Interaction of Grid Generated Turbulence with Expansion Waves

by

SAVVAS STELIOU XANTHOS

A Dissertation Submitted to the Graduate Faculty in Engineering in partial fulfillment of the requirements for the degree of Doctor of Philosophy, The City University of New York.

2004

INFORMATION TO USERS

The quality of this reproduction is dependent upon the quality of the copy submitted. Broken or indistinct print, colored or poor quality illustrations and photographs, print bleed-through, substandard margins, and improper alignment can adversely affect reproduction.

In the unlikely event that the author did not send a complete manuscript and there are missing pages, these will be noted. Also, if unauthorized copyright material had to be removed, a note will indicate the deletion.

ProQuest Information and Learning Company
300 North Zeeb Road
P.O. Box 1346
Ann Arbor, MI 48106-1346

This manuscript has been read and accepted for the Graduate Faculty in Engineering in satisfaction of the dissertation requirement for the degree of Doctor of Philosophy.

4/29/04
Date

Professor Yiannis Andreopoulos
Chair of Examining Committee

April 29, 2004
Date

Dean Mumtaz Kassir
Executive Officer

Professor Yiannis Andreopoulos
Mentor, Dept. of Mech. Eng., CCNY

Professor Latif M. Jiji
Dept. of Mech. Eng., CCNY

Professor Charles Watkins
Dept. of Mech. Eng., CCNY

Professor Damian Rouson
Dept. of Mech. Eng., CCNY

Professor Volkan Ötugen
Dept.of M, A & M Eng., Polytech U

Supervisory Committee

THE CITY UNIVERSITY OF NEW YORK

Abstract

Interaction of Grid Generated Turbulence with Expansion Waves

by

Savvas S. Xanthos

Advisor: Professor Yiannis Andreopoulos

The interaction of traveling expansion waves with grid-generated turbulence was investigated in a large-scale shock tube research facility. The incident shock and the induced flow behind it passed through a rectangular grid, which generated a nearly homogeneous and nearly isotropic turbulent flow. As the shock wave exited the open end of the shock tube, a system of expansion waves was generated which traveled upstream and interacted with the grid-generated turbulence.

The Mach number of the incoming flows investigated was about 0.3 hence interactions are considered as interactions with an almost incompressible flow. Mild interactions with expansion waves, which generated expansion ratios of the order of 1.8, were achieved in the present investigations. In that respect the compressibility effects started to become important during the interaction.

A custom designed vorticity probe was used to measure for the first time the rate-of-strain, the rate-of-rotation and the velocity-gradient tensors in several of the present flows. Custom made x-hotwire probes were initially used to measure the flow quantities simultaneously at different locations inside the flow field.

Although the strength of the generated expansion waves was mild, $S = \left[\frac{\partial U}{\partial x}\right]_{EW} = 50$ to100 s^{-1}, the effect on damping fluctuations of turbulence was clear. Vorticity fluctuations were reduced dramatically more than velocity or pressure fluctuations.

Attenuation of longitudinal velocity fluctuations has been observed in all experiments. It appears that the attenuation increases in interactions with higher Reynolds number. The data of velocity fluctuations in the lateral directions show no consistent behavior change or some minor attenuation through the interaction. The present results clearly show that in most of the cases, attenuation occurs at large $\frac{x}{M}$ distances where length scales of the incoming flow are high and turbulence intensities are low. Thus large in size eddies with low velocity fluctuations are affected the most by the interaction with the expansion waves. Spectral analysis indicated that spectral energy is shifted after the interaction to lower wave numbers suggesting that the typical length scales of turbulence are increased after the interaction.

Acknowledgments

To all the people who collaborated, assisted, listened in some way or another, understood in more ways than one and had the strength to allow me to conclude this great educational trip, I would like to thank and say that I am deeply in debt; therefore this page is dedicated to you.

First of all, and not because I have to, I would like to thank my mentor and friend Dr. Yiannis Andreopoulos for his constant guidance throughout the years as a student. His wealth of knowledge allowed me to grow and learn and not be afraid to tackle ambitious goals that he himself always tries to reach for. I would also like to thank my friend and colleague, now Dr. Zhexuan Wang for always being impatient, allowing me thus to grow and mature as in individual. Mr. Minwei Gong has been my co-mentor throughout the years and for sure if it was not for him this research attempt would have never been completed. I would also like to thank my old colleague, Mr. Alexis Pierides for the help, guidance and all the wonderful times we spent here at CCNY as well as Dr. Juan Agui, now at NASA Glenn Research Center in Ohio, for always being available to take and answer all kinds of questions that pertained to this research effort. Before giving my gratitude to the Mechanical Engineering Department as a whole, I would like to thank Robert Suhoke for always being there for everything; endless discussions and debates. To the three technicians who always said "sure", Mr. Jinrui Chen, Mike Askenazy and Robert Kalfa I would like to say thank you as well. For Mr. Luis Hernandez, the only thing that comes in mind is that he never says "no".

All the years spent studying and doing research would have not been possible with out the support of my dear family who lives abroad and for sure without the support

of my wonderful girlfriend Kelly Brook Emerton that has been most supportive, understanding and above all loving on all occasions. I thank you all and I wholeheartedly dedicate this to you.

Table of Contents

Nomenclature

a	sonic speed
C_p	constant pressure heat capacity
C_v	constant volume heat capacity
dU/dx	longitudinal derivative of mean longitudinal velocity
dU/dy	lateral derivative of mean longitudinal velocity
dU/dz	transverse derivative of mean longitudinal velocity
δ	local boundary layer thickness
Δp	pressure drop
d	grid rod diameter
EW	Expansion Wave
G	Amplification ratio
h	pitch coefficient
I	current
R_w	wire resistance
V	Voltage
K	pressure drop coefficient
K_1	wave number
k	pitch coefficient
L_e	dissipative length scale
Λ	pressure gradient parameter
λ	length scale

μ_t	eddy viscosity
M	Mesh Size
M_2	Shock Wave induced flow Mach number
M_s	Shock Wave Mach number
M_R	Reflected Shock Wave Mach number
$\bar{M}$	mean Mach number
p.d.f	probability density function
P	static pressure
P_0	total pressure
$P_0^{'}$	total pressure fluctuations
$P^{'}$	static pressure fluctuations
$\overline{P_0}$	mean total pressure
q	square root of TKE
r.m.s.	root mean square
R	specific gas constant
$\bar{R}$	universal gas constant
Re	Reynolds number
Re_M	Reynolds number based on mesh size
Re_λ	Reynolds number based on Taylor microscale
ρ	density
ρU	mass flux
SW	Shock Wave
σ	solidity

σ_i	upstream standard deviation
σ_i	downstream standard deviation
S^2	variance
T	static temperature
T_0	total temperature
τ_o	wall shear stress
S	mean shear
TVD	Total Variation Diminishing
$\overline{T_0}$	mean total temperature
t	time
Δt	sampling frequency interval
U_1	x-velocity
U_2	y-velocity
U′	velocity fluctuations
U_{eff}	Hot wire Effective velocity
U_N	Normal components of velocity
U_T	Tangential components of velocity
U_B	Binormal components of velocity
U_2	Shock Wave induced flow velocity
W_s	Shock Speed
Ωi	vorticity component in i direction
$\Omega i\ \Omega i$	enstrophy

List of Tables

List of Figures

Chapter 1: Introduction

1.1. Summary of Research

The interactions of shock waves and expansion waves with turbulent flows are of great practical importance in many engineering applications since they considerably alter the fluid field. Although a substantial amount of work has been devoted in the past to study the behavior of turbulent flows, turbulence remains an unsolved problem for the science and engineering community. For example, there is a need to be able to predict and control high subsonic to high supersonic speed flows for optimal design of aerospace vehicles. In this Mach number range, large variations in pressure, density or temperature can take place that can have an impact on the dynamics of turbulence. Improving prediction capabilities and providing effective control of compressible flows requires an accurate description of the large and small scales dynamics as well as the time-averaged statistical properties of the flow. Thus, a better fundamental understanding of the turbulent flow structure is essential.

Most of the work on viscous interaction of compressible turbulence with waves has been heavily concentrated on interaction with shock waves in an effort to alleviate its adverse effects on the flow. For example, the unsteady interaction of a moving shock wave with nearly homogeneous and isotropic decaying compressible turbulence reveals attenuation of the shock wave's strength as a result of the interaction with the turbulent flow field, which depends on the mesh size of the grid or its Reynolds number, the flow Mach number and the initial Mach number of the shock wave. Finer grids produce turbulence, which attenuates the shock wave more than coarse grids at the same Mach

number. Amplification of pressure fluctuations after the interaction is observed which also depends on grid size (initial turbulence level) and grid shock strength.

The objective of the present work is to increase the physical understanding of compressible turbulence interacting with expansion waves focusing on issues such as attenuation of turbulence intensity and pressure fluctuations based on grid size, reduction in skin friction and issues of relaminarization. The basic understanding of the physics of such a flow was obtained through investigations in conveniently selected and reasonably simplified flow configurations. A decaying compressible grid-generated homogeneous and isotropic turbulent flow interacted with a planar expansion wave in a shock tube to explore the potentially favorable effects of expansion waves on turbulence. A schematic of this interaction is shown in Figures 1.1 and 1.2.

It should be expected, similar to the case of shock wave–turbulence interaction, see Andreopoulos et al.[1], that expansion wave-turbulence interaction will depend on:

a) the characteristics of the interacting expansion wave like strength, relative orientation to the incoming flow, and location and shape,

b) the state of turbulence of the incoming flow as it is characterized by the fluctuation levels of velocity, density, pressure and entropy and length scales ,

c) the level of compressibility of the incoming flow, and

d) the flow geometry and boundary conditions.

All the above issues and more were addressed with the aid of the Large Shock Tube Research Facility (STURF) located in the Mechanical Engineering Department that provides a platform for high spatial and temporal resolution measurements of turbulence. The later combined with the small size of transducers and probes of high frequency

response as well as with single hotwires, X hotwire probes and a Vorticity probe allowed for the investigation of all the issues mentioned above.

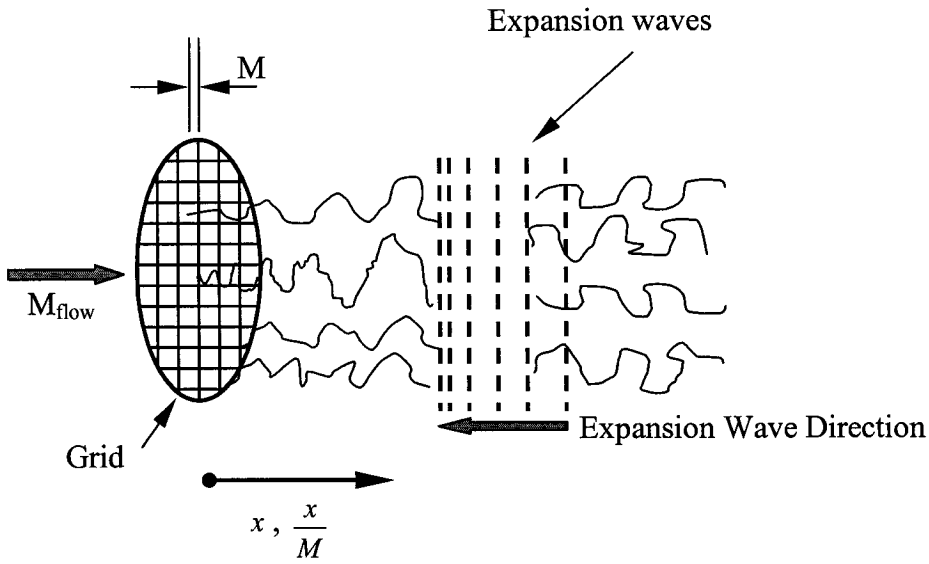

Figure 1.1: Schematic of Interaction of expansion waves with isotropic turbulence.

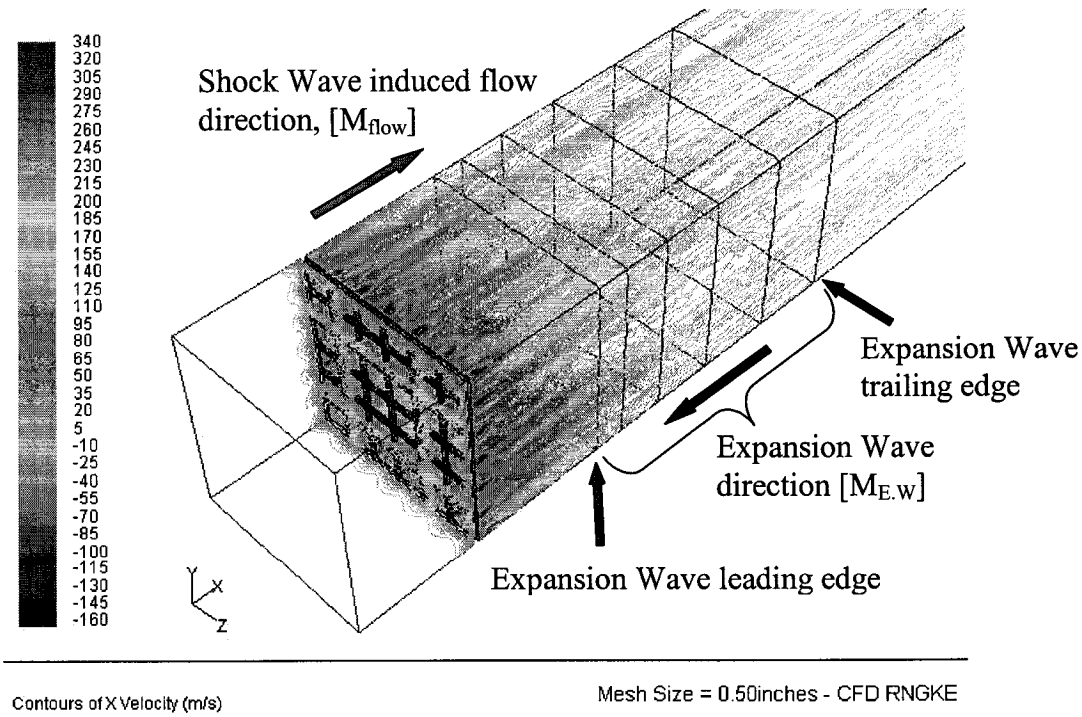

Figure 1.2: CFD modeling of the Interaction of expansion waves with isotropic turbulence. Contours of X – Velocity [m/s].

Chapter 2: Background Information

2.1. Introduction

Shock waves and expansion waves occur frequently in many technological applications. The supersonic flow over a blunt body is a basic example of a strong bow shock wave creation and the supersonic flow over a convex corner is a typical example of an expansion fan creation. The generation of shock waves or expansion waves can be observed in many engineering applications, i.e. inside turbines or compressors of turbine engines as a result of the supersonic flow and unsteady flow phenomena. These moving waves can interact with rotating or stationary blades as well as with the flow and may result in phenomena, which can affect the operation and performance of the engine. Another example of shock wave and expansion wave interaction with turbulence is in hypersonic viscous flows attached on the surface of hypervelocity vehicles in the form of boundary layers or separated from it, in the form of vortex emanating from a control surface. These flows can be significantly affected, for example, after passing through a shock wave or an expansion zone greatly affecting the performance of the vehicle.

In particular, one of the phenomena is the interaction of passing shock waves and expansion waves with free stream turbulence, which can be considered as nearly isotropic and nearly homogeneous. A unique facility has been developed at CCNY in which the Mach number of the flow behind the reflected shock can be controlled independently from the shock wave strength up to a certain extent. This has been achieved by replacing the end wall of the shock tube with a porous wall of variable porosity. Having a solid end wall with a porosity value of zero [0] results in a total reflection of the incident shock wave into another shock wave whereas having an open end wall, a porosity value of one

[1], results in a reflection of the incident shock wave into an expansion wave. The later configuration has been used for in the present work. The large size of this facility allows measurements of turbulence with high spatial and temporal resolution (see Briassulis & Andreopoulos[2], Briassulis et al.[3], Agui[4]). Thus, shock and expansion wave interactions even with incompressible flows can be generated.

The objective of the present research should be clear; to explore the effects of expansion waves on turbulence yet one could not clearly demonstrate the reasoning behind this objective unless some background information, in a sort of a nutshell, on the interaction of shock waves with grid turbulence was provided.

Past work on shock wave – turbulence interaction, which has been recently reviewed by Andreopoulos et al.[1] has shown that the interaction between a shock wave and turbulent flow is mutual and the coupling between them is very strong. Complex linear and non-linear mechanisms are involved which can cause considerable changes in the structure of turbulence and its statistical properties and alter the dynamics of the shock wave motion. Amplification of velocity fluctuations and substantial changes in length scales are the most important outcomes of interactions of shock waves with turbulence. This indicates that such interactions may greatly affect mixing. Contrary to the shock wave interaction with turbulence, outcomes of which are previously mentioned, the expansion wave interaction with turbulence has to have attenuating effects on turbulence, reduction in skin friction and possible relaminarization of the flow. This work has focused on an idealized case of an interaction of a planar expansion wave traveling through a grid-generated turbulence. This flow represents an interaction with a simplified yet relevant geometry, which can be used to investigate basic physics and/or as a test case for

turbulence modeling in computational fluid dynamics. One way to simulate experimentally the aforementioned interaction is by taking advantage of the induced flow behind a moving shock in a shock tube. This flow is passed through a turbulence-generating grid and the decaying turbulence behind the incident shock interacts with the expansion wave after it has been reflected from the end wall of the shock tube. Figure 1.1 shows a schematic of the flow interaction in the shock tube. This flow configuration in the shock tube provides a platform to investigate some fundamental issues associated with turbulence through its interaction with the moving expansion wave. A full description of the incoming compressible decaying turbulence before the interaction can be found in Briassulis et al.[3].

In general, interactions of shock waves and expansion waves with turbulent flows are of great practical importance in external or internal aerodynamics of engineering applications since they considerably modify the fluid field by vorticity and entropy production and transport.

2.2. Interactions of Expansion Waves with Grid Turbulence

Detailed experimental investigations of interactions of expansion waves with homogeneous and isotropic turbulence simply do not exist. The only existing studies are rather limited and have been confined to turbulent boundary layers, as it will be discussed shortly.

Past work by many investigators[5-9] has reported direct or indirect evidence demonstrating that in supersonic flow past an expansion corner the boundary layer reverts from turbulent state upstream of the corner to a laminar state downstream. This basically

indicates that expansion regions reduce the level of turbulence activity within a compressible boundary layer. This is not unexpected since the boundary layer after the expansion corner encounters a favorable pressure gradient and a strong dilatation effect.

In fact, Narasimha and Viswanath[10] attempted to identify a criterion for the occurrence of such reversion, following the theoretical work of Narasimha and Sreenivasan[11] performed at low speeds, which utilizes the ratio of the pressure gradient to a characteristic Reynolds stress gradient as the parameter governing the completion of reversion. This method has been successful in correlating and predicting the flow development, especially in the later stages of reversion. In fact, it has been suggested by the former authors in their study, that when a so-called pressure gradient parameter defined by:

$$\Lambda = -p' \frac{\delta}{\tau_o} \qquad (2.1)$$

is very large, reversion or relaminarization can occur. In this case according to the author's definition, reversion takes place if there is evidence either of the growth of a thin new shear layer from the corner or a considerable change in the associated flow characteristics downstream. In supersonic flows, the pressure gradient typically occurs over a few boundary layer thicknesses at the most, hence equation (2.1) simplifies to the form:

$$\Lambda = -\frac{\Delta p}{\tau_o} \qquad (2.2)$$

Empirical values of Λ above 70 are considered large enough for both incompressible and compressible flows, values that indicate the region of reversion or non-reversion. Here p' is the pressure gradient through the acceleration, δ is the local boundary thickness and τ_o is the wall shear stress in the boundary layers just upstream of the acceleration. Δp is the

pressure drop after the interaction of the expansion fan with the boundary layer (considered positive in an expansion; favorable pressure gradient) over a few δ.

Even though the previously mentioned work shows some encouraging signs of relaminarization, some of the lines of work discussed in the later paragraphs will indicate that the issue of relaminarization is not one of superficial nature and surely not an issue that is yet resolved.

Dussauge and Gaviglio[12] studied the rapid expansion of a turbulent boundary layer in supersonic flow both analytically, based on the Rapid Distortion Theory (see reference 45) and experimentally emphasizing on the effect of bulk dilatation on turbulent fluctuations. The authors indicated that their Mach 1.76 turbulent boundary layer had been relaminarized by the expansion. Following the same hypotheses as the previously mentioned authors, Smith and Smits[13] used Rapid Distortion Approximation (RDA) to simplify the Reynolds Stress equations, retaining terms, which were then modeled as functions of the Reynolds stress tensor and gradients of the mean flow. The modeled equations were then evaluated by comparison of calculated results with experimental results for the case of a Mach 2.84 turbulent boundary layer in a 20-deg centered expansion. Very good agreement between the two sets was reported. The authors do not mention any evidence of reversion and based on their results mention that caution should be taken before using the term of "relaminarization".

Moreover, Dawson et al.[14] performed multipoint wall pressure measurements to investigate the response of a Mach 3, fully developed, compressible boundary layer to a centered and a gradual ($\frac{R}{\delta} \cong 50$) expansion, both of 7-deg and 14-deg deflection. They also did not mention any evidence of relaminarization, since, although their r.m.s

fluctuation levels decreased across the expansions, the r.m.s normalized by the local static pressure remained nominally constant.

Johnson[15] on the other hand recently presented turbulence measurement downstream of a convex wall with expansion corner where the flow was relaminarized. In this experiment the flow had yet to recover after its first distortion through a concave wall, while compression corner preceded the flow of Smith and Smits. Successive distortions in the flow have a rather non-linear effect and therefore all the effects of expansion are considerably masked either by the non-equilibrium state of the flow upstream of the expansion corner or by the simultaneous presence of flow distortions due to streamline curvature. The total turning angle α of the flow imposes a normal pressure gradient to the wall flow, which may have a stabilizing effect if the streamline curvature is convex or may cause a destabilizing effect if the curvature is concave.

In the hypersonic regime, the works by Bloy and Georgeer[16], Hill[17] and Lewis, Gran and Kubota[18] found no evidence of relaminarization of the boundary layers.

Recent work by Arnette, Samimy & Elliot[19] and Dawson, Samimy and Arnette[20] provided more detailed information on the structure of turbulent boundary layers through expansion corners yet the authors did not mention any signs of relaminarization.

It was obvious from the reviewed literature that more fundamental work was needed which can lead to better understanding of the phenomena related to interactions of compressible turbulence with expansion waves.

Some of the fundamental aspects of turbulence can be studied better in flow configurations where the flow is nearly homogeneous and turbulence is nearly isotropic. The presence of a solid wall as a boundary in turbulent flows complicates its

understanding by introducing large mean velocity gradients at the wall which are responsible for the continuous production of turbulence. In order to better understand the effects of expansion waves on turbulence, the interaction of grid-generated turbulence with planar expansion waves was proposed. The effects of sudden expansion of zero mean-shear turbulent flow have not been investigated before. The flow behind a turbulence-generating grid contains a large scale of turbulent scales the size of which depends on the distance from the grid and on its mesh size. This can establish an experimental set up where the interaction of expansion waves with a flow having a variety of turbulence scales can be studied. In flows where turbulence is distorted by a rapidly applied mean shear $S = (\frac{\partial U}{\partial x})_{EW}$, the controlling parameter is the ratio of the time-scale of turbulence $\frac{L_e}{q}$ to the time scale of the applied strain, $\frac{1}{S}$ i.e. $r = \frac{L_e S}{q}$. L_e is the dissipative length scale and q is the square root of the turbulence kinetic energy (TKE). It appears that r is proportional to the pressure drop ratio and q^2 and inversely proportional to the dissipation rate of turbulence kinetic energy ϵ, i.e. $r \approx \frac{\Delta p}{p}\frac{q^2}{\varepsilon}$. Thus, this particular flow can provide different values of this scaling parameter at different distances from the grid. The data to be obtained have the potential to provide significant contributions in the modeling compressible turbulence, which, so far, is entirely based on subsonic flow concepts.

Preliminary results of the interaction of turbulence with expansion waves are found in the work by Xanthos and Andreopoulos[21] where a 20 percent overall reduction in the r.m.s value of the pressure fluctuations after i.e. downstream of the interaction with

the expansion waves is reported, indicative of the reduction in the range of the fluctuations after the interaction. Based on the results briefly described above, along with the mixed and controversial, one might describe, set of results presented in the literature review, the objective of the present research work is clearly to investigate and explore the potentially favorable effects of expansion waves on turbulence. In the very few previous investigations of interactions of turbulence with expansion waves, the effects due to stabilizing streamline curvature substantially masked the effects of turbulence suppression due to flow expansion through the waves. In the proposed flow configurations, planar expansion waves interacted with grid-generated turbulence in the high-resolution shock tube research facility of CCNY, as mentioned in the introduction part. This approach has assessed directly the effects of the interaction on turbulence.

2.3. The Shock Tube Facility

Unlike conventional low speed grid turbulence generated in a wind tunnel, the present flow is produced in a shock tube behind a moving shock wave. Shock tubes are traditionally used to study mainly moving shock waves and their reflections, or interactions with solid surfaces and to generate high temperature environments. Our work is not the first one to configure a stationary flow behind a moving shock wave. There have been several attempts in the past to utilize the induced flow behind the shock to study several flow phenomena. The experiments will be performed in the large scale Shock Tube Research Facility (STURF), shown in Figures 2.1 and 2.2. The large dimensions of this facility, 1 ft in diameter and 88 ft in length, provide an excellent platform for high spatial resolution measurements of turbulence with long observation

time of steady flow. The induced flow behind the traveling shock wave passes through a turbulence-generating grid installed in the beginning of the working section of the facility.

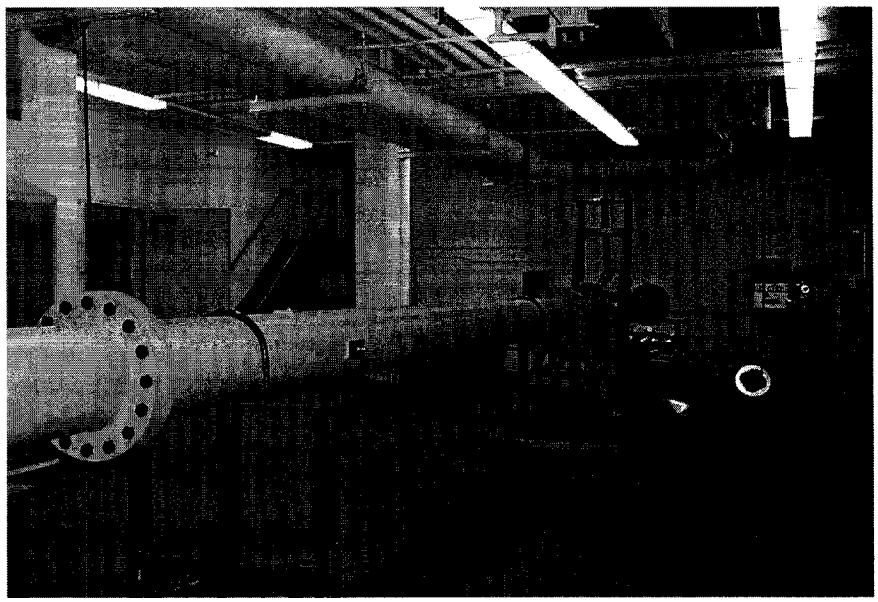

Figure 2.1: Shock Tube facility at CCNY, Driver section.

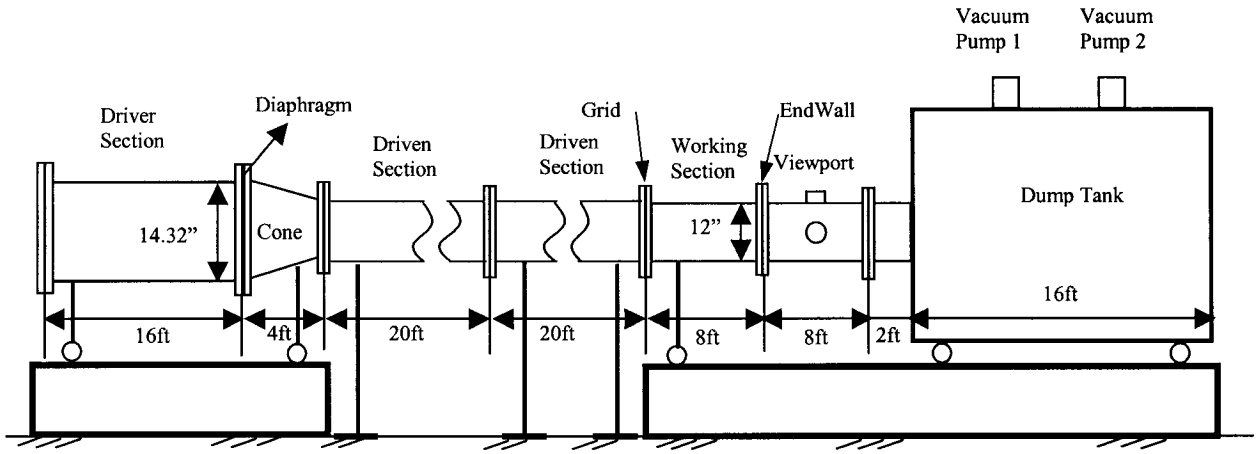

Figure 2.2: Schematic of Shock Tube Research Facility.

Several turbulence-generating grids were used at different flow-Mach numbers. The velocity of the induced flow behind the shock wave depends on the rupture pressure of the diaphragm, i.e. driver strength P_4.

The present shock tube facility has three distinguishing features. The most significant one is the ability to control the strength of the reflected shock and the flow quality behind it by using a removable porous end wall, placed at the flange between the dump tank and the working section. The impact of shock wave on the end wall would result in a full normal shock reflection in case of zero porosity (solid wall), a weak shock reflection in case of moderate porosity, or expansion waves in case of porosity value of unity (open end wall). The second feature of the facility is the ability to vary the total length of the driven section by adding or removing one of the several pieces or modules that are available or rearrange their layout. Proper arrangement of the layout of the various modules of the shock tube can maximize the duration of the useful flow. The third feature of the facility is its large diameter, which allows for a large area of uniform flow in the absence of wall effects to be available while at the same time can provide a platform for high spatial resolution in the measurements of turbulence.

There are two available working (test) sections, 2 feet and 8 feet in total length respectively. Both are fitted with several single and X-type hotwires, a vorticity probe and pressure ports (see Figures 2.3-2.7). This experimental set-up allows for time-dependent measurements of one, two and three-velocity components, three components of vorticity, total temperature, wall pressure and span wise pressure at several locations of the flow field simultaneously. The pressure signals and velocity information can be acquired with high frequency response Kulite pressure transducers type XCQ-062 both

inserted in the flow (Mach Probes) and by pressure transducers flash mounted on the wall along the working section.

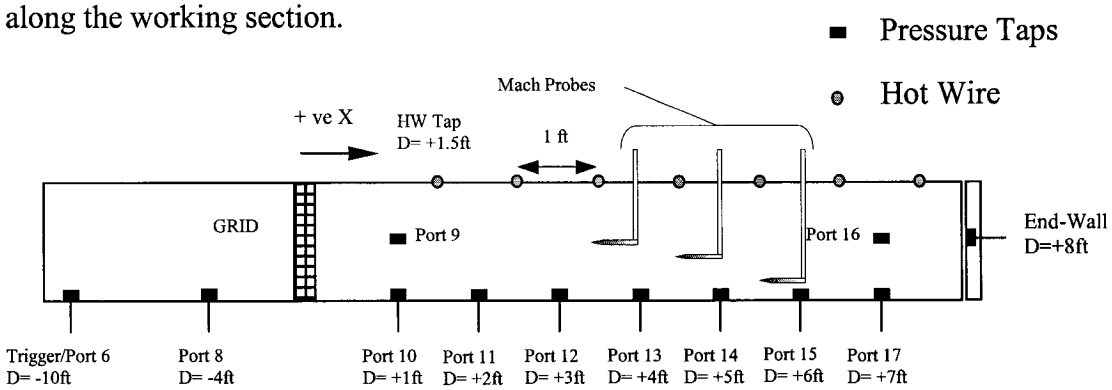

Figure 2.3: 2D schematic of the working section with pressure and hot wiretap's locations along the 8 ft length.

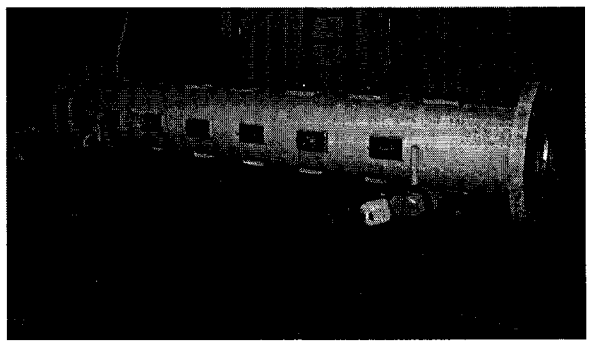

Figure 2.4: Actual 8ft section with all tabs shown.

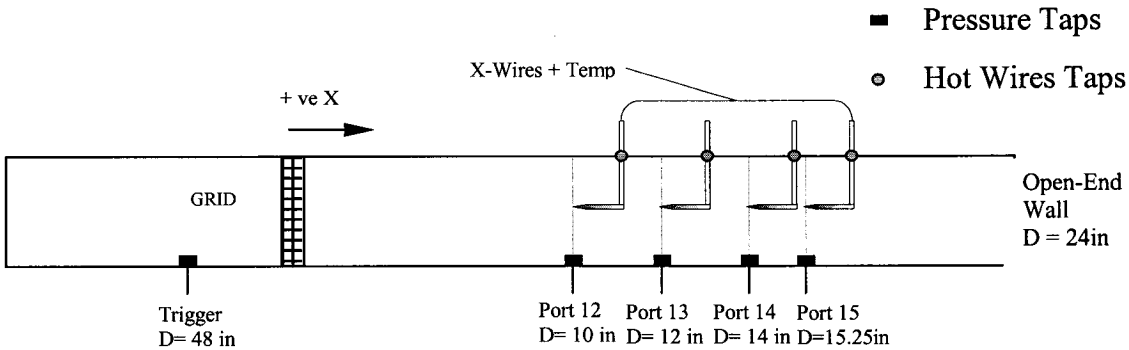

Figure 2.5: 2 D schematic of the working section with pressure and hot wiretap's locations along the 2 ft length. X-WIRE CASE.

For details on the hot-wire techniques applicable to shock tubes see Briassulis et al.[22, 23,24] where estimates of uncertainties in the measurements are also given.

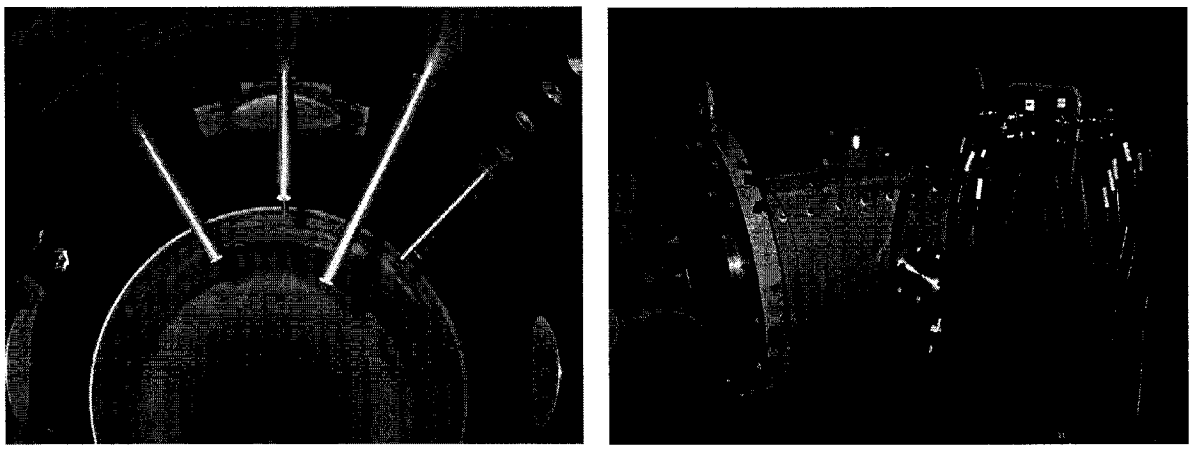

Figure 2.6: 2ft working section – inside view with hotwires shown – outside view with connectors.

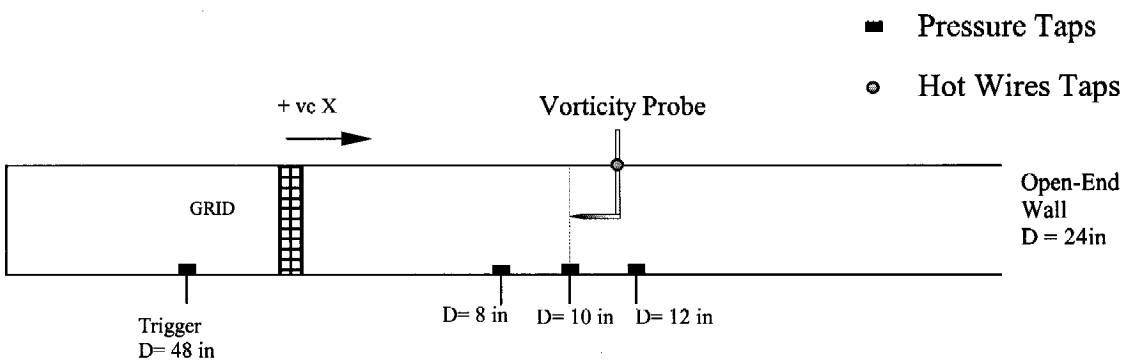

Figure 2.7: 2 D schematic of the working section with pressure and vorticity probe locations along the 2 ft length. VORTICITY PROBE CASE.

In addition the working section provides some view ports where non intrusive laser imaging techniques can be utilized to visualize the flow i.e. interaction of the turbulent field with expansion waves and/or shock waves.

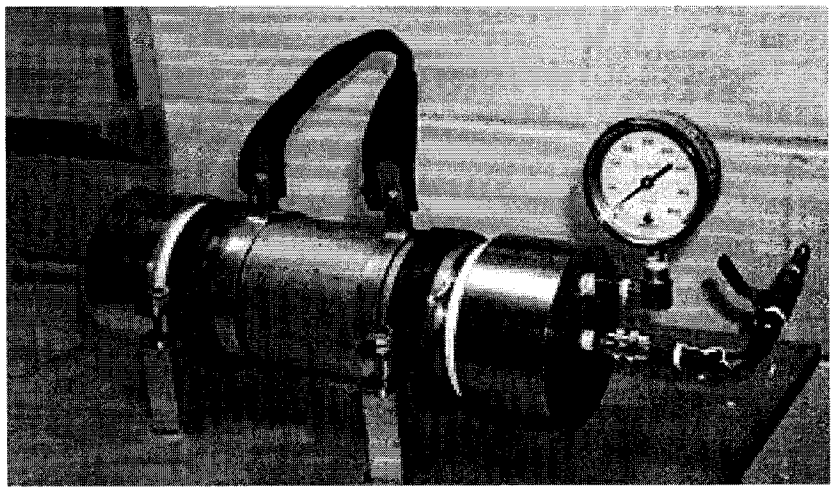

Figure 2.8: Pressure Transducer calibrator

Prior to any experiment, the shock tube is fitted with 9 pressure taps in the working section and 8 in the driven section. The later transducers are placed throughout the driven section in order to monitor the passage of the shock wave and also to check its uniformity through the driven section. The shock tube is then pressurized so any leaks can be detected prior to the experiments, and once the shock tube is free of any leaks a static calibration is performed. The static response of the transducers is typically linear and previous tests on these types of transducers revealed that the difference between the static and dynamic calibration is only a few percent. The temperature effects are even smaller for this type of transducers. A detailed description of the facility and the results of the qualification tests can be found in the work by Briassulis[23] and Briassulis et al.[24]. Moreover the same transducers are calibrated statically in a pressure chamber that was designing specifically for this reason. Figure 2.8 shows the actual assembly of the pressure calibrator. Aluminum plates shown in Figure 2.9 are used as diaphragms and are placed in between the driver and the conical sections. Initially, a circular 0.125in

aluminum diaphragm (M1100) is inserted in between connecting flanges, which separate the driver (dark section seen in Figure 3.1, red in true color) from the rest of the facility, thus creating a partition.

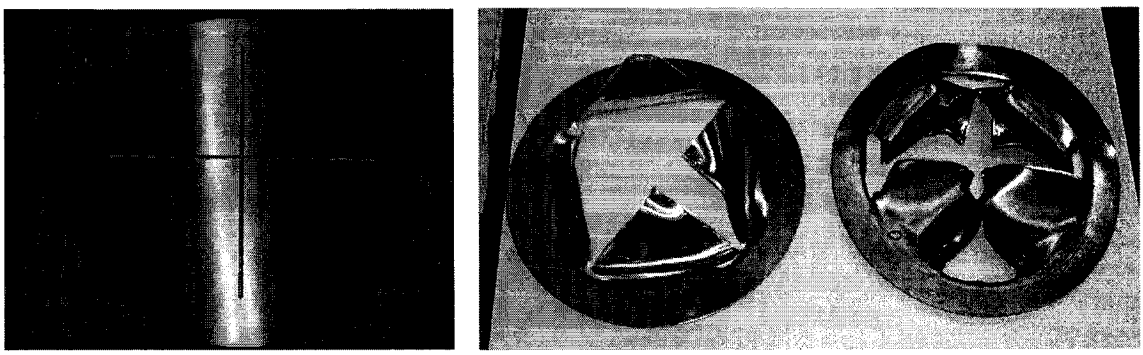

Figure 2.9: Typical diaphragms, before burst/after burst

The 18½ inch diameter diaphragms are machined with a 10 degree conical tapered end mill that inscribes a mark shown in Figures 2.10 and 2.11 to create a weak point where which will aid in rupturing the diaphragm and in controlling the bursting pressure. The following Figure shows a typical scoring mark of 0.060 inches in depth that would result in a bursting pressure of about 70psi.

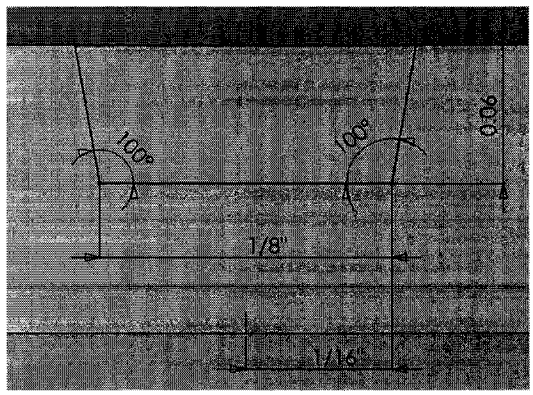

Figure 2.10: 2D schematic of the diaphragm scoring depth.

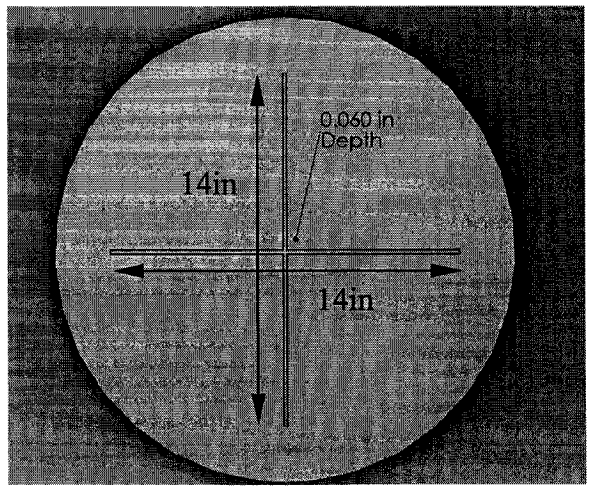

Figure 2.11: 2D Top View the diaphragm with score
Cut from Center extends 7 inches in each direction, 14in overall centered.

The basic operation consists of pressurizing the driver section until the dividing diaphragm ruptures. Immediately after the diaphragm ruptures there is a simultaneous generation of a shockwave, which travels downstream (into the driven section) at supersonic speed and expansion waves which travels at the local sonic speed in the opposite direction, upstream. The interface, which separates the gas initially in the driver section from the gas in the driven section is known as the contact surface. This interface is associated with sharp changes in density and temperature between the two gases. The shock which is marked by a sharp jump in pressure induces uniform flow behind it while the expansion fan produces a gradual drop in pressure. Structurally the facility can withstand a maximum pressure differential between driver and drives sections of roughly 1000 to 1 which has the potential of producing shock Mach numbers of 3.2 and an induced flow which reaches an asymptotic value of 1.89.

During experiments all signals are acquired simultaneously by using 4 National Instruments PCI 6120 boards with 800 KSamples/sec sampling rate per each of the 16

channels available at 16 bits resolution. The data acquisition system is triggered by the arrival of the shock wave at the location of a wall pressure transducer 4 feet or 10 feet upstream of the grid. The bulk flow parameters of the experiments that were performed are listed individually according to the chapter that they are referred to, and include the grid mesh density, the mesh size M, the flow Mach number M_2 behind the incident shock of strength M_s, the Reynolds number based on mesh size Re_M and mean flow velocity U_2 and the solidity of the grids σ, defined as the projected solid area per unit total area so that $\sigma = 1 - \left[1 - \frac{d}{M}\right]^2$, where d is the rod diameter and M is the mesh size. All grids are fabricated from circular steel rods and are shown in Figure 2.12 and Figure 2.13.

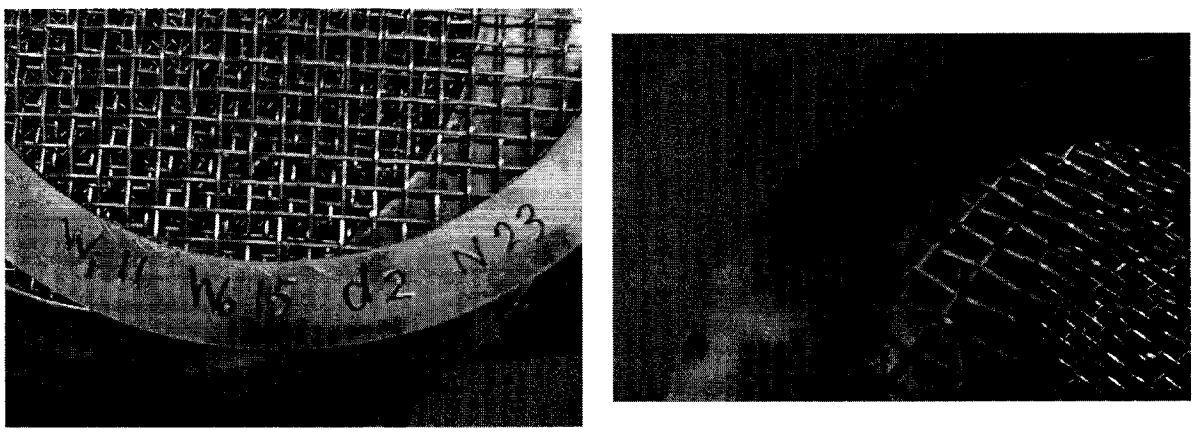

Figure 2.12: Typical grids.

Grid Meshes/in	Wi (in)	Wo (in)	Wav (in)	d (in)	N	Solidity σ
1 x 1	0.89	1.12	1.005	0.115	12	0.22
1.33x1.33	0.65	0.87	0.76	0.11	16	0.28
2 x 2 [a]	0.39	0.61	0.5	0.11	24	0.39
2 x 2 [b]	0.43	0.59	0.51	0.08	23	0.28
3 x 3	0.25	0.41	0.33	0.08	35	0.39
4 x 4	0.18	0.31	0.245	0.065	47	0.44
5 x 5	0.16	0.24	0.2	0.04	61	0.37
8 x 8	0.1	0.15	0.125	0.025	99	0.36

Table 2.1: Grid Dimensions.

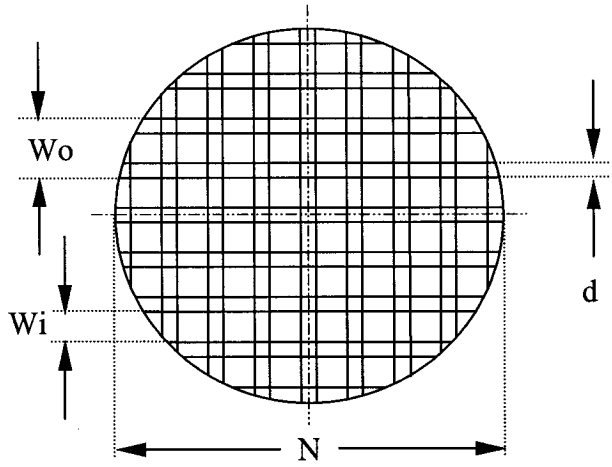

Figure 2.13: Schematic of the grid with reference to Table 2.1.

All the Grid dimensions are given in Table 2.1. The values of M_2 are obtained in the flow downstream of the grid and they are slightly smaller than the Mach number values obtained in the approaching flow upstream of the grid. As the incoming shock wave reaches the grid, it is transmitted through the grid with some minor losses due to viscous effects while a very weak reflected shock travels as a small disturbance in the opposite direction upstream as a result of the impact of the incident shock on the grid. This disturbance is stronger at higher shock Mach numbers and in impacts with higher solidity grids. This weakly reflected shock reduces the velocity and increases the temperature of

the approaching flow by small amounts respectively. The induced flow behind the incident shock, after it has experienced the effects of the upstream traveling weakly reflected shock, passes through the grid to form a nearly homogeneous and isotropic flow.

2.4. The Shock Tube Flow

Unlike conventional low speed grid turbulence, generated in a wind tunnel, the present flow is produced in a shock tube behind a moving shock wave. Shock tubes are traditionally used to mainly study moving shock waves and their reflections or interactions with solid surfaces and to generate high temperature environments. This work is not the first one to configure a stationary flow behind a moving shock wave. There have been several attempts in the past to utilize the induced flow behind the shock to study several flow phenomena. The results that are presented in this section are based on the interaction of a shock wave reflected off the porous end wall given that no experimental data yet exist for the interaction of grid generated turbulence with expansion waves. They are given merely to illustrate the flow characteristics in the shock tube.

The duration of the induced flow behind the shock wave may be limited by the arrival of reflected expansion waves from the driver end wall which are formed during the rupture of the diaphragm, by the arrival of shock or expansion waves formed at the downstream end wall and the arrival of the contact surface which is characterized by a large temperature gradient. To determine how different parameters (i.e. pressure, density, temperature etc.) vary with time and position in the shock tube, a predictive tool was

developed based on the predictor-corrector Total Variation Diminishing scheme (TVD). The reader is referred to chapter 4 that gives a detailed description on the simulations. The formation of a nearly homogeneous and isotropic turbulent flow with decaying intensity can be described by considering the time-dependent wall pressure signals shown in Figure 2.14.

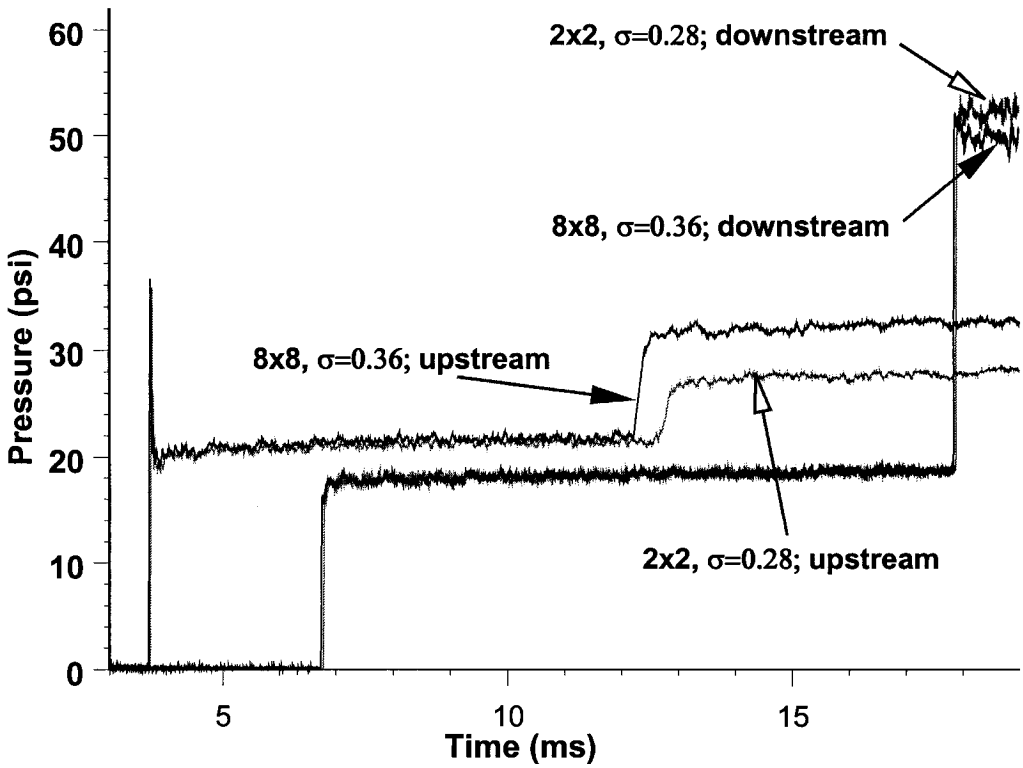

Figure 2.14: Time dependent pressure signals at locations upstream and downstream of grid. $\frac{P_4}{P_1} = 6.53$

The signals shown in this Figure were obtained at locations; one upstream and one downstream of the grid. Two different grids were used in this case, one with solidity

$\sigma = 0.28$ and M=12.7 mm (2x2 meshes/in) and the other with $\sigma = 0.36$ and M = 3.17 mm (8x8 meshes/in). The values of pressure plotted in this Figure are above the ambient atmospheric pressure. The incident shock is first detected by the pressure transducer located upstream of the grid. As the incoming shock reaches the grid, it is partly transmitted through the grid with some minor pressure losses associated with viscous effects, it is partly reflected and it travels in the opposite direction. This disturbance due to the reflected shock is stronger at higher Mach numbers and in impacts with higher solidity grids. The pressure signals shown in Figure 2.14 upstream of the grid correspond to flows with incident shocks of the same strength as is indicated by the same average pressure level behind, yet they clearly demonstrate the effect of grid in the reflected shock off the grid. The strength and speed of the reflected shock off the higher solidity grid (8x8) is higher than in the case of the lower solidity grid (2x2).

The reflected shock, which travels in the upstream direction reduces the velocity and increases the temperature of the approaching flow behind the incident shock by small amounts respectively. The induced flow behind the incident shock, after it has experienced the effects of the upstream traveling weakly reflected shock, passes through the grid to form a nearly homogeneous and nearly isotropic flow. A full documentation of the velocity field of the decaying turbulence can be found in the work by Briassulis et al.[3] The minor losses of the transmitted shocks can also be seen in Figure 2.14 by considering the pressure signals at the downstream of the grid location. In general, there some small differences in the level of pressure behind the incident/transmitted shocks, which can be attributed to the different grids. However, in the present case of the 2x2 and 8x8 grids, the incident shock after its passage through the grids has the same strength, to a very

good approximation, in both flows. The incident shock travels downstream and is reflected off the porous end-wall or solid end wall and returns to the measuring location after its interaction with the decaying turbulence present in the induced flow behind the incident shock. The pressure signals shown in Figure 2.14 show the arrival of the reflected shock at the measuring location to take place at about the same time in both flows. This indicates that both reflected shock fronts travel with the same propagation velocity. The pressure behind them, however, is different, which suggests that the shock strengths are not the same although their speeds do not differ.

There are some other issues related to the data processing, which need to be discussed in the context of the data statistics presented here. These are demonstrated in Figure 2.15, which shows a typical time resolved pressure signal obtained at a location downstream of the grid in an experiment with driver's pressure ration $\frac{P_4}{P_1} = 4.40$. In Figure 2.15 the end wall of the shock tube was left closed, resulting in a complete reflection of the shock wave. In the case of the open end reflection a typical signal is shown in Figure 2.16. P_1 is the pressure in the driven section before the rupture of the diaphragm, which in this particular case was the ambient atmospheric pressure. The signal in Figure 2.15 shows the arrival of the incident shock over the measuring location followed by the arrival of the reflected shock off the end-wall traveling upstream with Mach number M_R. As this reflected shock reaches the turbulence generating grid is partially transmitted through and partially is reflected in the opposite direction. This reflected grid shock is detected in the measuring location as it travels downstream towards the end-wall, where it is reflected and starts traveling in the opposite direction towards the grid. The pressure signal clearly shows its passage over the location of the pressure transducer.

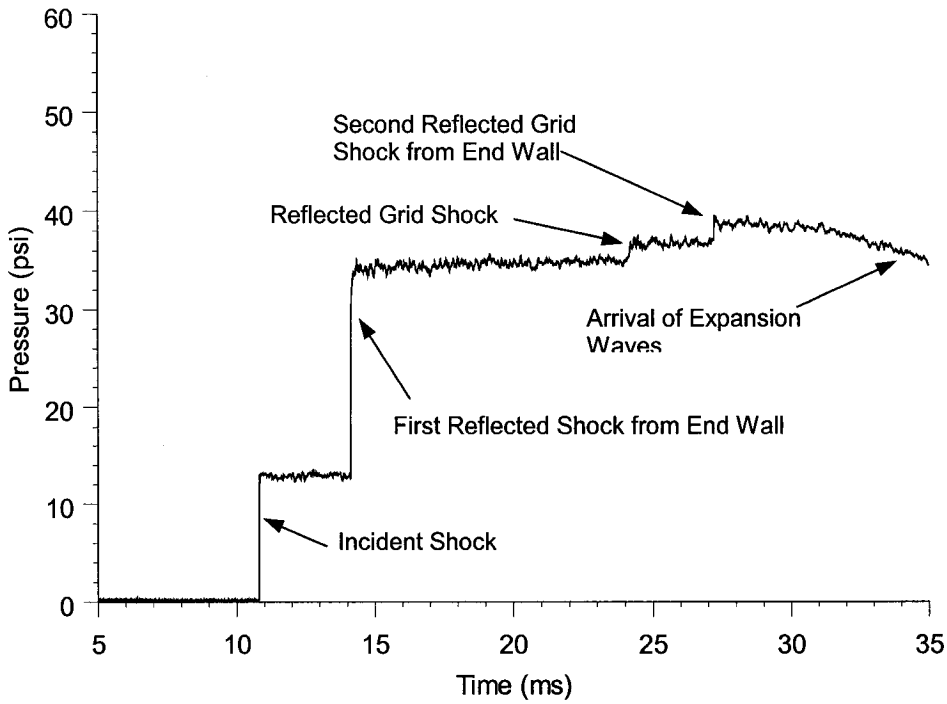

Figure 2.15: Typical pressure signal downstream of grid.5x5 grid size, $\frac{P_4}{P_1} = 4.40$

The pressure signal in Figure 2.15 also shows the arrival of the expansion waves, which are formed during the rupture of the diaphragm and travel initially in the opposite to the shock wave direction, towards the end wall of the driver's section. There they are reflected and travel downstream, which is an issue that shall be discussed more due to the complications it adds to the experiments during the interaction of the expansion wave reflected over the open end of the shock tube. Figure 2.16 is clearly marked with the different regions during a typical experiment with an open-end wall. An extensive program has been undertaken to assess the quality of the grid flow established in the shock tube. This was accomplished by measuring the flow uniformity and homogeneity in the working section on planes normal to the flow and in the longitudinal direction.

The flow isotropy was also tested and verified by several different methods. Results and details of the flow quality are shown and discussed by Briassulis et al.[3]. They have indicated that flow homogeneity is better in fine grids than in coarse ones.

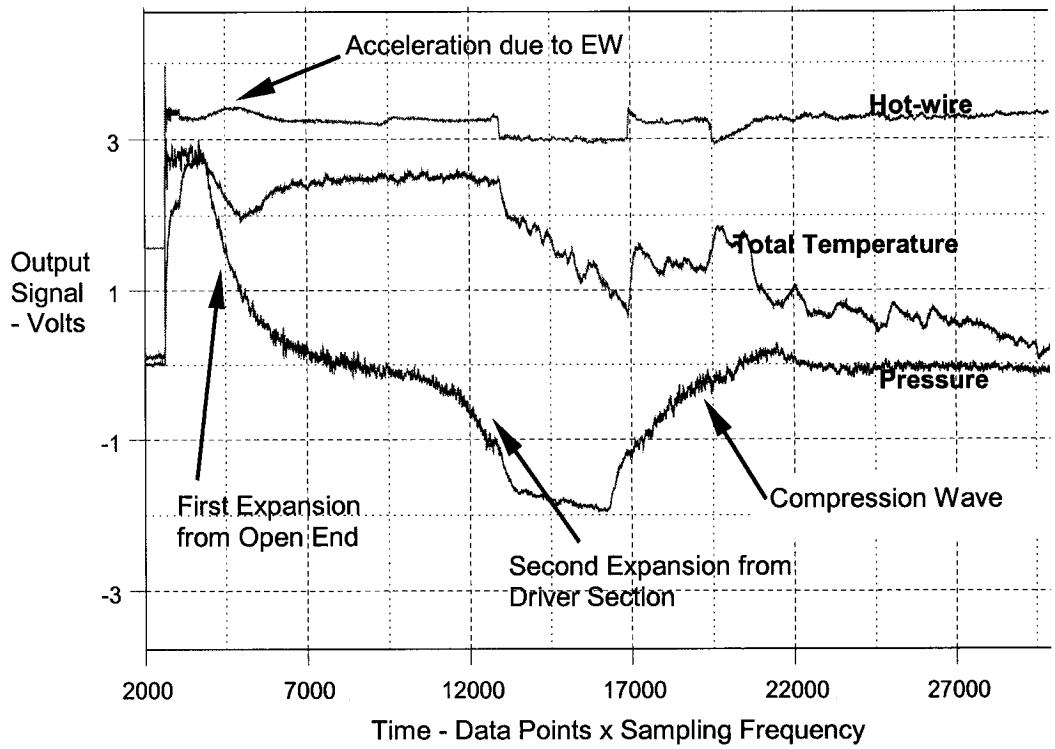

Figure 2:16: Typical pressure, mass/flux, Total temperature signal downstream of grid.8x8 grid size, $\frac{P_4}{P_1} = 4.40$

Chapter 3: Computational Analysis

3.1. CFD Method Introduction

As mentioned in the introduction, the way to experimentally simulate the interaction is by taking advantage of the induced flow behind a moving shock in a shock tube. This flow is passed through a turbulence-generating grid and the decaying turbulence behind the incident shock interacts with the expansion wave after it has been reflected from the end wall of the shock tube. In the present work, an attempt has been made to explore several bulk characteristics with the aid of CFD analysis. The results gave an insight and a direction to the correct choice of equipment, and in general, to the whole experimental setup and apparatus. These were compared against experimentally obtained results.

Three different CFD packages were utilized:

1. P_{41}: a one dimensional compressible inviscid flow calculation which provides information downstream of the moving shock wave such as:
    a. Shock speed and Flow velocity [$W_s, U_2 - \frac{m}{s}$]
    b. Total and Static Temperatures [T_{02}, $T_2 - K$]
    c. Density [$\rho_2 - \frac{kg}{m^3}$]
    d. Static and Total pressures [P_{02}, P_2 (Pa or psi)],

based on a predefined driver pressure P_4.

2. TVD (Total Variation Diminishing): one dimensional inviscid compressible flow analysis of expansion waves tailored to the present shock tube facility[1].
3. Gambit and FLUENT:

[1] This will be presented in detail in Chapter 4

a. 3-D unsteady inviscid flow package to simulate the moving shock wave and compute the flow through the grids utilized in the present experiments.

b. 3-D steady state viscous flow package (RNG Model) to compute the flow upstream, through and downstream of the grids.

c. 3-D unsteady viscous flow package with Large Eddy Simulation [LES] model to compute the flow upstream, through and downstream of the grids.

3.2. CFD and Experimental Results of Shock Waves Traveling Through Grids

When a moving shock wave impacts a grid in a face-on fashion, it generates a reflected shock traveling in the opposite direction and a transmitted shock propagating in the same direction as the original shock. The reflected shock which travels upstream has strength much higher than the incident shock in terms of pressure behind it, while the transmitted one has strength slightly lower than the original one. This is evident in Figure 2.14 and Figure 2.15 where the shock tube flow is described.

Four computational meshes of a single turbulence-generating grid were modeled under

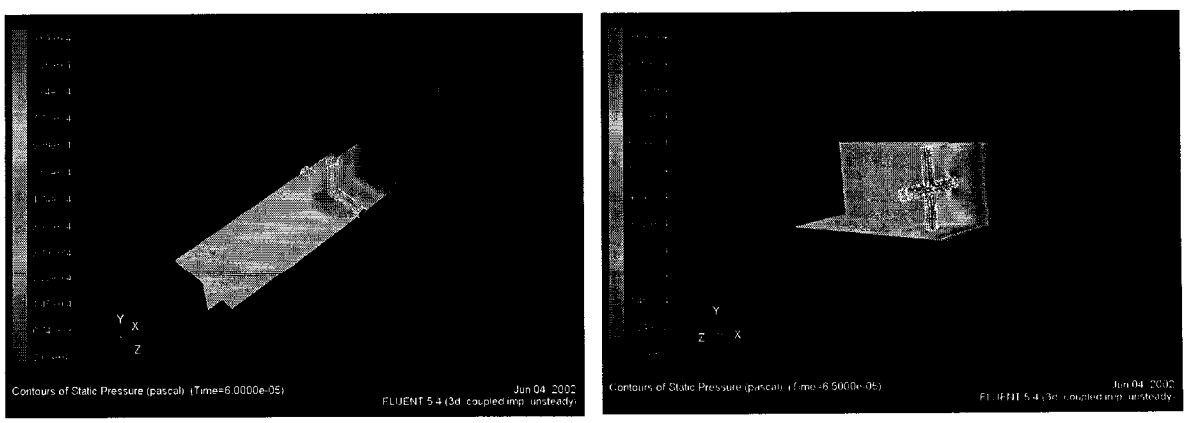

Figures 3.1a,b: Reflected and transmitted shocks over four [4] meshes in a typical grid.

FLUENT; a computational fluid dynamics (CFD) package for capturing the reflected shock wave off the grid as well as the shock wave signature downstream after it has passed through the grid. Figure 3.1a and figure 3.1b clearly illustrate the reflected and transmitted shocks.

Figure 3.2a and Figure 3.2b show sequential frames of the static pressure distribution inside the flow field. The frames of this animation are 2.5 ms apart. The flow field around one basic cell of the flow is shown only. As the incident shock impacts the grid regions of high pressure, they are shown upstream of the grid and are indicative of the formation of a reflected shock traveling upstream. The reflected shock is generated during the impact at the surface of the grid and it travels upstream as a three-dimensional highly distorted disturbance. It acquires its planar form within one mesh size, M, upstream of the grid. Part of the incident goes through the opening of the grid and part goes around the rods where it is reflected. The transmitted shock has also been distorted during its passage through the grid. Any flow inhomogeneities downstream of the grid and behind the shock seem to disappear when the shock is at a distance of about 5 mesh sizes, M. When the shock wave leaves the computational domain, a system of expansion waves is generated which travels upstream. The basic characteristic of this system is that it has low pressure behind it with no inhomogeneities. The major conclusion of this inviscid work is that the distortions of the transmitted and reflected shocks that result from the impact of the incident shock wave on the grid are decaying fast and that both shock waves appear to become planar within a few mesh sizes from the grid. Qualitatively these findings agree rather well with experimental evidence, which has shown that the shock recovers its initial shape within about one shock tube diameter after it is distorted by the grid.

The results of the CFD work should be always considered within the limitations of an inviscid calculation. The effects of viscosity, however, are expected to even out possible flow inhomogeneities much faster than what an inviscid calculation can show.

In that context the present qualitative results should be valid. Further comments on the onset of homogeneity will be discussed later while the RNG k-ϵ viscous turbulent model was used to analyze the experimental flows.

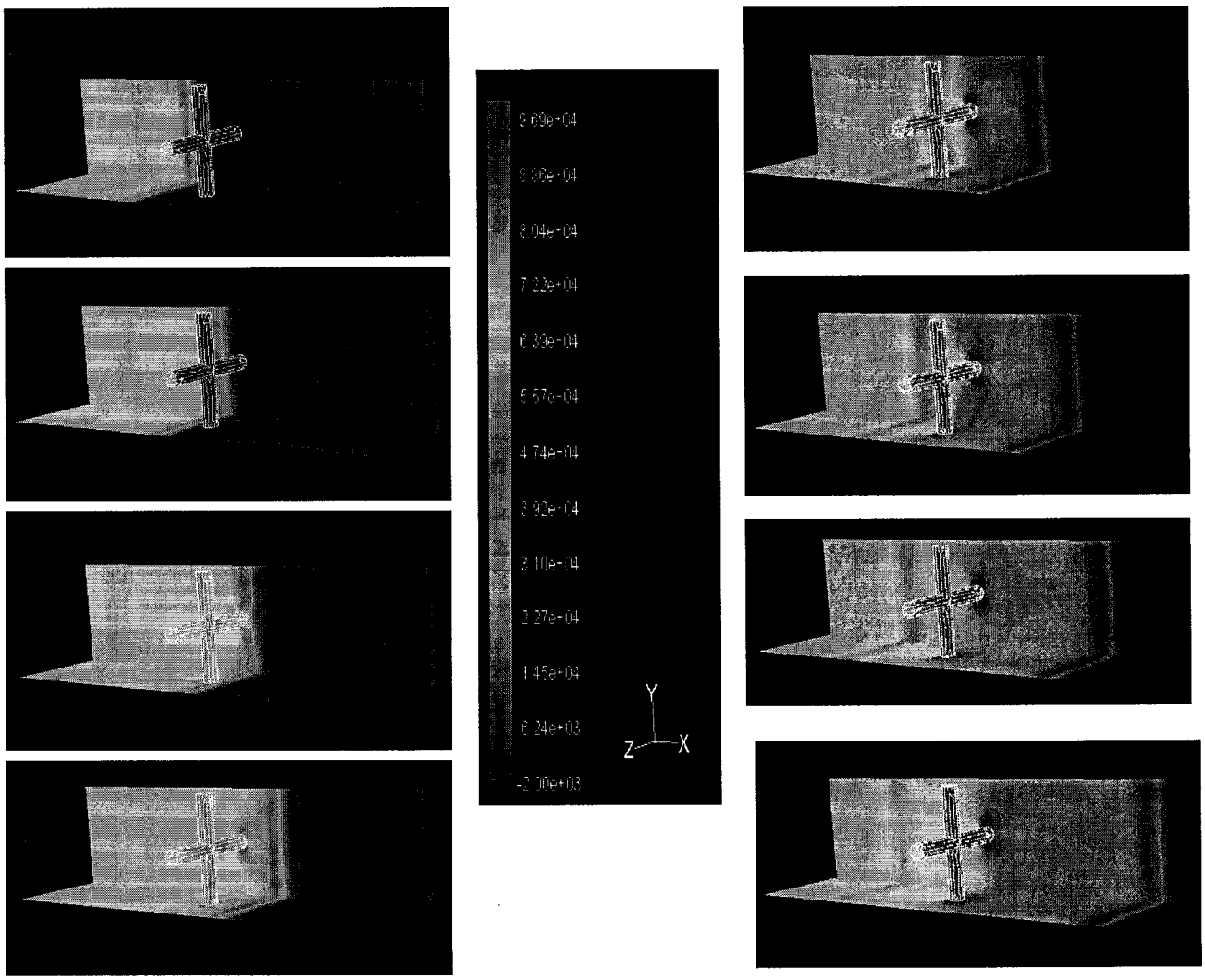

Images 1-4 From Top to bottom.

Images 5-8 From Top to bottom.

Figure 3.2a: CFD Calculations. Evolution of static pressure distribution inside flow domain. Frames are 2.5 ms apart. Images 1-8.

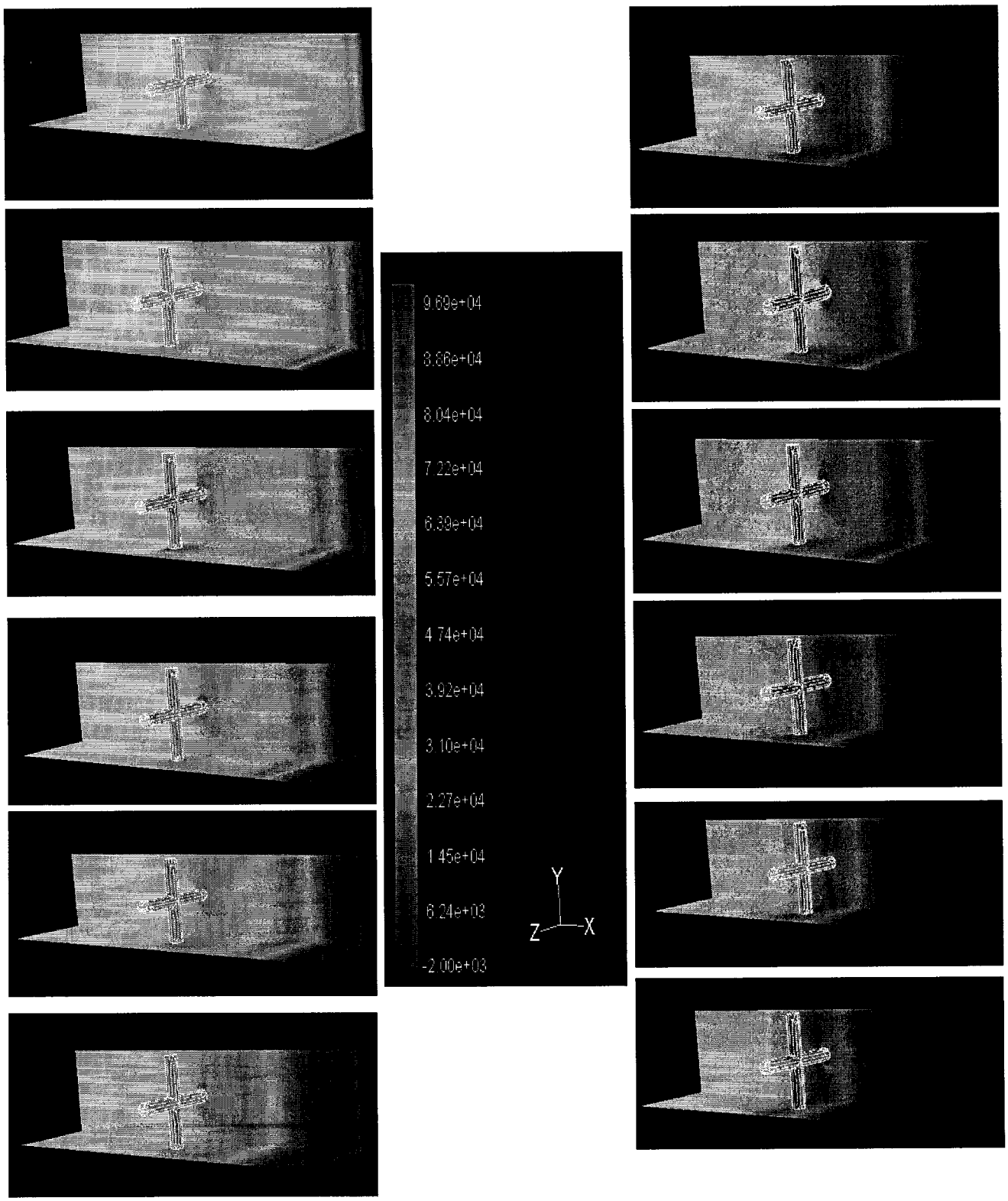

Images 9-14 From Top to

Images 15-20 From Top to bottom.

Figure 3.2b: CFD Calculations. Evolution of static pressure distribution inside flowfield. Frames are 2.5 ms apart. Images 9-20.

Figure 3.3 shows the normalized pressure drop obtained experimentally across the Grid versus the Reynolds number computed based on the grid mesh size, Re_M. The pressure drop across the grid remains relatively constant in the range of 12%. This pressure drop can be expressed in terms of the coefficient K defined as:

$$K = \frac{\Delta P}{\frac{1}{2}\rho U^2}$$

where ΔP is the difference between the pressure behind the incident shock and the pressure behind the transmitted shock.

According to Xanthos et al.[25], this coefficient is expected to be a function of the flow Mach number, M_2, the Reynolds number based on the mesh size M, Re_M and the solidity of the grid σ, i.e. $K = K(M_2, \mathrm{Re}_M, \sigma)$.

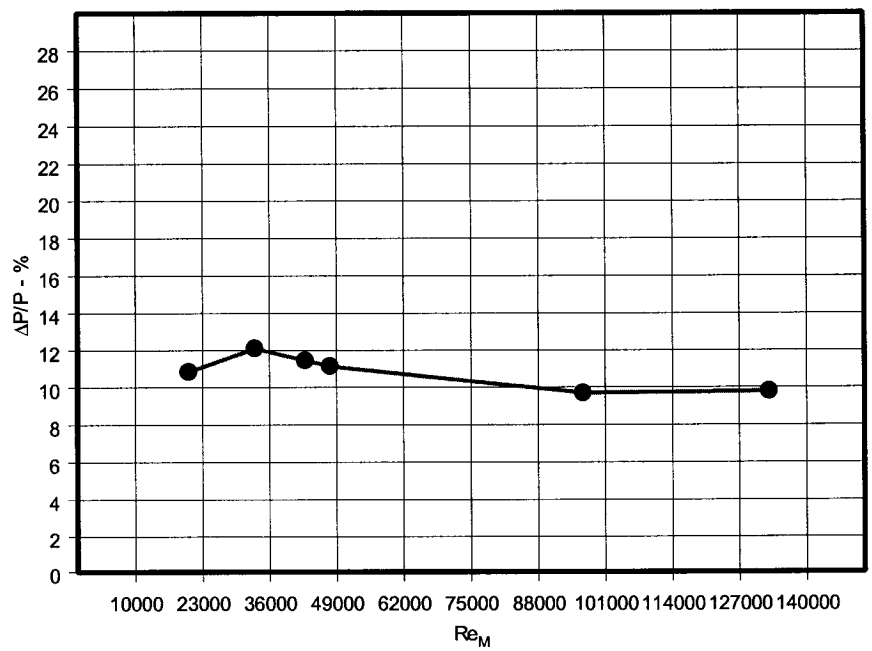

Figure 3.3: Experimental Data Pressure drop across Grid vs. Re_M.

Following the work of Laws and Livesey[26] and Groth & Johansson[27] for incompressible flows through fine grids, the dependence of solidity can be isolated from M_2 and Re_M as $K = f(M_2, Re_M)F_\sigma$. Taylor & Davies[28] suggested that the factor F_σ, which in general contains the effects of grid geometry, could be expressed in terms of the solidity σ as $F_\sigma = [\frac{1}{(1-\sigma)^2} - 1]$, since solidity is the dominant geometrical characteristic in the present case. Then, it appears that $K = f(M_2, Re_M)[\frac{1}{(1-\sigma)^2} - 1]$.

Figures 3.4a and 3.4b demonstrate a visual association of two grids with the same size yet with a different solidity value:

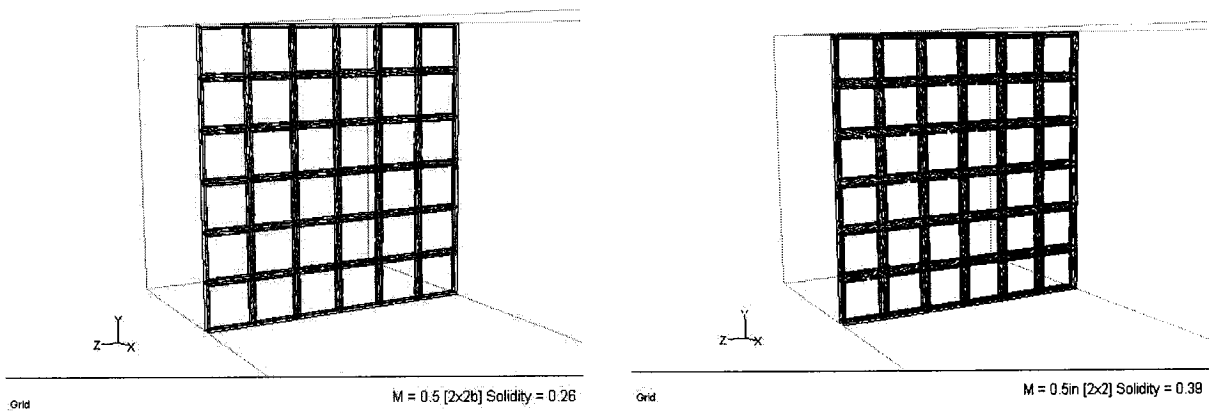

Figures 3.4a,b: Visual association of two grids with the same size, different solidity.

Figures 3.5 and 3.6 demonstrate the effects of grid solidity on the transmitted shock wave strength for the 2x2 grid (M = 12.7 mm) with $\sigma = 0.28$ and the 4x4 grid (M = 6.35 mm) with $\sigma = 0.44$ respectively.

These figures show experimental data of the mean pressure distribution along the wall of the working section. The longitudinal distance from the grid has been non-dimensionalized by the mesh size M of each grid. In both cases with the two different

grids, the incoming shock wave and flow have the same strength and Mach numbers respectively. The data in figure 3.5 indicate a pressure drop across the grid $\frac{\Delta P}{P}$ of about 10% while the corresponding value of F_σ is 0.929. The data in Figure 3.6 show a pressure drop, $\frac{\Delta P}{P}$, of about 16% with $F_\sigma = 2.18$. In this particular case with the same M_2 for both experiments, the function $f(M_2, Re_M)$ depends on Re_M only, i.e. $f(Re_M)$.

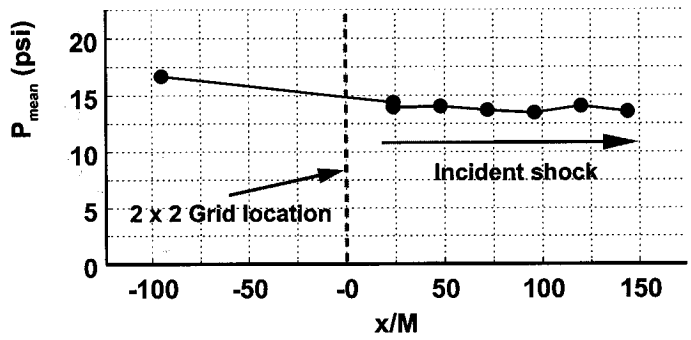

Figure 3.5: Mean pressure distribution at P_4/P_1=3.74 for 2x2b grid, σ = 0.28.

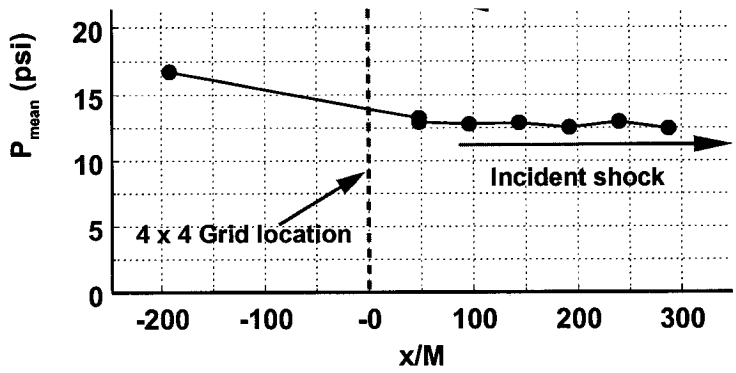

Figure 3.6: Mean pressure distribution at P_4/P_1 = 3.74 for 4x4 grid, σ = 0.44.

The Re_M for the 2x2b grid is twice the Re_M of the 4x4 grid. According to Pinker & Herbert[29] the function $f(M_2, Re_M)$ decreases by about 30 percent for this increase in Re_M. Thus, the pressure drop coefficient K is expected to be higher in the grid with high

solidity by about the ratio (1/1.3) F_σ^{4x4} / F_σ^{2x2} ≅ 1.7, a value which is close to the experimental data presented here as well as the CFD modeled results tabulated in Table 3.2 in the later section. This is consistent with the experiments performed in the shock tube's 8ft working section described in Figure 2.7 where grids are used. In all experiments with various grid sizes, the transmitted shock through the grid had to have the same strength. This was achieved by slightly readjusting the incident shock strength to account for the difference in pressure drops across the various grids so that the pressure behind the transmitted shock remained practically the same.

In order to explore the bulk behavior of the present quasi-steady flow behind the incident shock wave, through and downstream of the grid, a full three-dimensional version of the renormalization group (RNG) of the basic two-equation steady state k-epsilon (k-ϵ) model was used. The k-ϵ model is an eddy viscosity (μ_t) model, which solves approximate transport equations for the turbulent kinetic energy (k) where $k = \frac{1}{2}(\overline{u'^2} + \overline{v'^2} + \overline{w'^2})$ and the turbulent dissipation rate (ϵ) which is defined as the rate at which k decays and then calculates the eddy viscosity μ_t: $\mu_t = \rho C_\mu \frac{k^2}{\varepsilon}$

The Renormalization group (RNG – k-ϵ) is similar in form to the standard k-ϵ model yet the empirical coefficients used in the k-ϵ model are estimated theoretically from the RNG theory. The more elaborate modeling represented by this model seems to outperform the simpler "basic k-ϵ model"; an attribute that directed our analysis to this type of turbulence model. Very dense computation grids were set up to simulate each experimental flow case placing all parameters and boundary conditions the same for

correct and reliable modeling. Table 3.1 provides mesh information on individual computational grids.

Grid	Mesh Size-mm	Solidity σ	Number of Tetrahedral Cells	Number of Nodes
2x2a	12.7	0.39	807473	158178
2x2b	12.7	0.28	739382	142932
3x3	8.50	0.39	904518	172929
4x4	6.35	0.44	953472	181898
5x5	5.10	0.37	920508	174971
8x8	3.175	0.36	905633	172777

Table 3.1: Mesh information on individual computational grids.

The pressure drop through the various grids was initially obtained along the working section and compared with the results obtained experimentally.

Figure 3.7 shows a typical grid with the planes of symmetry visibly meshed for a three dimensional effect. Table 3.2 provides the parameters for the CFD calculation used to evaluate the percent pressure drop through the grids based on the experimental characteristics of the flow.

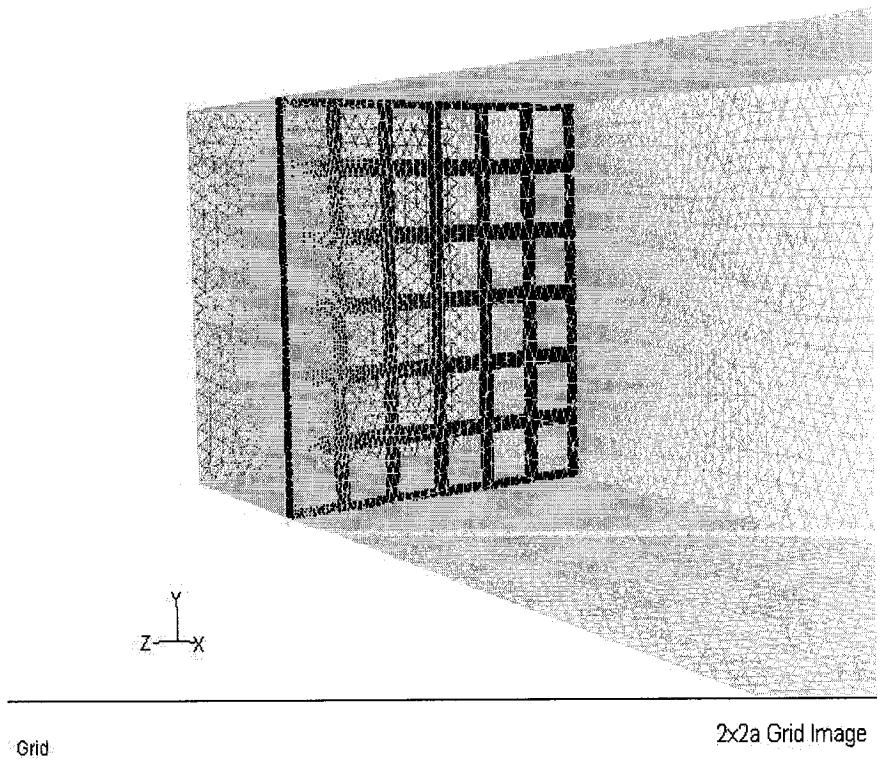

Figure 3.7: 2x2a meshed Grid.

Grid (Meshes /in)	M Mesh size (mm)	Solidity σ	M_2 Flow Mach Number	P_4 psi	Re_M	P_{2g_m} P41 Theory (psi)	P_{2g_m} Upstr. of Grid (psi)	P_{2g_m} Downstr. of Grid (psi)	ΔP/P %	K
2 x 2a	12.7	0.39	0.30	35	122838	7.660	7.95	6.95	**12.58**	**0.753**
2 x 2a	12.7	0.39	0.34	40	147948	9.100	9.60	8.40	**12.50**	**0.650**
2 x 2a	12.7	0.39	0.41	50	193898	11.65	12.75	10.25	**19.61**	**0.845**
2 x 2a	12.7	0.39	0.51	70	273381	15.91	18.50	13.50	**27.03**	**0.940**
2 x 2b	12.7	0.28	0.30	35	122838	7.660	7.90	7.20	**8.86**	**0.527**
2 x 2b	12.7	0.28	0.34	40	147948	9.100	9.40	8.45	**10.11**	**0.515**
2 x 2b	12.7	0.28	0.41	50	193898	11.65	12.35	10.60	**14.17**	**0.592**
2 x 2b	12.7	0.28	0.51	70	273381	15.91	17.75	14.25	**19.72**	**0.658**
3 x 3	8.50	0.39	0.30	35	82214	7.660	7.95	6.80	**14.47**	**0.866**
3 x 3	8.50	0.39	0.34	40	99020	9.100	9.60	8.00	**16.67**	**0.867**
3 x 3	8.50	0.39	0.41	50	129774	11.65	12.85	10.00	**22.18**	**0.963**
3 x 3	8.50	0.39	0.51	70	182972	15.91	19.00	13.00	**31.58**	**1.129**
4 x 4	6.35	0.44	0.30	35	61419	7.660	8.00	6.80	**15.00**	**0.903**
4 x 4	6.35	0.44	0.34	40	73974	9.100	9.60	8.00	**16.60**	**0.867**
4 x 4	6.35	0.44	0.41	50	96949	11.65	13.00	10.00	**23.08**	**1.014**
4 x 4	6.35	0.44	0.51	70	136691	15.91	19.00	13.00	**31.58**	**1.129**
5 x 5	5.10	0.37	0.30	35	49328	7.660	8.00	6.90	**13.75**	**0.828**
5 x 5	5.10	0.37	0.34	40	59412	9.100	9.70	8.10	**16.49**	**0.867**
5 x 5	5.10	0.37	0.41	50	77865	11.65	12.75	10.25	**19.61**	**0.845**
5 x 5	5.10	0.37	0.51	70	109783	15.91	19.00	13.50	**28.95**	**1.034**
8 x 8	3.175	0.36	0.30	35	30709	7.660	8.00	7.10	**11.25**	**0.678**
8 x 8	3.175	0.36	0.34	40	36987	9.100	9.60	8.35	**13.02**	**0.677**
8 x 8	3.175	0.36	0.41	50	48475	11.65	12.60	10.50	**16.67**	**0.710**
8 x 8	3.175	0.36	0.51	70	68345	15.91	18.50	13.75	**25.68**	**0.893**
1.3x1.3	19.10	0.26	0.30	35	184741	7.660	7.88	7.30	**7.36**	**0.437**
1.3x1.3	19.10	0.26	0.34	40	222504	9.100	9.60	8.80	**8.33**	**0.433**
1.3x1.3	19.10	0.26	0.41	50	291611	11.65	12.30	11.25	**8.54**	**0.355**
1.3x1.3	19.10	0.26	0.51	70	411148	15.91	17.50	15.25	**12.86**	**0.423**

Table 3.2: Parameters for the Pressure Drop through the grids by CFD.

Before representing the results of these computations, the lines along which the results were obtained with respect to the whole three dimensional domain should be made clear since they are referenced in the legend of each set of results. Figures 3.8 and 3.9 provide information on 36 cells [6x6] utilized for the creation of the computational gird.

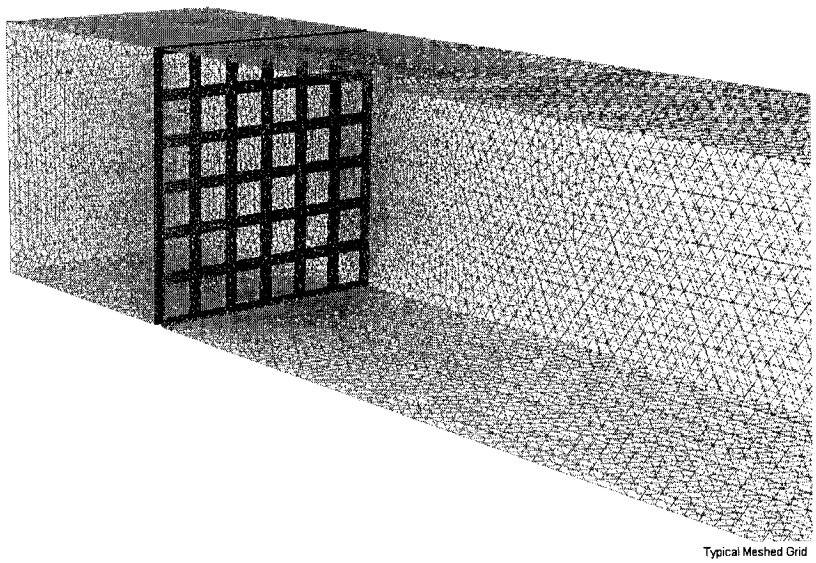

Figure 3.8: Three dimensional domain with symmetry planes visible.

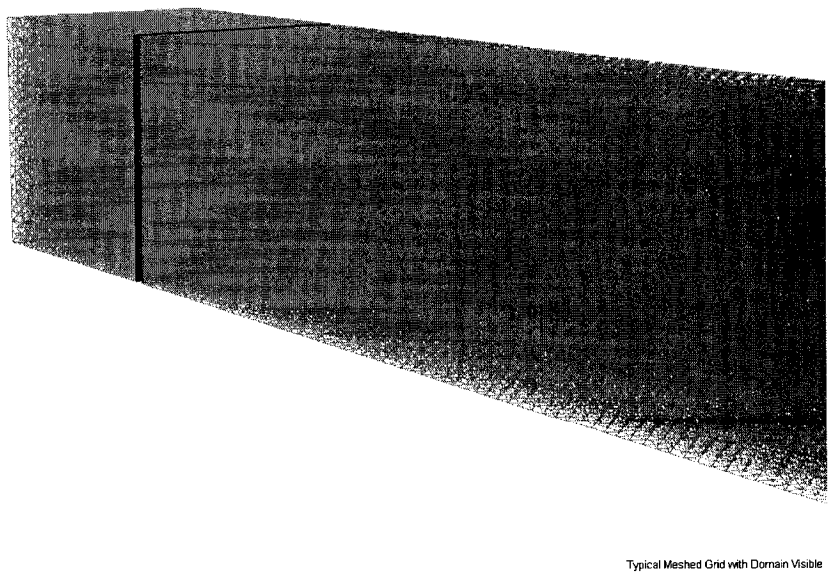

Figure 3.9: Three-dimensional domain with interior visible.

The planes here shown are symmetry planes since in the 12-inch grids utilized for the experiments, the number of total cells varied from 12x12 to 100x100.

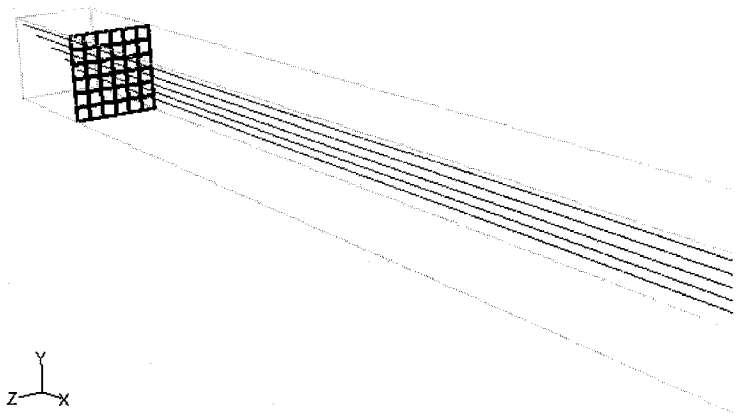

Figure 3.10a: Lines along X with constant Y and Z.

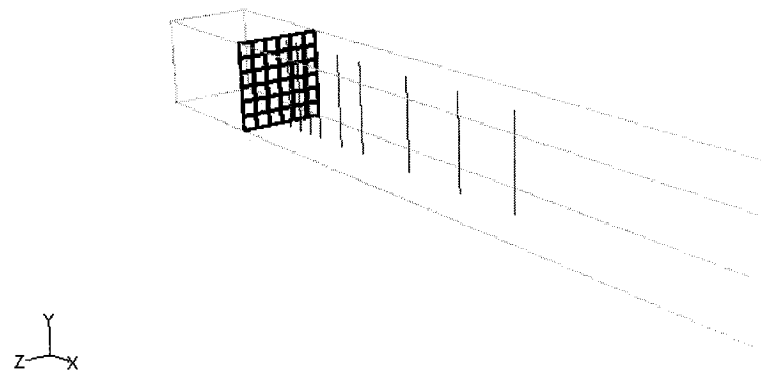

Figure 3.10b: Lines along Y with constant Z and X.

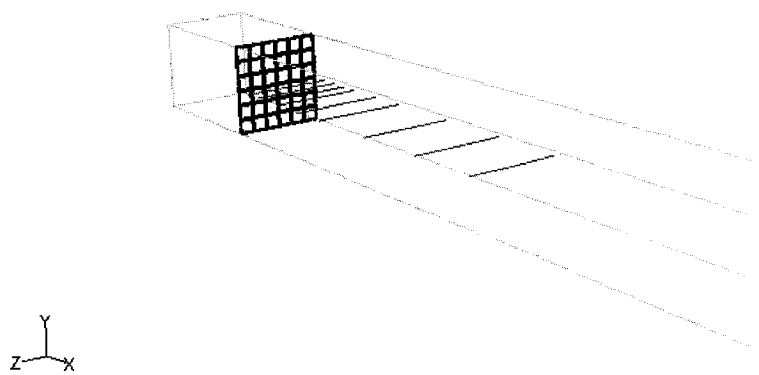

Figure 3.10c: Lines along Z with constant Y and X.

All the result windows include in their legend a description of lines with the format of "**line(i) (j) (#) (k) (#)**"; i, j, k taking the values of x, y, and z coordinates and (#) is the numerical value of displacement [in inches] of the line along which the results were obtained with respect to the grid coordinate system located at the center of the grid. For example "**linex y-0.25z-0.25**" indicates lines along the x-direction [refer to Figure 3.10a-c] with a value of [-0.25in] displacement along the y and z directions from the center of the grid. Figure 3.11 shows a typical static pressure drop [in psi] along the length of the working section where position [0 inches] indicates the location of the grid. The flow through the grid is similar to the flow through a converging-diverging nozzle of relative short length. The pressure reaches a minimum at the minimum cross section location, where the velocity is at maximum.

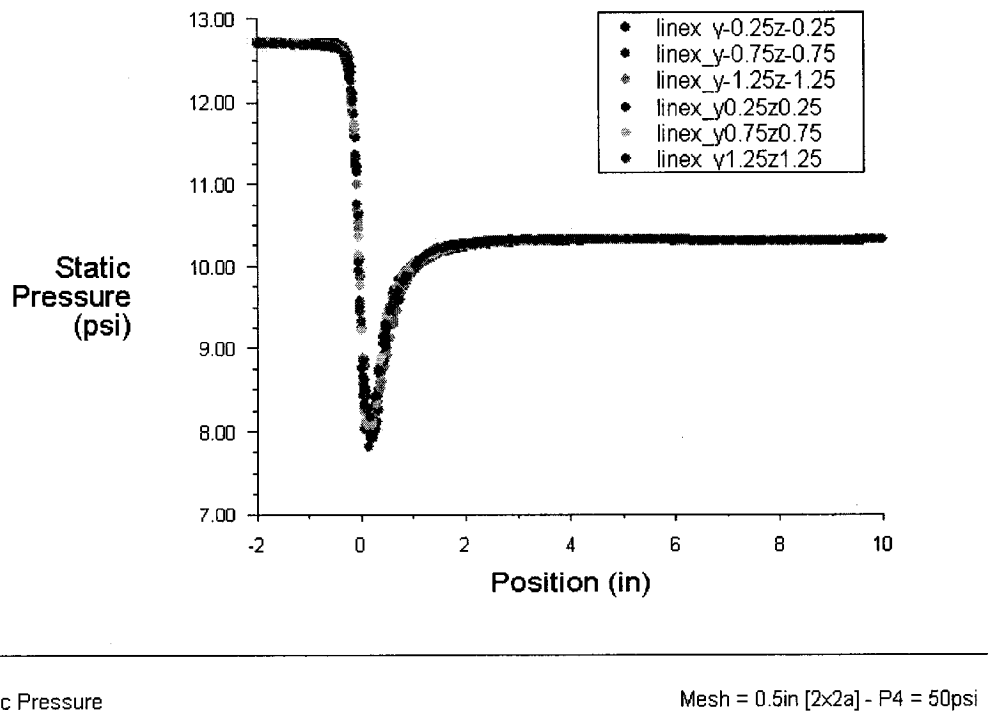

Figure 3.11: Static Pressure drop through the 2x2a grid, P4 = 50psi.

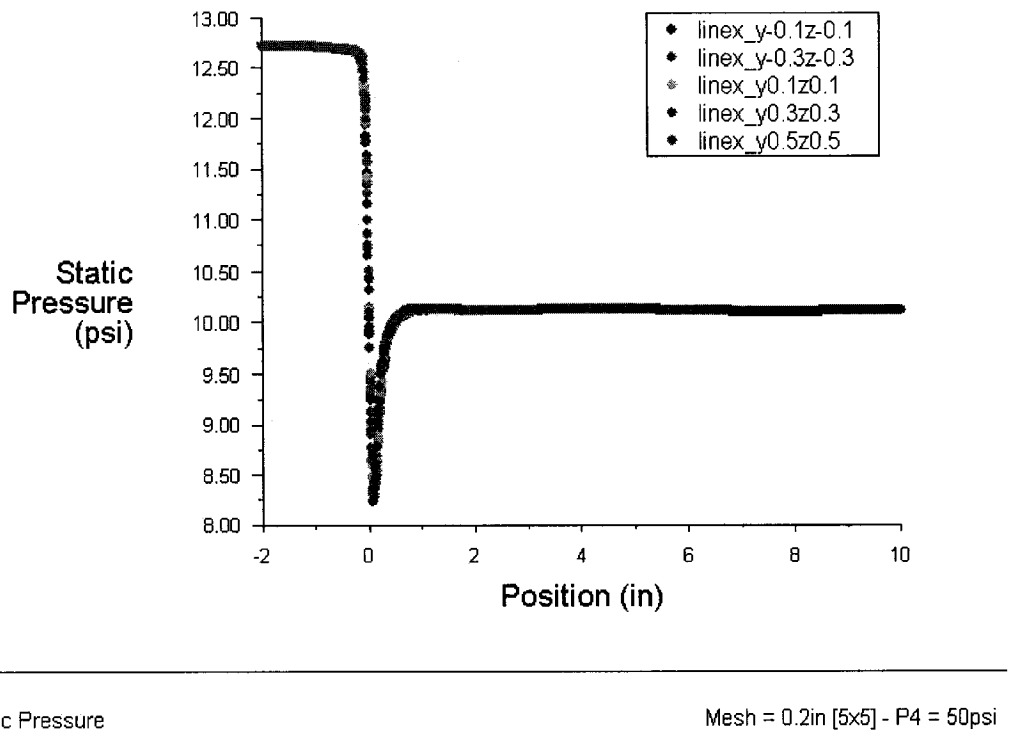

Figure 3.12: Static Pressure drop through the 5x5 grid, P4 = 50psi.

In Table 3.2, $\frac{\Delta P}{P}$ column summarizes the percentage pressure drop through the grids based on the CFD computations. Prior to plotting these results, a quantitative comparison based on the experimental results previously shown in Figures 3.5 and 3.6 can be quickly pointed out. The first set of experimental data indicate a pressure drop $\frac{\Delta P}{P}$ across the grid of about 10% while the CFD calculation predicts a pressure drop $\frac{\Delta P}{P}$ across the 2x2 grid of 10.11% [see first underlined field in the table]. The second set of experimental data indicate a pressure drop $\frac{\Delta P}{P}$ across the grid of about 16% while the CFD calculation

predicts a pressure drop $\frac{\Delta P}{P}$ across the 4x4 grid of 16.60%. Moreover the pressure drop coefficient K based on the CFD results indicates a higher value due to the solidity by the ratio of 1.68, which is comparable with the results obtained experimentally.

The results of Table 3.2 are now presented here under Figures 3.13- 3.16. Figure 3.13 shows the relative pressure drop as a function of Re_M for each grid. A limited comparison with experimental data is also attempted in this figure. The CFD results indicate that for a low value of solidity σ, the pressure drop $\frac{\Delta P}{P}$ is weakly affected with increasing value of Re_M. At values of solidity $\sigma > 0.3$, $\frac{\Delta P}{P}$ is strongly affected and indicates an increased values with an increase in Re_M. The experimental data appear to be close to the computed values by the CFD modeling only in the cases of low solidity σ and low Re_M. In general the CFD data over predicts the experimental results.

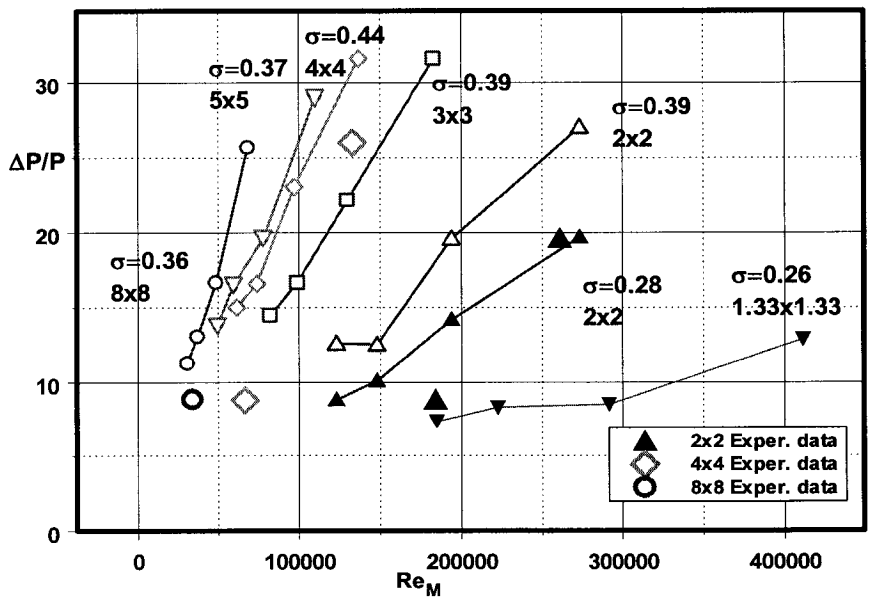

Figure 3.13: $\frac{\Delta P}{P}$ versus Reynolds number based on Mesh size. CFD results along with experimental points for comparison.

Figure 3.14 show the dependence of $\frac{\Delta P}{P}$ on the flow Mach number M_u as it is predicted by CFD. It appears that $\frac{\Delta P}{P}$ increases with M_u in almost all cases with different grids.

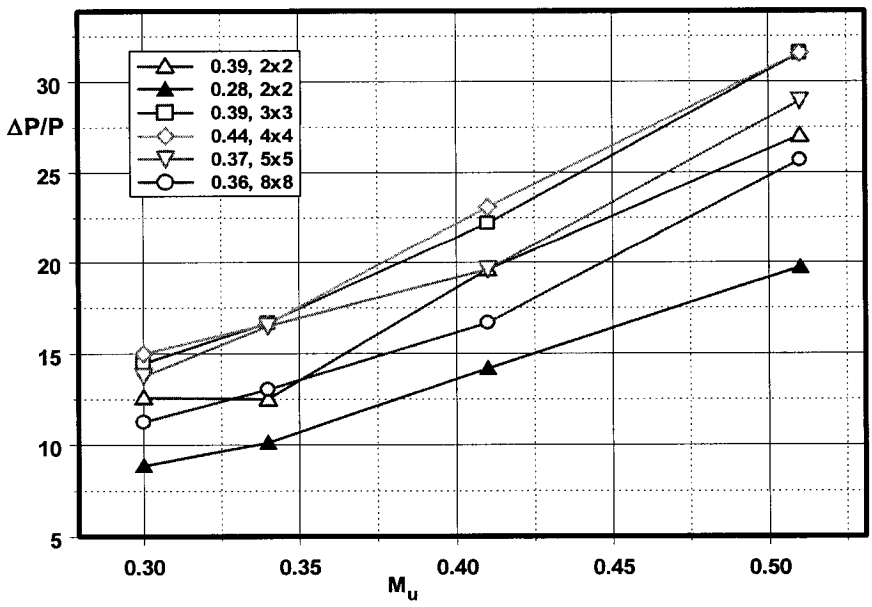

Figure 3.14: CFD results of $\frac{\Delta P}{P}$ versus flow Mach number [M_u].

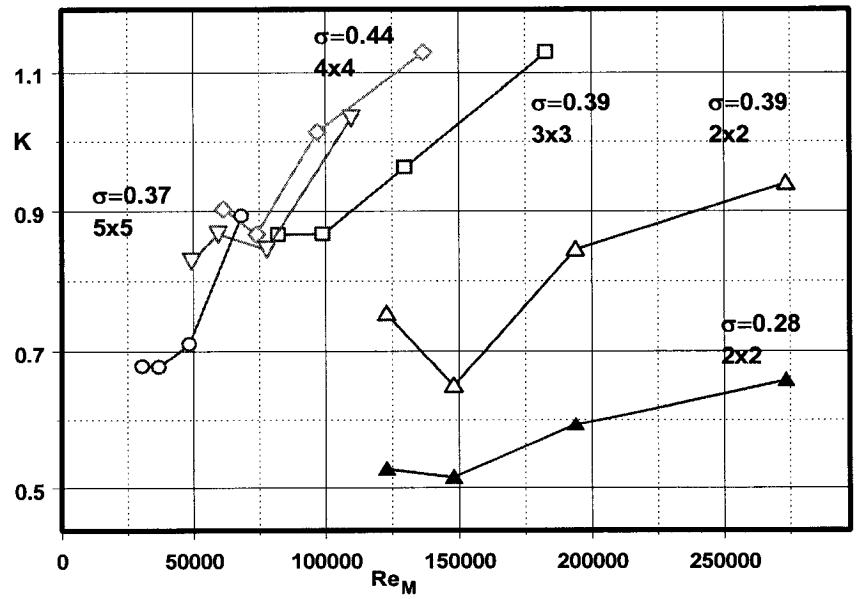

Figure 3.15: CFD results of K versus Reynolds number based on Mesh size.

The predicted values of the pressure drop coefficients [K] are shown in Figures 3.15 and 3.16. The value of K increases with an increased value of both M_u and Re_M. Larger values of K were computed in the cases of higher solidity values, which indicates that K is highly dependent on solidity.

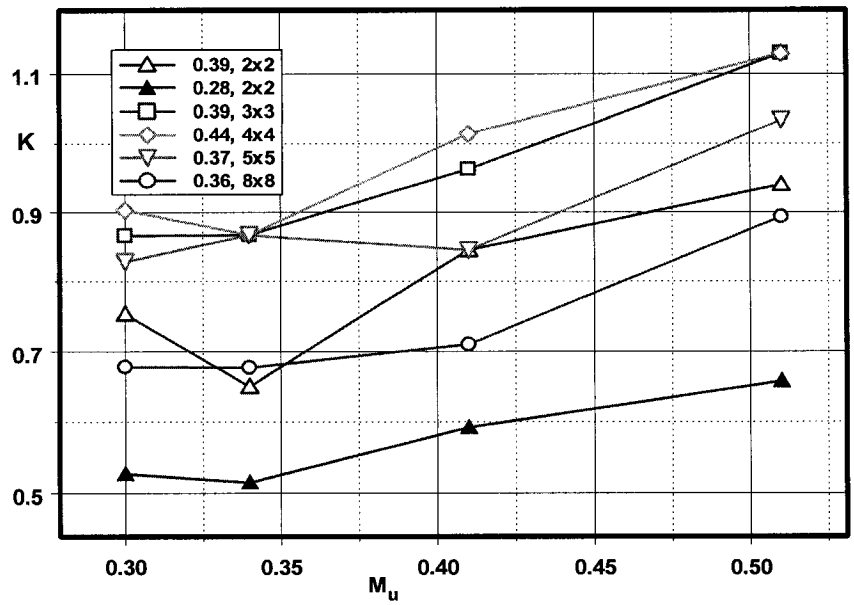

Figure 3.16: CFD results of K versus flow Mach number [M_u].

The pressure drops along the grids based on a different experiment set than the ones referred to in Figures 3.5 and 3.6 are tabulated in Table 3.3. The CFD computations allowed the study of the pressure drop along the grids as was seen in the previous section. Moreover the onset of homogeneity downstream the grid is of vital importance if one is to investigate the expansion wave interaction with homogeneous turbulence downstream a grid flow. Interestingly enough these CFD [RNG k-ϵ and LES] computations provided a prediction on the onset of this occurrence, which is tabulated in Table 3.4 as well.

Grid (Meshes /in)	M Mesh size (mm)	Solidity σ	M_2 Flow Mach Number	P_4 (psi)	Re_M	P_{2g_m} Theory (psi)	P_{2g_m} Upstr. of Grid (psi)	P_{2g_m} Downstr. of Grid (psi)	ΔP/P %	K
2x2b	12.70	0.28	0.56	84	322543	18.44	21.45	19.36	9.74	0.298
2x2b	12.70	0.28	0.39	47	184317	10.92	12.59	11.37	9.69	0.457
4x4	6.35	0.44	0.31	37	66577	8.25	9.52	8.68	8.82	0.548
4x4	6.35	0.44	0.53	76.5	148110	17.12	19.48	17.59	9.70	0.310
5x5	5.10	0.37	0.48	64	101028	14.73	23.86	21.19	11.19	0.579
5x5	5.10	0.37	0.43	54.2	85217	12.63	14.58	12.90	11.52	0.487
8x8	3.175	0.36	0.56	85.5	81843	18.7	21.28	18.72	12.03	0.356
8x8	3.175	0.36	0.32	37.5	33926	8.40	9.38	8.55	8.85	0.524

Table 3.3: Experimental Pressure drops across different grids

The flow through a grid has similar characteristics with the flow through a very short nozzle. The flow accelerates suddenly in the beginning and then decelerates slowly after it passes the throat of the grid and exits into the wake where it merges with flow exiting nearby cells. The flow in the near wake of the grid appears to be highly inhomogeneous. Mixing, however, in the wake brings about a homogeneous flow after some distance. The longitudinal and lateral derivatives of the mean longitudinal velocity U, $\frac{\partial U}{\partial x}$ and $\frac{\partial U}{\partial y}$ were used to determine the distance X_H where the deviation between the data of these quantities appear to be less than 2 percent of the maximum $\frac{\partial U}{\partial x}$ peak to peak value which takes place at the throat of the grid. The last column in Table 4, with the values of

$\frac{X_H}{M}$, indicates that the flow becomes homogeneous within a distance of 10 to 25 mesh sizes downstream of the grid. There are also some indications suggesting that the flow becomes homogeneous within a shorter distance in cases with higher Re_M. Similar qualitative information has been observed in the experimental work of Briassulis et al.[23]. The effect of solidity, in cases which Re_M remains the same (cases with grids 2x2a and 2x2b) can also be discerned from these data. Increasing solidity seems to increase $\frac{X_H}{M}$.

Grid	Solidity, σ	Pressure, P_4 psi	X_H in	X_H/M
2x2b	0.28	35	8	16
2x2b	0.28	50	5	10
2x2a	0.39	35	9	18
2x2a	0.39	50	9	18
3x3	0.39	35	6	18
3x3	0.39	59	8	24
4x4	0.44	35	4	16
4x4	0.44	50	4	16
5x5	0.37	35	3	15
5x5	0.37	50	2	10
8x8	0.36	35	3	24
8x8	0.36	50	3	24

Table 3.4: Homogeneity regions.

The results in Table 3.4 were obtained by examining sets of results for each computation with different grid and different boundary conditions which generated flow conditions as close to the ones obtained experimentally. Typical result sets are shown in Figures 3.17 – 3.27. Figures 3.17-3.18 show contours of X velocity [u] and velocity magnitude in the flow region through and downstream the grid. The individual wakes of each rod of the grids can be clearly seen. The flow through the grid is exiting the cell as a jet flow which interfaces with the rod's wake to create a highly inhomogeneous flow. The mixing however between the jet-like flow and the wake-like flow brings fluid from the high

momentum region to the low momentum region and vice versa resulting in a homogeneous region downstream the grid. Values of the longitudinal velocity derivatives $\frac{\partial U}{\partial x}$ along various y = constant and z = constant lines are shown in Figure 3.19. The flow as predicted accelerates and then decelerates downstream of the minimum cross sectional area. No substantial difference can be observed in the values of $\frac{\partial U}{\partial x}$ at these various locations. On the other hand significant differences on the lateral and transverse derivatives $\frac{\partial U}{\partial y}$ and $\frac{\partial U}{\partial z}$ can be observed, Figures 3.20 and Figure 3.21, in the near wake region of the grid where strong inhomogeneous flow is present. It is clearly seen that the later derivatives are of the same magnitude and decay at approximately 12-15 mesh sizes after the grid.

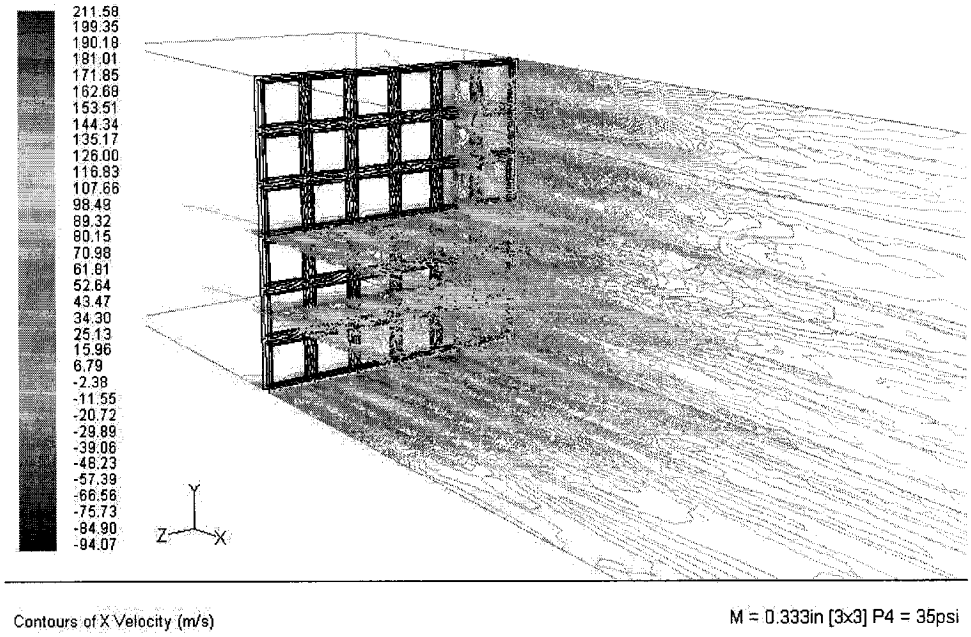

Figure 3.17: Contours of X Velocity [m/s] M=0.333in – P4 = 35psi.

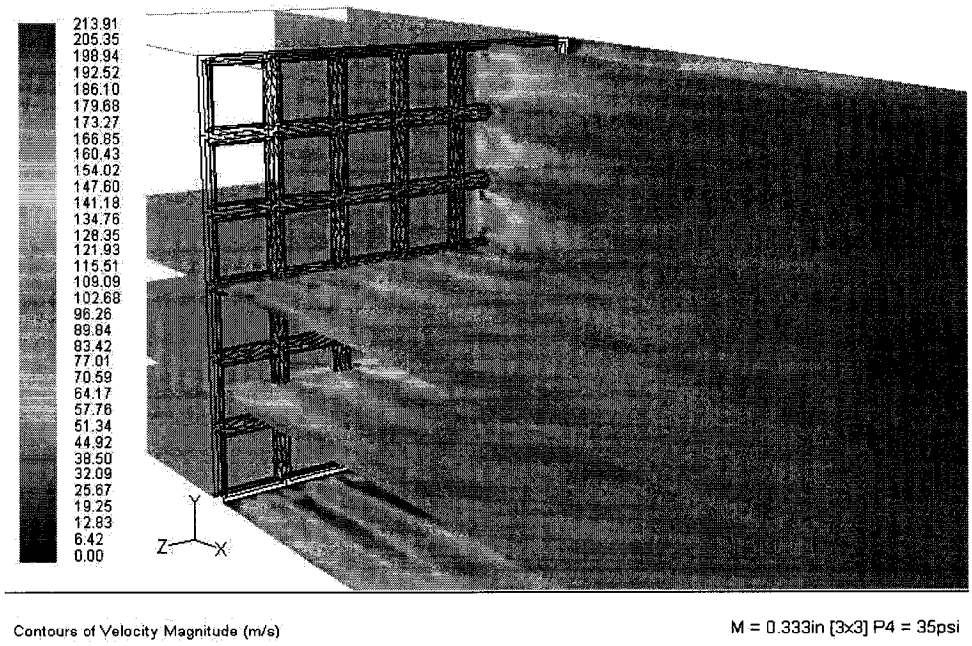

Figure 3.18: Contours Velocity Magnitude [m/s] M=0.333in – P4 = 35psi.

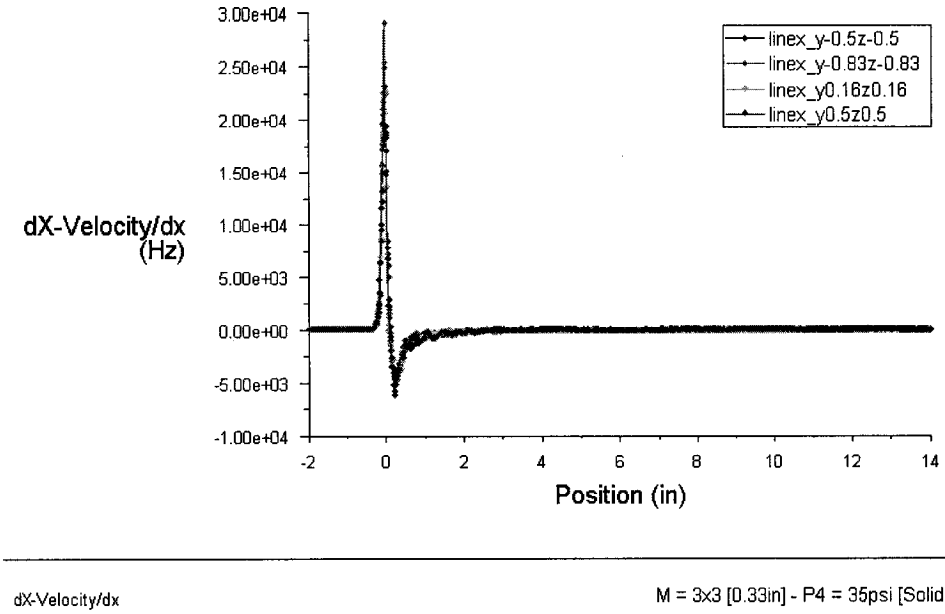

Figure 3.19: $\frac{\partial U}{\partial x}$ [Hz] versus distance downstream the grid - M=0.333in – P4 = 35psi.

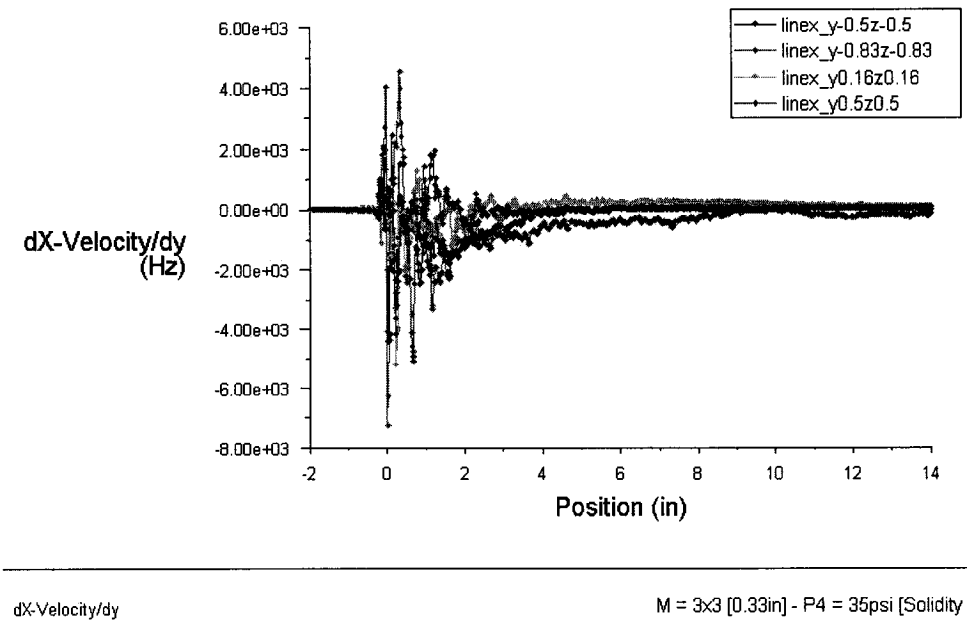

Figure 3.20: $\frac{\partial U}{\partial y}$ [Hz] versus distance downstream the grid - M=0.333in – P4 = 35psi.

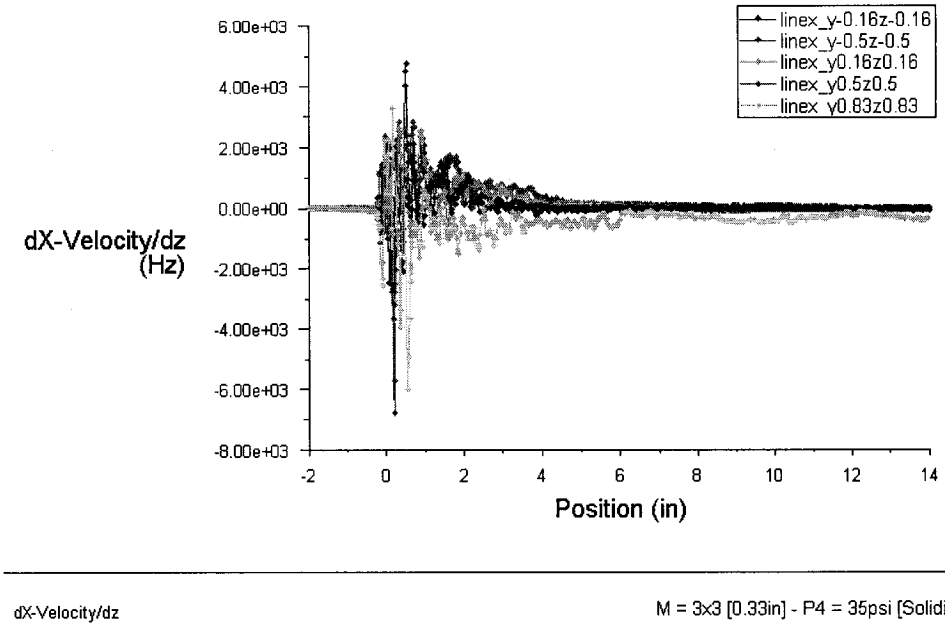

Figure 3.21: $\frac{\partial U}{\partial z}$ [Hz] versus distance downstream the grid - M=0.333in – P4 = 35psi.

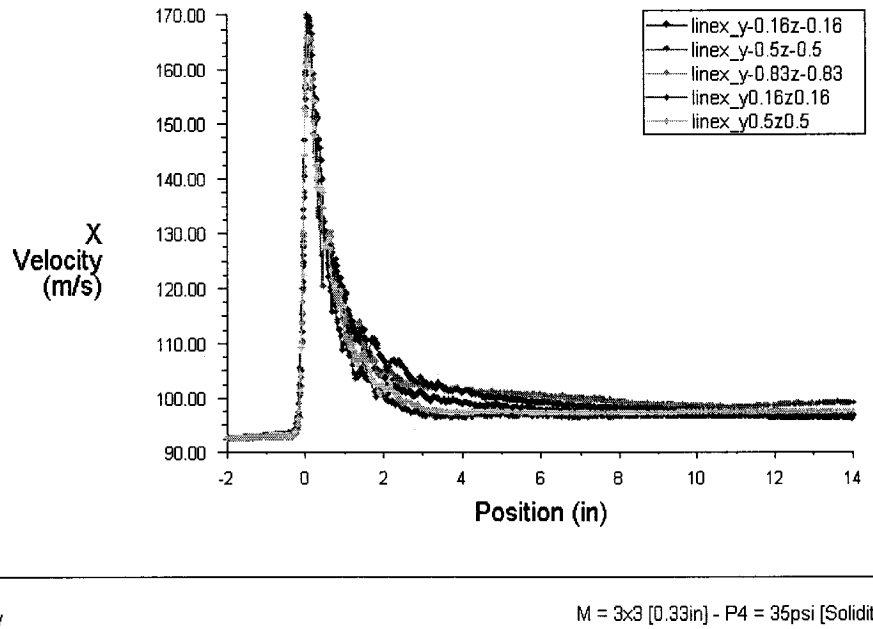

Figure 3.22: U_x Velocity [m/s] versus distance downstream the grid M=0.333in – P4 = 35psi.

Figure 3.22 depicts the computed flow velocity [u] after the grid and it is evident that the velocity magnitude downstream increases; this is mainly due to the pressure drop that was observed across the grid and discussed previously.

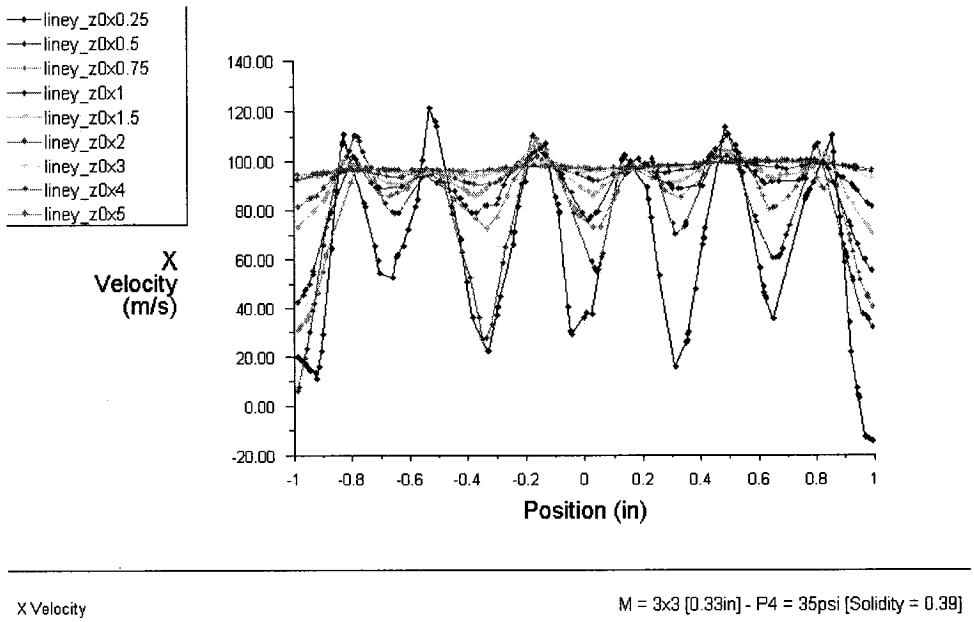

Figure 3.23: U_x Velocity [m/s] along the height of the grid [y-direction] - M=0.333in – P4 = 35psi.

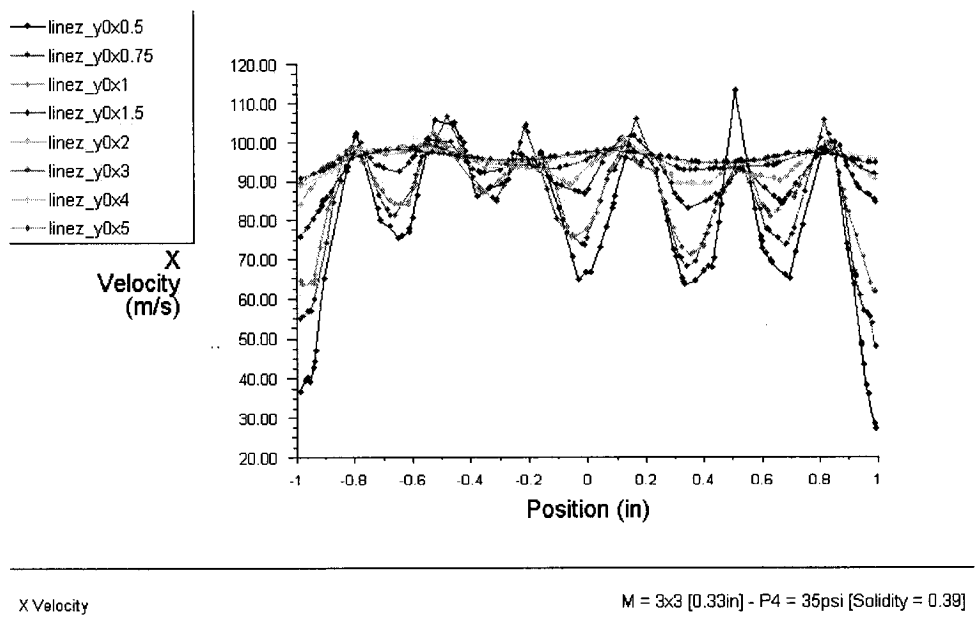

Figure 3.24: U_x Velocity [m/s] along the width of the grid [z-direction] - M=0.333in – P4 = 35psi.

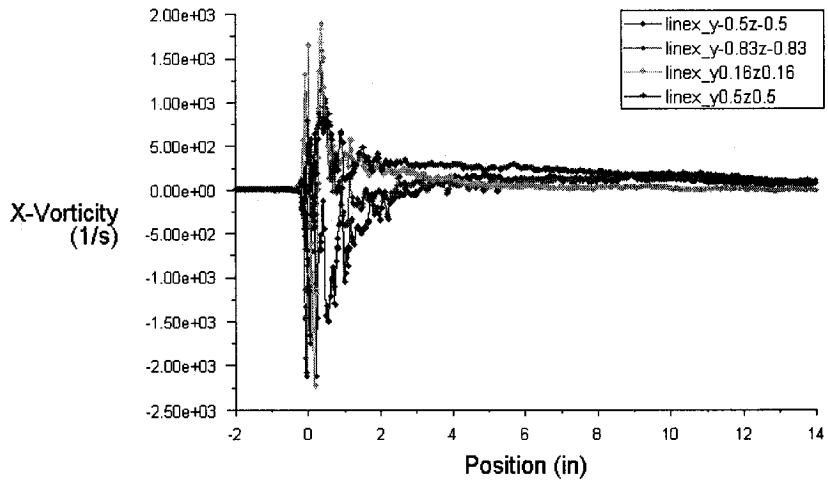

Figure 3.25: Vorticity - X [Hz] versus distance downstream the grid M = 0.333in – P4 = 35psi.

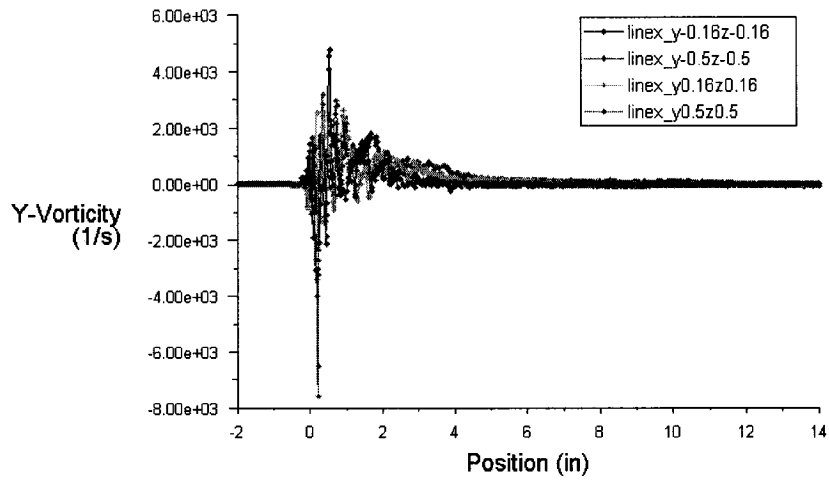

Figure 3.26: Vorticity - Y [Hz] versus distance downstream the grid M = 0.333in – P4 = 35psi.

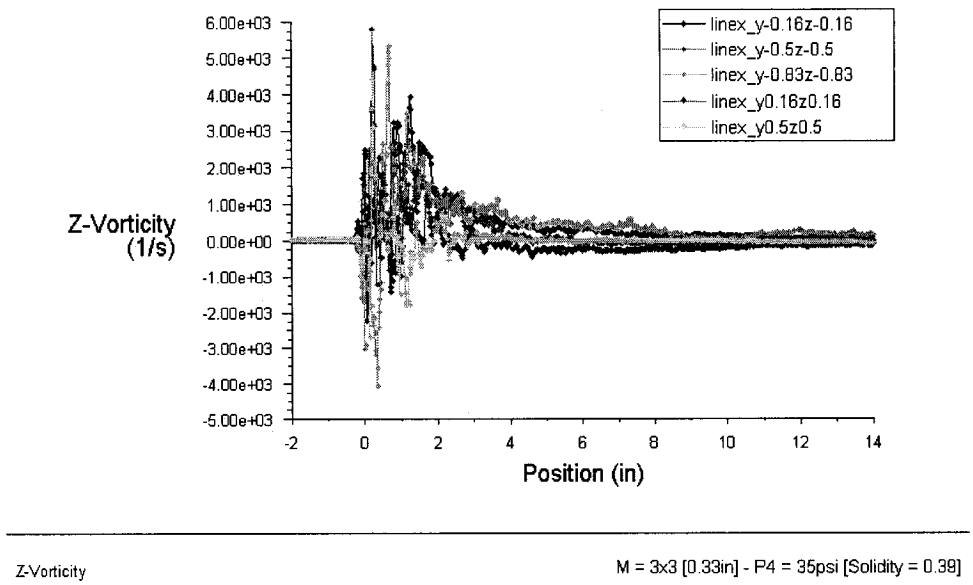

Figure 3.27: Vorticity - Z [Hz] versus distance downstream the grid M = 0.333in – P4 = 35psi.

Chapter 4: Total Variation Diminishing Scheme

4.1. Introduction to TVD Scheme

The objective of this research work as mentioned earlier was to investigate the potentially favorable effects of interaction of turbulence with expansion waves on the flow. In order to correctly identify the duration of the useful flow as well as the location of the true expansion wave – turbulence interaction, a predictive tool was developed based on the predictor-corrector Total Variation Diminishing (TVD) scheme. These simulations indicated the existence of two regions of traveling expansion waves (see Figure 4.1 and Figures 4.7, 4.8). The first one is generated immediately after the rupture of the diaphragm and travels in the opposite direction to that of the shock wave. It is reflected over the end wall of the driver section and then it travels in the same direction as the incident shock wave at a much higher speed due to the already induced flow.

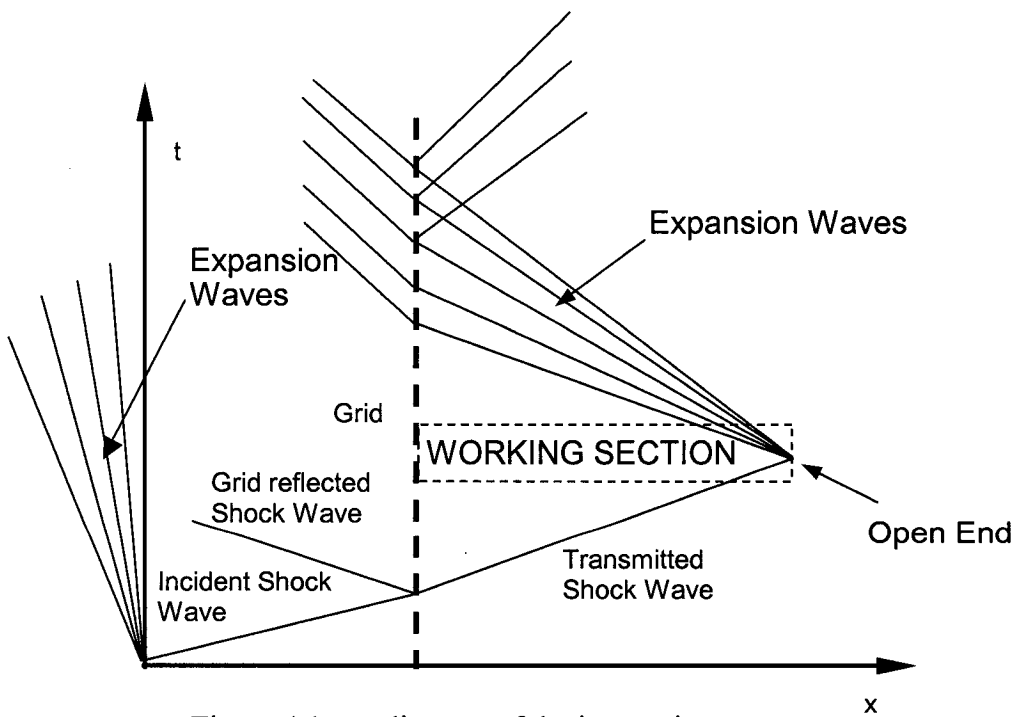

Figure 4.1: x-t diagram of the interaction.

The second system of expansion waves is generated at the open end of the driven section when the incident shock reflects over the open end of the shock tube's working section where the pressure is atmospheric. This system of expansion waves was utilized in the present experiments to interact with the induced flow behind the incident shock wave, which has traveled through a turbulence-generating grid. The grid was placed at the beginning of the working section, sizes of which are tabulated in Table 3.2. A brief description of the TVD scheme will be given here along with some results. These results created the benchmark along which the instrumentation, apparatus and in general the experimental setup [see chapter 5] was designed and fabricated on.

4.2. TVD Description

Starting from the governing equations, with initial and boundary conditions given, the flow is monitored through different time process.

Physical meanings of some parameters used

a_1: Sonic Speed downstream of the shock.

M_s: Mach number of the shock.

p_1: Pressure of the downstream of the shock.

p_2: Pressure of the upstream of the shock.

T_1: Temperature of the downstream of the shock.

T_2: Temperature of the upstream of the shock.

ρ_1: Density of the downstream of the shock.

ρ_2: Density of the upstream of the shock.

R: Gas constant.

u_1: Flow velocity of the downstream of the shock.

u_2: Flow velocity of the upstream of the shock.

dt: Time interval.

dx: Grid size.

4.2.1. Governing Equations

A Quasi-one-dimensional problem can be expressed by the Euler Equation as:

$$\frac{\partial \omega}{\partial t} + \frac{\partial f(\omega)}{\partial x} = 0$$

where $\omega = \begin{cases} \rho \\ m \\ e \end{cases}$, $f(\omega) = \begin{cases} m \\ \frac{m^2}{\rho} + p \\ \frac{m}{\rho}(e+p) \end{cases}$,

x: Eulerian position.
t: Time.
ρ: Density.
m: Momentum.
e: Total unit energy.

The following relations exist, $m = \rho u$ and $e = \frac{p}{\gamma - 1} + \frac{1}{2}\rho u^2$

Where **u:** Velocity.
p: Pressure of the fluid respectively.

4.2.2. Initial Conditions

$\mathbf{u}(x, t = 0) = 0$
$\mathbf{p}(x < d, t = 0) = p_2$; $p(x > d, t = 0) = \mathbf{p_1}$
$\mathbf{\rho}(x < d, t = 0) = \rho_2$; $\rho(x > d, t = 0) = \mathbf{\rho_1}$
$\mathbf{e}(x < d, t = 0) = e_2$; $e(x > d, t = 0) = \mathbf{e_1}$

where d is the location of the diaphragm used to separate the driver from the driven section. The simulation is normalized by, $\mathbf{p_1 = 1}$, $\mathbf{\rho_1 = 1}$, $\mathbf{e_1 = 2.5}$.

4.2.3. Boundary Conditions

The TVD scheme can be used to either create shock waves that will reflect at a solid or porous end wall, as was mentioned earlier, thus allowing the flow adjustment of the induced flow behind the shock wave or reflect at an open end wall to produce an expansion fan, which is the aim of our experiments. The boundary condition allowing expansion wave creation at the open end can thus be described as:

a. Left side is solid wall, so velocity changes its direction here.

b. Right side is the free surface, so velocity is continuous here.

In addition, the type of boundary conditions can also remove the expansion wave influence on the calculation; this is referred as an "incident shock wave' calculation.

4.2.4. Formulation of the TVD Scheme

$$\overline{\omega}_j^n = \omega_j^n - \lambda(\overline{f}_{j+\frac{1}{2}} - \overline{f}_{j-\frac{1}{2}})$$

$$\omega_j^{n+1} = \overline{\omega}_j^n$$

where

$$\overline{f}_{j+\frac{1}{2}} = \frac{1}{2}(f_j + f_{j+1} + \frac{1}{\lambda}\sum_{k=1}^{3} R^k_{j+\frac{1}{2}} \beta^k_{j+\frac{1}{2}})$$

$$\beta^k_{j+\frac{1}{2}} = g^k_j + g^k_{j+1} - Q(v^k_{j+\frac{1}{2}} + \gamma^k_{j+\frac{1}{2}})\alpha^k_{j+\frac{1}{2}}$$

$$\gamma^k_{j+\frac{1}{2}} = \begin{cases} \dfrac{g^k_{j+1} - g^k_j}{\alpha^k_{j+\frac{1}{2}}} & \alpha^k_{j+1} = 0 \\ 0 & \alpha^k_{j+1} = 0 \end{cases}$$

$$g_j^k = S^k_{j+\frac{1}{2}} \cdot \max[0, \min(\left|\tilde{g}^k_{j+\frac{1}{2}}\right|, \tilde{g}^k_{j+\frac{1}{2}} \cdot S^k_{j+\frac{1}{2}})]$$

$$S^k_{j+\frac{1}{2}} = sign(\tilde{g}^k_{j+\frac{1}{2}})$$

$$\tilde{g}^k_{j+\frac{1}{2}} = \frac{1}{2}[Q(v^k_{j+\frac{1}{2}}) - (v^k_{j+\frac{1}{2}})^2] \cdot \alpha^k_{j+\frac{1}{2}}$$

$$v^k_{j+\frac{1}{2}} = \lambda \alpha^k_{j+\frac{1}{2}}$$

where $\lambda = \frac{\Delta t}{\Delta x}$.

Q(x) is called entropy-forced function, which is used to give out physical solutions at any time.

$$Q(x) = \begin{cases} \frac{1}{2}(\frac{x^2}{\varepsilon} + \varepsilon) & |x| \le \varepsilon \\ |x| & |x| > \varepsilon \end{cases}$$

where $0.05 \le \varepsilon \le 0.5$.

The term α is determined by the following linear equation group,

$$\Delta_{j+\frac{1}{2}} \omega = \omega_{j+1} - \omega_j = \sum_{k=1}^{3} \alpha^k_{j+\frac{1}{2}} \cdot R^k_{j+\frac{1}{2}}$$

$$\begin{bmatrix} \alpha^1_{j+\frac{1}{2}} \\ \alpha^2_{j+\frac{1}{2}} \\ \alpha^3_{j+\frac{1}{2}} \end{bmatrix} = \begin{bmatrix} \frac{\varphi_{j+\frac{1}{2}} - \psi_{j+\frac{1}{2}}}{2} \\ \Delta_{j+\frac{1}{2}} \rho - \varphi_{j+\frac{1}{2}} \\ \frac{\varphi_{j+\frac{1}{2}} + \psi_{j+\frac{1}{2}}}{2} \end{bmatrix}$$

$$\varphi_{j+\frac{1}{2}} = \frac{\gamma - 1}{c^2_{j+\frac{1}{2}}}[\Delta_{j+\frac{1}{2}} e + \frac{u^2_{j+\frac{1}{2}}}{2} \Delta_{j+\frac{1}{2}} \rho - u_{j+\frac{1}{2}} \Delta_{j+\frac{1}{2}} m]$$

$$\psi_{j+\frac{1}{2}} = \frac{1}{c^2_{j+\frac{1}{2}}}[\Delta_{j+\frac{1}{2}} m - u_{j+\frac{1}{2}} \Delta_{j+\frac{1}{2}} \rho$$

Letting $A(\omega) = \frac{\partial f(\omega)}{\partial \omega}$ and the characteristic values be

$$(\alpha^1, \alpha^2, \alpha^3)=(u-c, u, u+c)$$

and the characteristic vector is:

$$CR = \begin{bmatrix} 1 & 1 & 1 \\ u-c & u & u+c \\ H-uc & \frac{1}{2}u^2 & H+uc \end{bmatrix}$$

where $H = \frac{\gamma p}{(\gamma-1)\rho} + \frac{1}{2}u^2$.

Averaging by Roe format to get the values for the middle points and letting

$$D = \sqrt{\rho_{j+1}/\rho_j},$$

$$u_{j+\frac{1}{2}} = \frac{Du_{j+1} + u_j}{D+1}$$

$$H_{j+\frac{1}{2}} = \frac{DH_{j+1} + H_j}{D+1}$$

$$c^2_{j+\frac{1}{2}} = (\gamma-1)(H_{j+\frac{1}{2}} - \frac{1}{2}u^2_{j+\frac{1}{2}})$$

Since the shock tube has a variable areas section right after the diaphragm position [refer to shock tube description] ω_j^{n+1} has to be changed to a value with period of Δt after the above calculations are performed.

4.2.5. Calculation procedure

1. calculate Δt and $\lambda = \frac{\Delta t}{\Delta x}$
2. average by Roe
3. solve the characteristic values of matrix A and also vector CR
4. calculate α
5. calculate $f_{j\pm\frac{1}{2}}$
6. calculate ω_j^{n+1}

4.2.6. Non-Dimensional Parameters

The results are provided in a non dimensionalized format given by the following groups:

$$\bar{x} = \frac{x}{L},$$

$$\bar{t} = \frac{t}{t_0}$$

$$\bar{\rho} = \frac{\rho}{\rho_1},$$

$$\bar{p} = \frac{p}{p_1},$$

$$\bar{u} = \frac{\sqrt{\gamma} u}{a_1},$$

where L is the total length of the shock tube and $t_0 = \frac{\sqrt{\gamma} L}{a_1}$.

4.3. Output Files with the TVD [Incident Shock Mode]

A typical output of the TVD program provides the following Variables:

a. Velocity

b. Pressure

c. Density

d. Static Temperature

e. Mach Number

f. Total Temperature

g. Mass flux [ρu]

Figure 4.2 shows a typical result plot of the incident shock wave version, where the pressure ratio, density ratio and flow velocity behind the shock wave [P_2,ρ_2 and U_2] are used as input parameters. The y-axis of this graph indicates ratios with respect to the

conditions downstream of the shock rather than absolute values. For example, the pressure line starts with a value of 1.0 and jumps to the value of 1.62 after the shock wave passed by that point of interest, which in this case is the starting point of the working section indicating a value of $P_2 = 23.82$ psig. The effect of the expansion waves reflected from the open end is visibly noticed in all parameters, i.e. the pressure plot shows that the expansion starts at 0.60 seconds after the bursting of the diaphragm. The expansion wave effect from the driver section is not observed here since the conditions of the incident shock were used as input parameters.

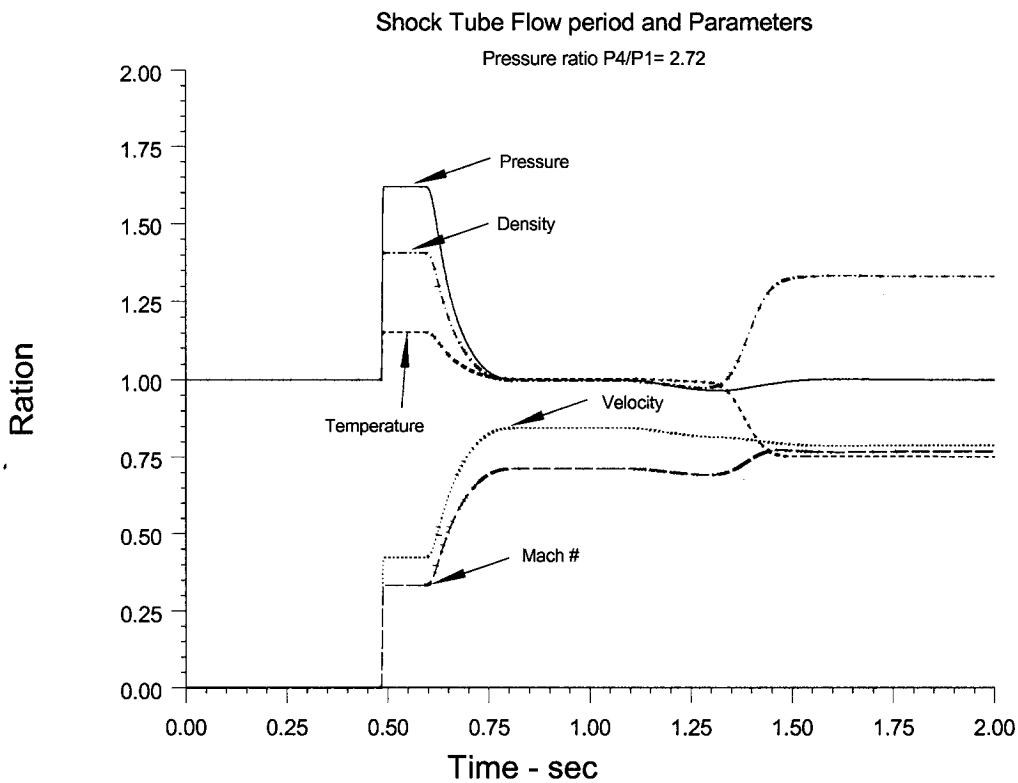

Figure 4.2: Shock tube Flow Parameters / Incident Case P41 = 2.72.

4.4. Output Files with the TVD [Regular - Driver Section Mode]

During the shock tube experiments, the expansion waves from the driver side could not be eliminated, thus the true pressure and density ratios in the driver section

ought to be used as the boundary conditions if one would attempt to evaluate the correct length of the shock tube, including the working section, that would maximize the useful flow. Figure 4.3 provides all the information at a point 10 inches downstream of the grid with a driver pressure $P_4 = 35$ psi.

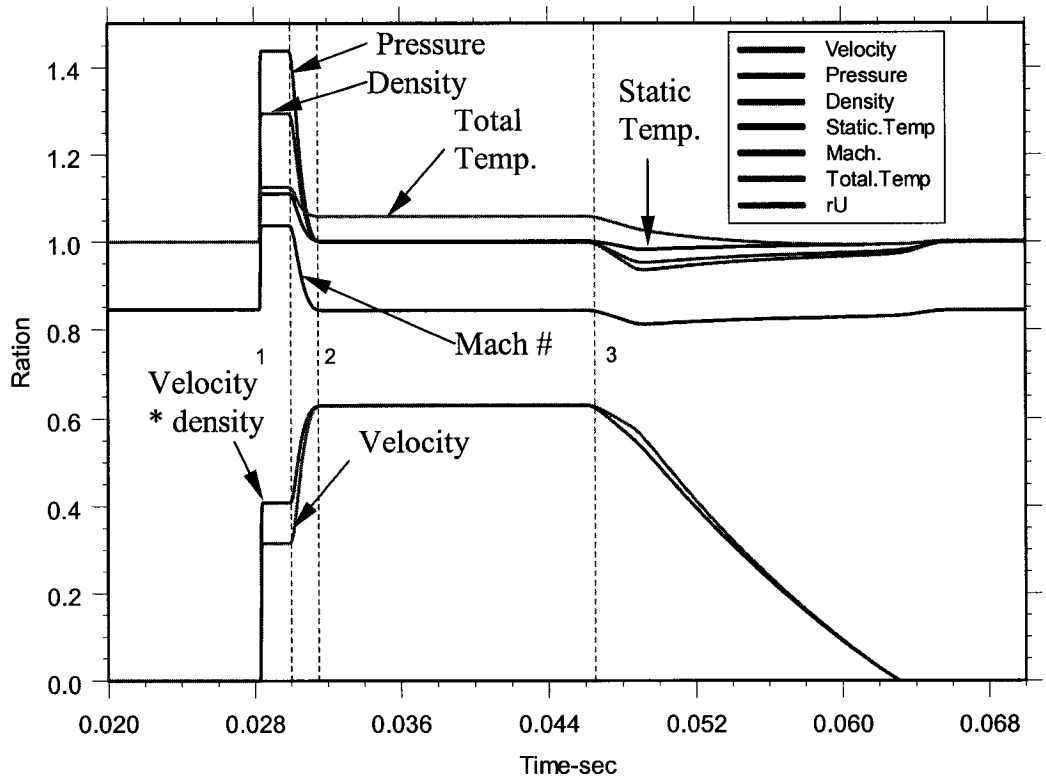

Figure 4.3: Shock tube Flow Parameters [EW included] - P4 = 35 psi.

The effect on the pressure and velocity due to the expansion waves from the driver section are now evident. The arrival of the front of the expansion fan from the open end is indicated at point 1. At point 2, the expansion wave drops the pressure to that of atmospheric, basically indicating the end of the expansion fan. Location 3 points out the arrival of the expansion waves from the driver section, the time at which the useful flow is over. Plots like the ones in Figure 4.3 provide information only at a specific point, which is usually the exception rather than the rule. If the history of all these variables along the working section is needed, which it is in the case of the 2 component of

velocity measurements with X wires as will be discussed later, it is necessary to monitor the output of all these variables at different locations. Figure 4.4 provides a typical plot of such an analysis with the pressure history for 10 locations; one at the triggering location, one at the grid location, seven locations spaced 2 inches apart starting at 6 inches downstream the grid, and one at the open end of the working section 24 inches from the grid.

4.5. Expansion – Interaction Region

The TVD scheme tool was utilized to find the correct placement of the instrumentation used in the working section for all the experiments since maximizing the flow would not be of any interest if the correct timing of interaction was not known. As mentioned before, two working sections were used, a long one of a total length of 8ft and a shorter

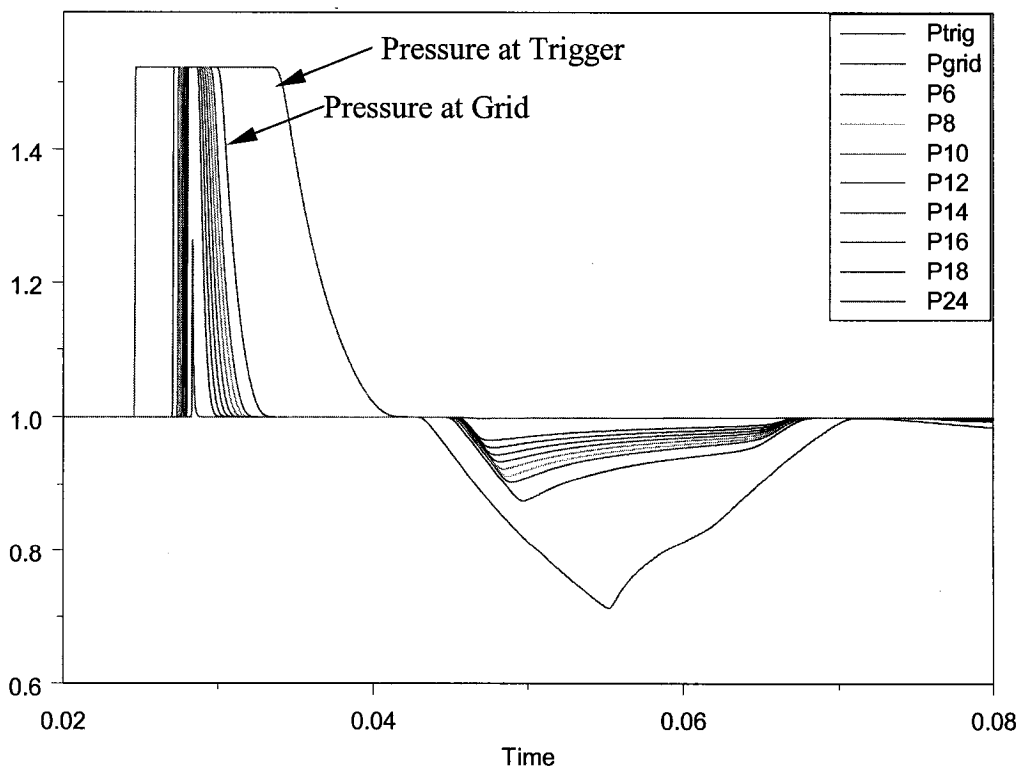

Figure 4.4: Pressure history of transducers along working section
[P_4 = 35 psig, U_2 = 107 m/s , W_s = 415 m/s].

one of a total length of 2ft. Figure 4.5 shows the pressure contours against time and location along the 8ft working section for a specific pressure ratio in the driver section.

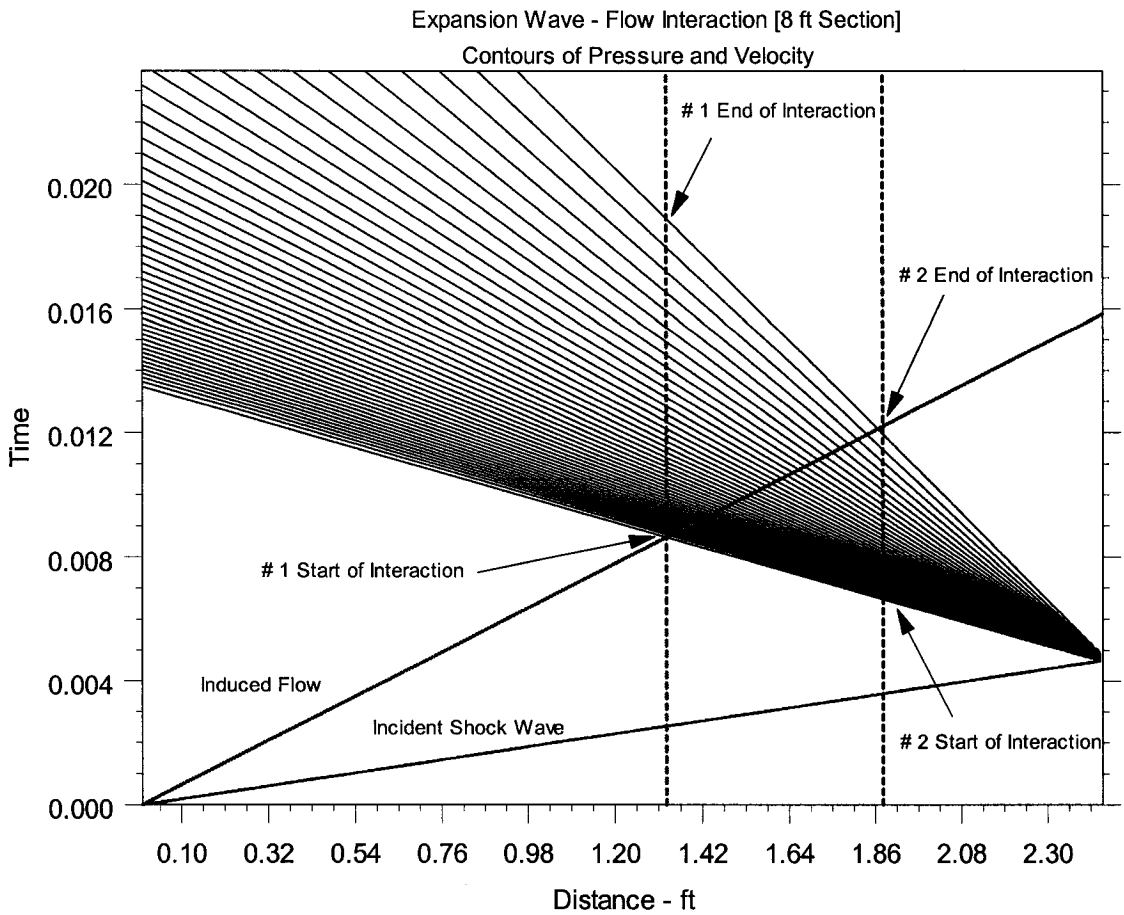

Figure 4.5: Expansion Wave – Flow Interaction / Pressure Contours [8ft].

This longer version allows for a longer maximum interaction time [about 10ms shown below] for location # 1 yet the onset of the interaction with the turbulent flow from the grid [about 10ms as shown below] is too long which eventually reduces significantly the useful data duration. The shockwave-induced velocity is also shown here since it is a requirement for the location of the start of the interaction. Figure 4.6 shows the pressure contours against time and location along the 2ft working section. The shorter version indicates the onset of the interaction at about 2ms after the grid and a maximum

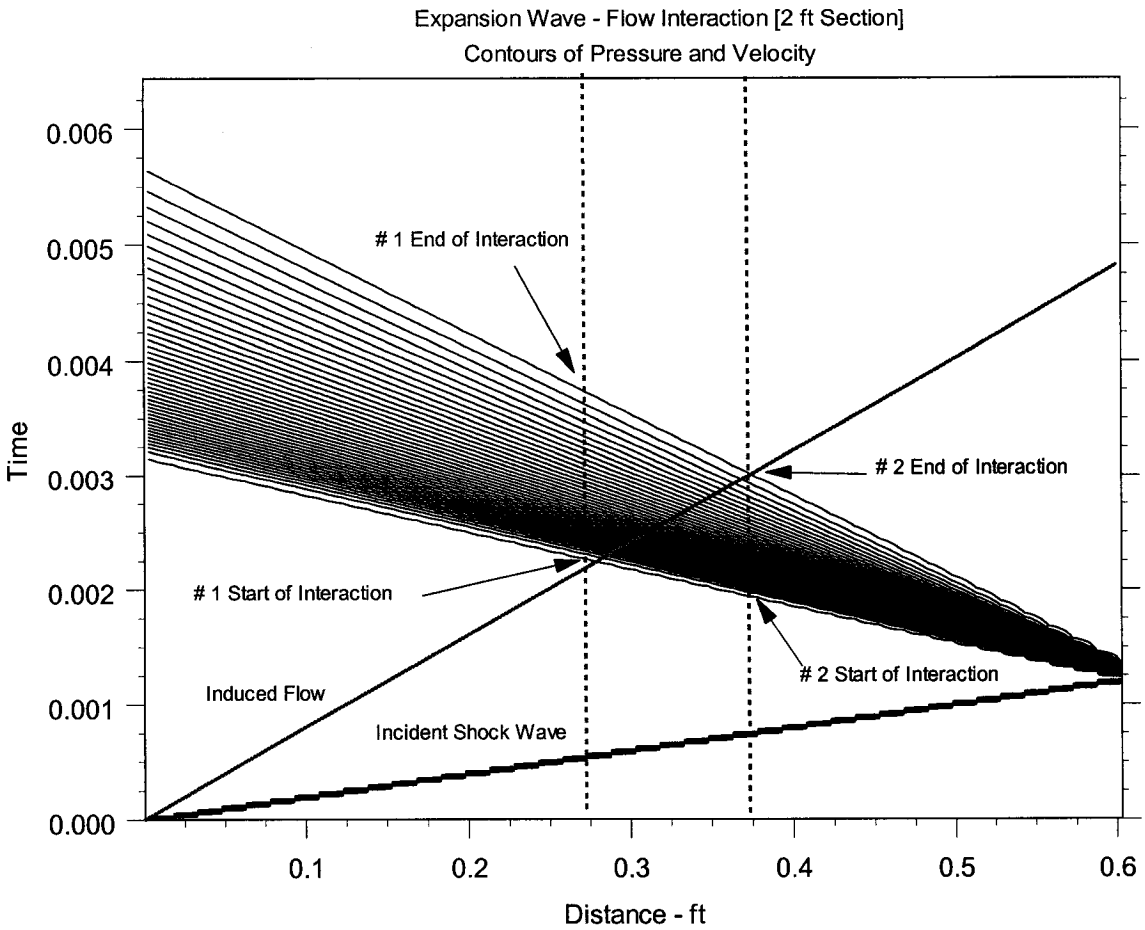

Figure 4.6: Expansion Wave – Flow Interaction / Pressure Contours [2ft].

interaction time of about 1.5ms, which allows eventually a longer duration of useful flow prior to the arrival of the expansion waves from the driver section. Figure 4.7 and 4.8 demonstrate the pressure contours and density contours of a typical experiment along the 12in diameter shock tube with the 2ft working section attached to it. All regions are clearly labeled, especially the useful data duration, which is of vital importance for the uncontaminated data processing. In general, it is clear that the induced flow is separated by three distinct regions; passing through the grid becoming thus almost homogeneously and isotropically turbulent, followed by the transient interaction with the expansion wave [non-stationary region] and after that, decaying in the region after the interaction.

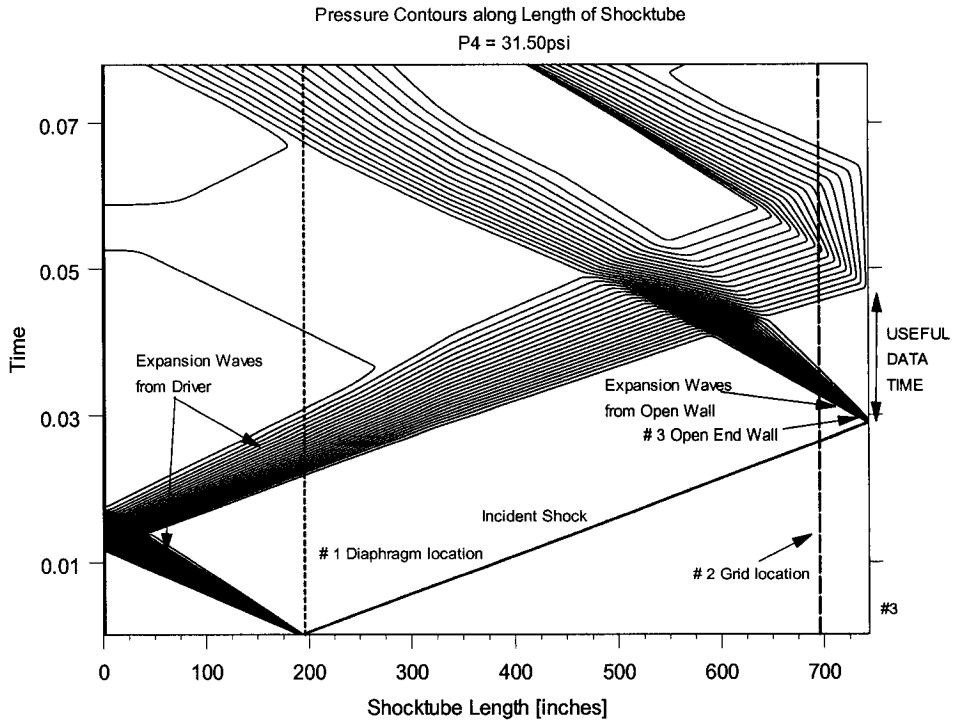

Figure 4.7: Pressure Contours along 2ft length of Shock tube.

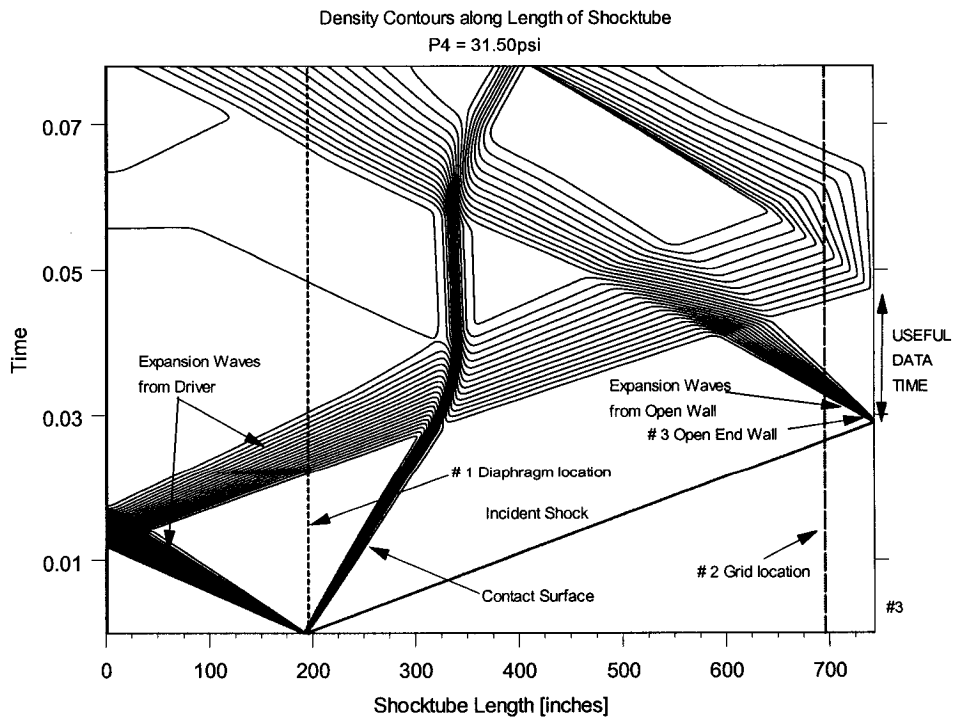

Figure 4.8: Density Contours along 2ft length of Shock tube.

The later is a region of interest. One of the controlling parameters for that interval is the initial bursting pressure in the driver section [P_4]. On that account, the TVD program was utilized to simulate different ranges of pressure to optimize for the one that gives the longest flat region after the expansion has passed. Figures 4.9a-d show four pressure contour plots with different initial bursting pressures:

- $P4_a = 35$ psig
- $P4_b = 45$ psig
- $P4_c = 55$ psig
- $P4_d = 65$ psig

As specified in Figure 4.9a the useful duration of data is approximately enclosed in the circle by the region unaffected by the expansion wave from the driver section. It is clear that the best choice is $P4_a = 35$ psig, a value that was used for most of the experiments.

Higher bursting pressures were used in the cases that only the transient part of the interaction was of interest. This lower pressure value choice reduces the strength of the reflected shock off the grid that travels in the upstream direction as described in Figure 2.14 and Figure 2.15. This is an outcome that favors the experimental sets. In addition, the pressure drop across the grid is kept as low as possible which allows the shock wave to reform and recover its shape after its passage through the grid within a few mesh sizes length.

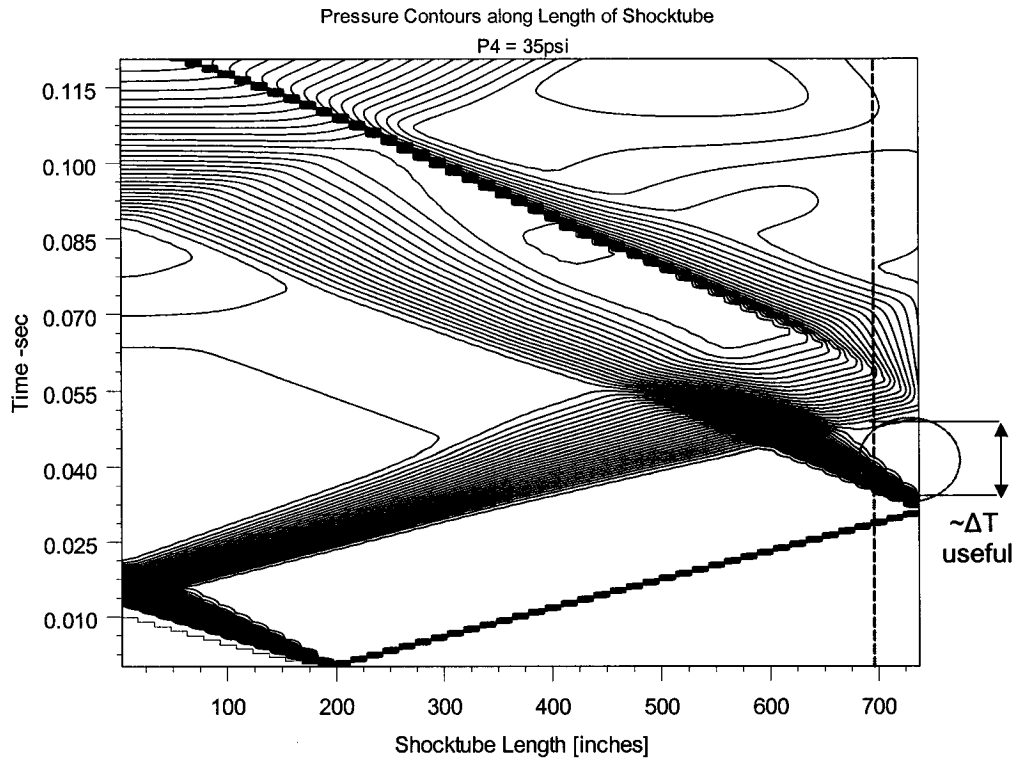

Figure 4.9a: Pressure Contours along 2ft length of Shock tube [P4 = 35 psig].

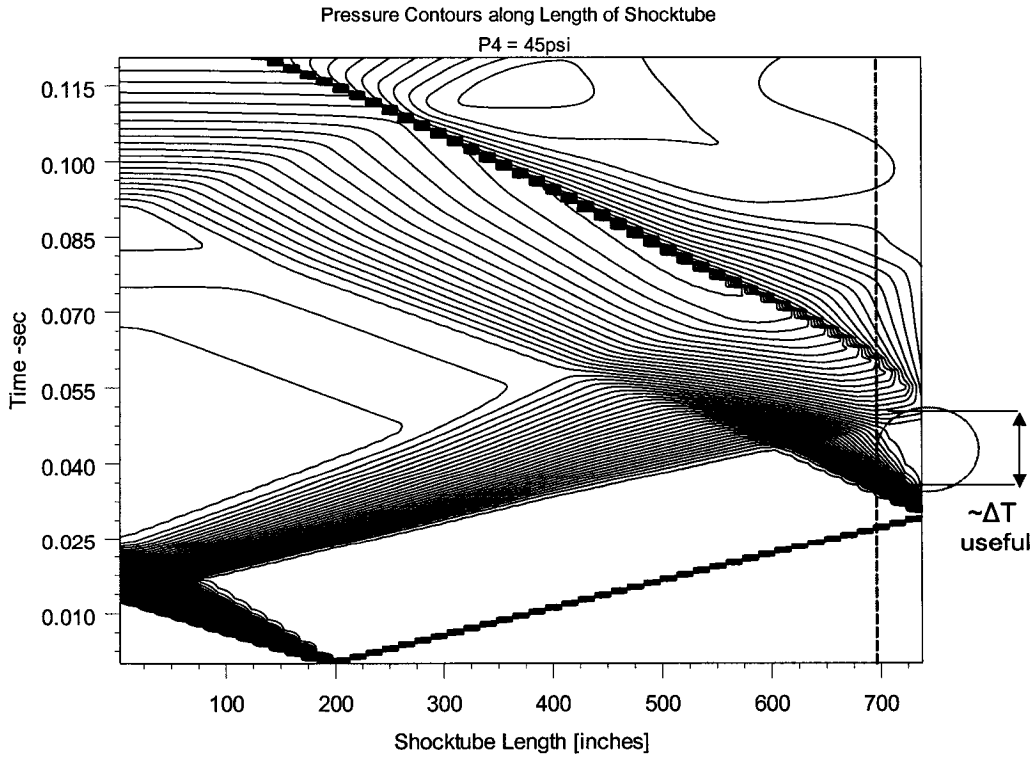

Figure 4.9b: Pressure Contours along 2ft length of Shock tube [P4 = 45 psig].

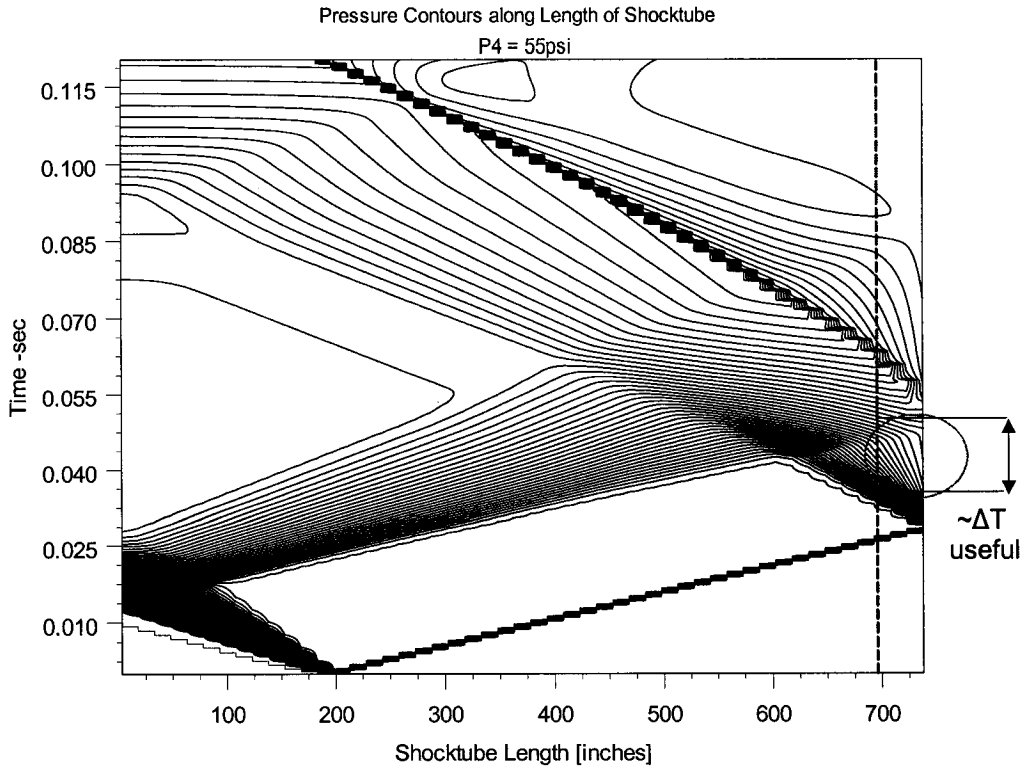

Figure 4.9c: Pressure Contours along 2ft length of Shock tube [P4 = 55 psig].

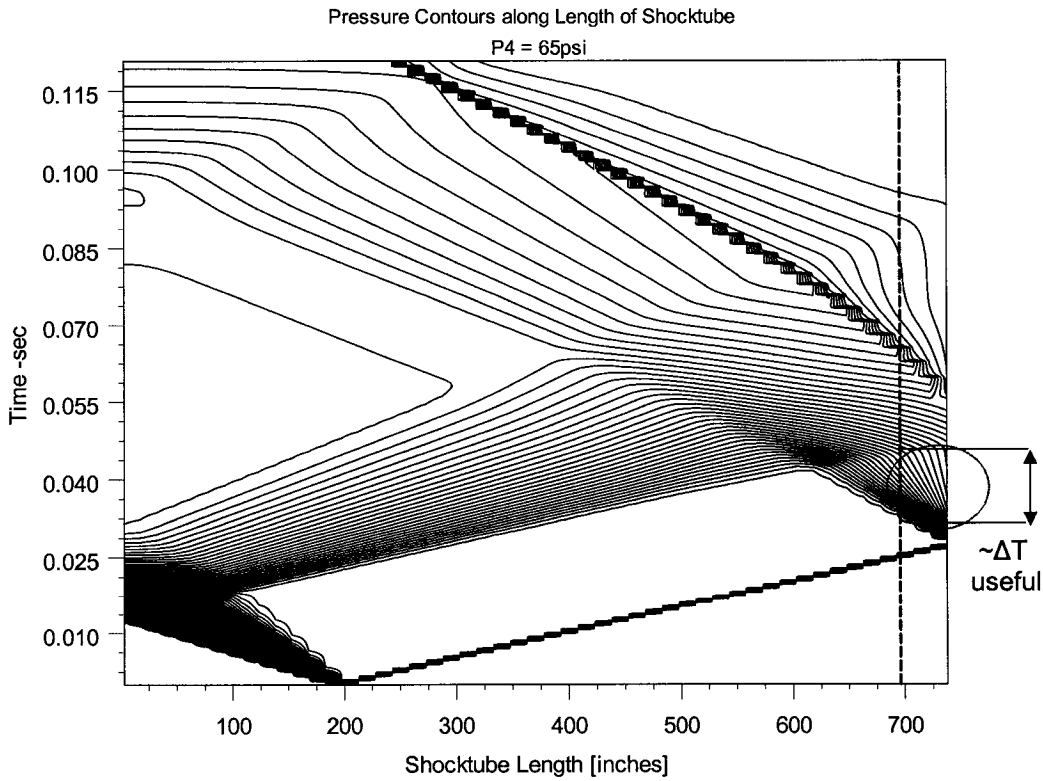

Figure 4.9d: Pressure Contours along 2ft length of Shock tube [P4 = 65 psig].

Chapter 5: Experimental Set Up

5.1. Experimental Setup Introduction

In this chapter some of the experimental set up will be re-introduced or described in more detail in order to allow the reader to follow the experimental steps that were performed primarily for the X wire measurements. The vorticity probe will be introduced as a whole in chapter 7.

The induced flow behind the traveling shock wave passes through a turbulence-generating grid installed in the beginning of the working section of the facility. The velocity of the induced flow behind the shock wave depends on the rupture pressure of the diaphragm, i.e. driver strength P_4. The initial step after verifying the correct value for P_4, which in our case was chosen to be around 21.00psig was to correctly choose the appropriate instruments for obtaining the quantities involved in turbulent flows. To simultaneously resolve two dimensional velocity components with hot wires, a cross wire (X-wire at 45°) arrangement was used. New three-wire probes were designed and custom built. Six different three-wire probe assemblies were concurrently used at different downstream locations, all adjustable to different lengths, each carrying 2 hot-wires in an X configuration and one cold-wire for simultaneous velocity and temperature measurements respectively. The three-wire probes were equipped with 5 μm Platinum/Tungsten wires for velocity measurements and with a 2.5 μm Platinum/Tungsten wire for temperature measurements. To eliminate any wake effects from probes located upstream, all of the probes were staggered at increasing distances from the tube wall. The probes we also varied in the radial direction in increments of 22.5 degrees (see figure 5.3). The cross wires as well as the vorticity probe, were driven by

DANTEC anemometers model CTA56C01 and the temperature wires were connected to EG&G model 113 low noise, battery operated pre-amplifiers/filters. The output signal of the cold-wire was digitally compensated for thermal lag up to frequencies of interest.

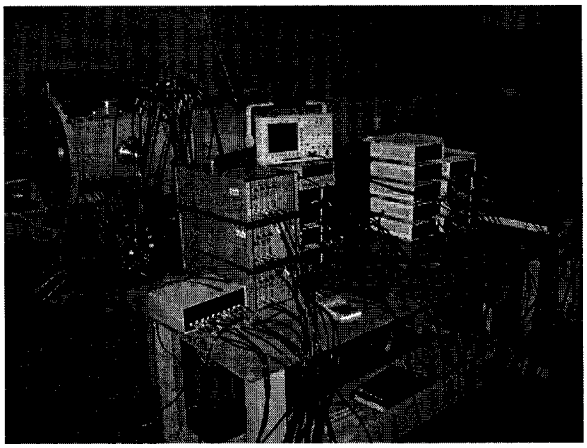

Figure 5.1: Instrumentation for experiments

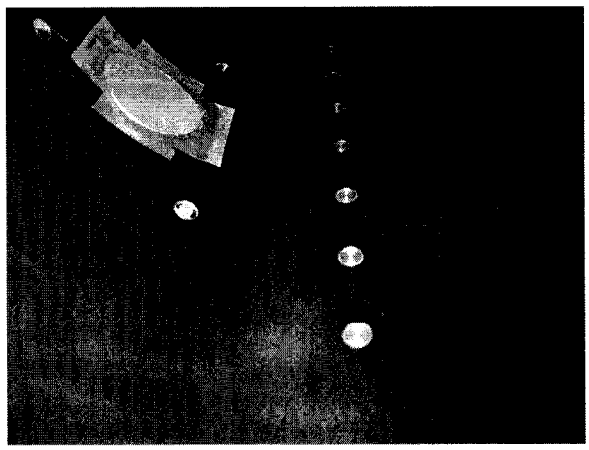

Figure 5.2: Pressure Taps along the length

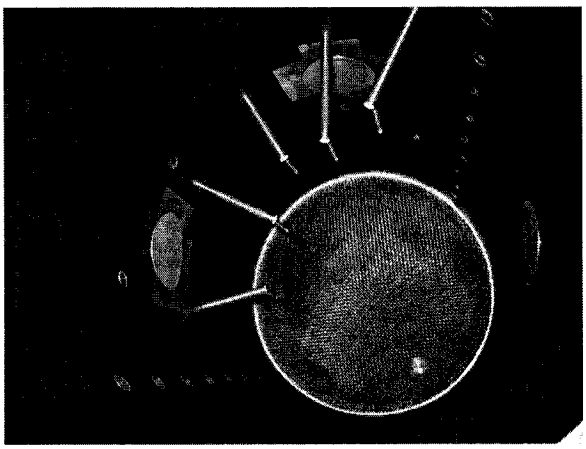

Figure 5.3: X wire Probes along working section

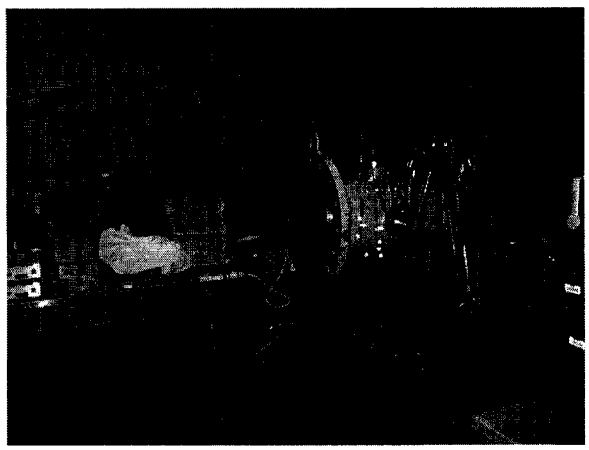

Figure 5.4: Open end condition for Shock Tube

For more details on the hot-wire techniques applicable to shock tubes see Briassulis et al.[3] where estimates of uncertainties in the measurements are also given. Figures 5.1 – 5.4 provide images of the location of the arrays as described above along with the instrumentation of the setup.

Figures 5.5 and 5.6 show a close up view of the one of the x wire probes utilized.

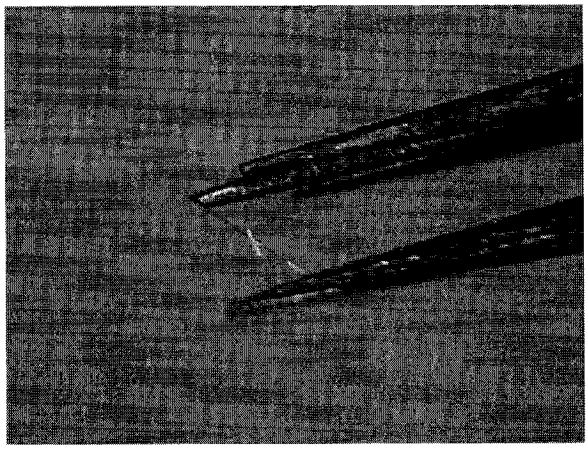

Figure 5.5: Close up of X wires

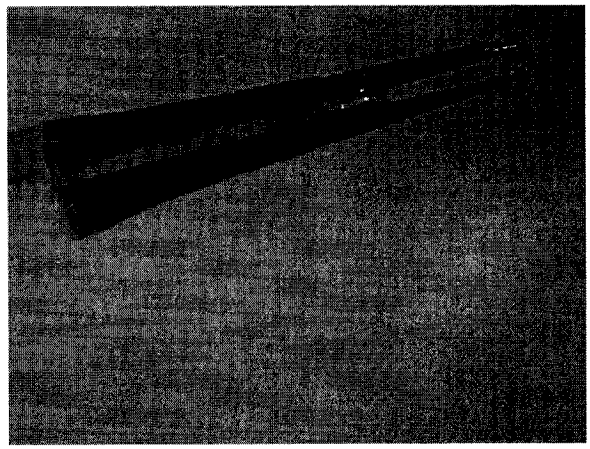

Figure 5.6: Close up of X wire probe tip

#	Grid Size	Solidity	X/M				P_2 - psig	M_2	W_s - m/s
			10in	12in	14in	15.25in			
1	2x2a	0.39	20	24	28	30.5	4.55	0.1892	388.60
2	3x3	0.28	30	36	42	45.75	4.20	0.1759	385.25
3	4x4	0.39	40	50	56	61	4.44	0.1853	388
4	5x5	0.44	50	60	70	76.25	4.68	0.1956	390
5	8x8	0.37	80	96	112	122	5.76	0.2313	400

Table 5.1: Experimental characteristics using X wire probes.

Table 5.1 provides some of the characteristics of the experiments performed with the X wire assemblies. The CCA anemometer will be introduced in the vorticity probe discussion, yet the most relevant settings that need to be mentioned are:

Constant Current output driving the cold wires [CCA mode] at 6V power supply: [0.6mA] with the ability to vary the value from 0.5mA to 1.0 mA.

Typical value for a cold wire resistance [10 Ohm],

Typical value of the BNC cable connecting the hot wires to the AD = 1.20 Ohm,

The Kulite pressure transducers flash mounted on the wall were driven by a constant voltage power supply at 9V.

X- Wires are 45 degree type.

Chapter 6: X-Wire Results

6.1. Results of the Interaction Region

This chapter will provide typical results of the first set of experiments of expansion wave interaction with turbulence having in mind that the understanding of the interaction is of vital importance. In order to do that, some the pressure signals were low-pass filtered and then the time-derivative was obtained. A typical result of this signal processing is shown in Figure 6.1

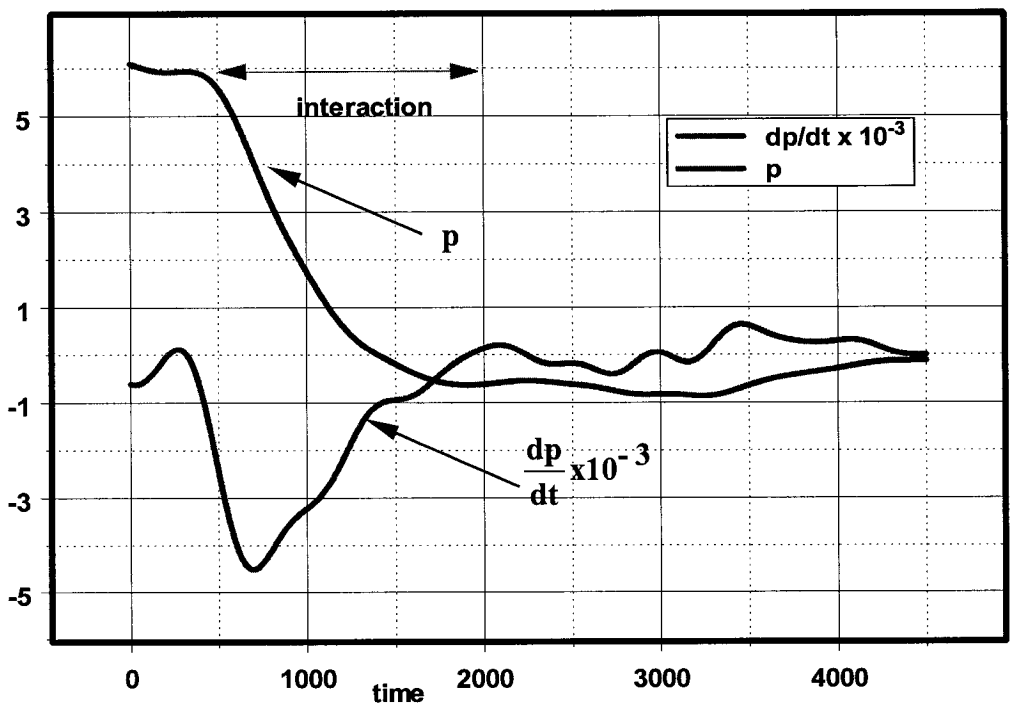

Figure 6.1: Low-pass filtered pressure signal and its time-derivative.

The time derivative if divided by a typical propagation velocity C-U, can be converted to pressure gradient, which is the dominant term in the transport equation. The results show that the pressure gradient peaks very close to the beginning of the interaction region, i.e.

within 15 percent of its total duration. Then it starts to relax some of its strength and reaches values close to zero at the end the duration of the interaction.

The signals of velocity pressure and temperature are characterized by a gradual change through the interaction in addition to the presence of turbulence fluctuations. Most of the turbulent fluctuations occur at frequencies higher than the low frequency scales of the gradually changing values inside the interaction region. In order to remove this "trend" the signals were high-pass filtered at about 500 Hz the results are shown in Figure 6.2.

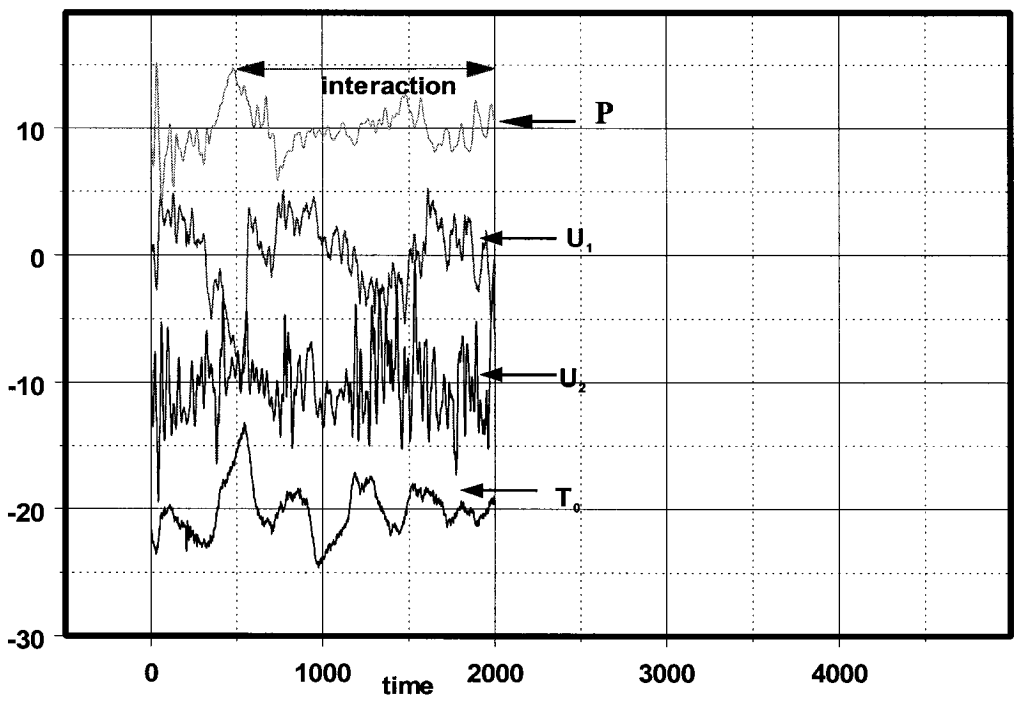

Figure 6.2: High-pass filtered signals of pressure velocity components and total temperature. Signals are displaced for better visual-aid and amplified.

All signals have now a zero mean value. In order to demonstrate the amplitude of the fluctuations within this interaction, the region was subdivided into ten shorter regions and the r.m.s of the fluctuations was computed within each of these sub-regions. This information within each of the zone is not an accurate value of the true r.m.s because the process is not stationary. It represents, however, a reasonably good estimate of the amplitude of the fluctuations within each sub-region. These r.m.s values $<\sigma_i>$ are normalized by the true r.m.s. value in the upstream region σ_u and are plotted in Figure 6.3. Thus, the ratio $<\sigma_i>/\ \sigma_u$ indicates the attenuation of the fluctuations within the interaction. The data show that fluctuations are attenuated immediately after the start of the interaction and reach the maximum attenuation approximately at the time the pressure gradient reaches its peak value. Then they start to increase and approach the values obtained in the downstream of the interaction region.

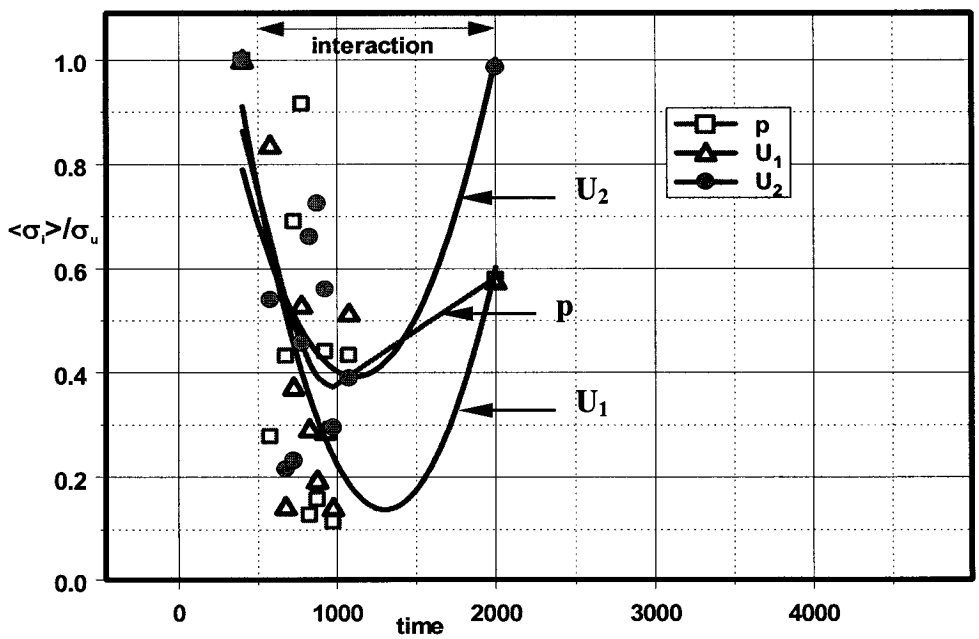

Figure 6.3: Attenuation of turbulent fluctuations inside the interaction region.

6.2. Turbulence modification through the interaction

Attenuation of turbulence is one of the major features of expansion waves-turbulence interaction. Linear analysis is expected to predict attenuation of turbulence as long as fluctuations of pressure, velocity and temperature upstream of the expansion waves are small so that the front is not substantially distorted and the Rankine-Hugoniot conditions can be linearized. DNS data or other CFD results are not available at this time.

Typically the attenuation of turbulent fluctuations should depend on the expansion waves strength, the state of turbulence of the incoming flow before the interaction, and its level of compressibility.

Figure 6.4 and 6.5 show the amplification ratio of the velocity vector fluctuations defined as the ratio of the standard deviation of the fluctuations downstream of the interaction σ_d to that upstream of the interaction σ_u i.e. $G = \sigma_d/\sigma_u$. Data available from the two velocity components of various experiments obtained by x-wires and the wall pressure are plotted against the normalized distance from the rid, x/M, where is the mesh size.

The data of the 8x8 case, which are shown in Figure 6.4, express the attenuation of longitudinal velocity fluctuations at all locations downstream of the grid. Close to the grid, fluctuations of the lateral velocity component and pressure are amplified by the interaction. However at further distances from the grid these fluctuations are attenuated.

It appears that the ratio $G = \sigma_d/\sigma_u$ decreases with x/M.

Attenuation of longitudinal fluctuations through the whole flow field have been also observed in the case of the 4x4 grid (see Figure 6.5). Lateral velocity fluctuations are attenuated close to the grid and amplified further downstream. The data obtained with the

vorticity probe seem to fit this pattern. Pressure fluctuations seem to be amplified close to the grid and attenuated away from it.

The attenuation data presented here have been obtained in incoming flows, which are practically incompressible since the Mach number is about 0.3. The passage of the expansion waves however accelerates the flow to Mach numbers about 0.8. Thus during the interaction compressibility effects start to play a significant role, and therefore it is expected to affected the flow development.

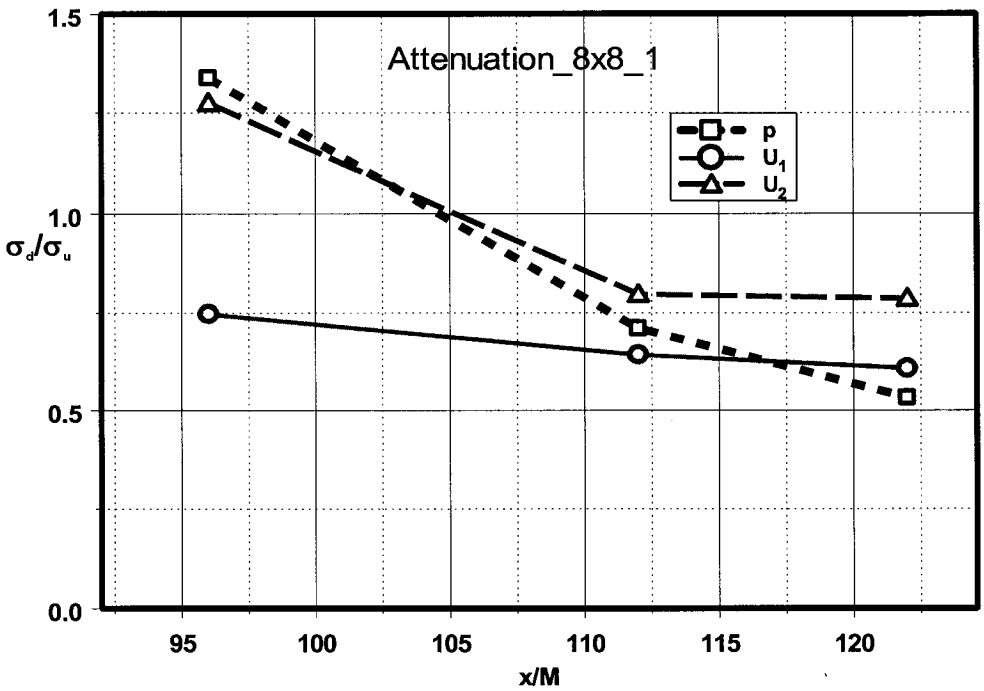

Figure 6.4: Attenuation of turbulent fluctuations in the case of the 8x8 grid.

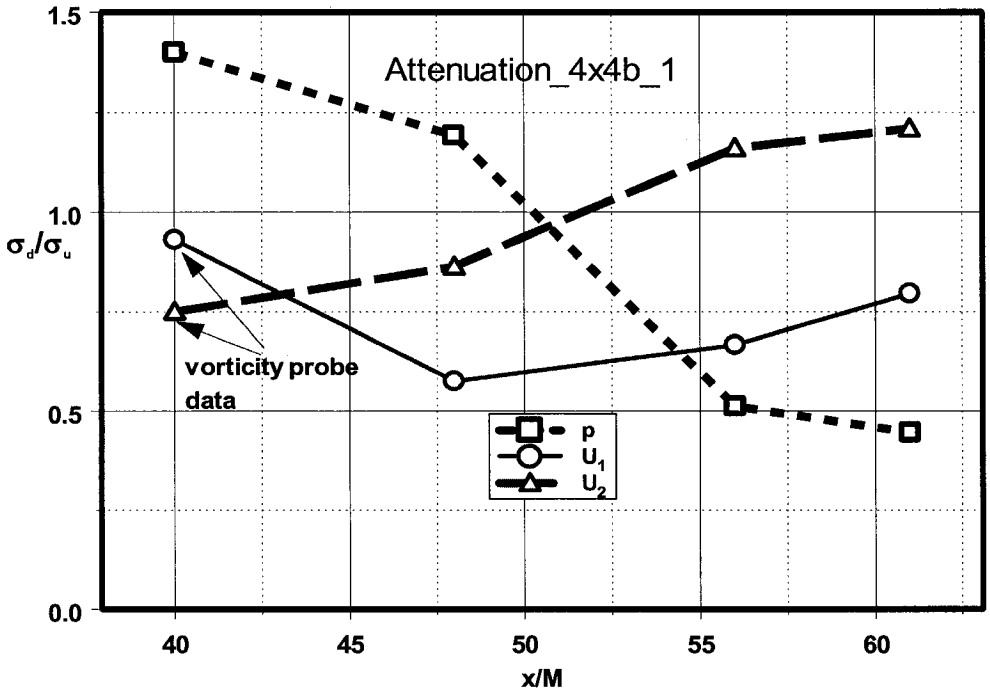

Figure 6.5: Attenuation of turbulent fluctuations in the case of the 4x4 grid.

Chapter 7: Vorticity Background

7.1. Introduction to Vorticity

Fluid particles in motion deform, and therefore, can conform to complex geometries and shapes. Deformation represents the different ways in which particles can change shape, and/or position under the influence of external forces. Formally the modes of deformation are defined either as:

1. Simple translation
2. Simple rotation
3. Strain
    a. Extensional strain
    b. Shear strain

The Vorticity vector in Cartesian coordinates is defined by its three components,

$$\omega_x = \frac{\partial w}{\partial y} - \frac{\partial v}{\partial z} \qquad \omega_y = \frac{\partial u}{\partial z} - \frac{\partial w}{\partial x} \qquad \omega_z = \frac{\partial v}{\partial x} - \frac{\partial u}{\partial y} \tag{7.1.1}$$

and measurements of vorticity therefore can be performed by directly measuring velocity gradients at two distinct, but nearby, points. The validity of approximating velocity gradients relies on neglecting second order and higher terms from a Taylor expansion of velocity. For instance, the velocity gradient of u in the z-direction is obtained by the following Taylor expansion:

$$u(x_0, z_0 + h) = u(x_0, z_0) + h\frac{\partial u}{\partial z}(x_0, z_0) + h^2 \frac{\partial^2 u}{\partial z^2}(x_0, z_0) + h^3 \frac{\partial^3 u}{\partial z^3}(x_0, z_0) + \ldots\ldots \tag{7.1.2}$$

By neglecting the higher terms, including the second one, the velocity gradient is then approximated by:

$$\frac{u(x_0, z_0 + h) - u(x_0, z_0)}{h} \cong \frac{\partial u}{\partial z}(x_0, z_0) \tag{7.1.3}$$

Some other issues are mentioned here as they relate to the accuracy of the measurements of velocity, and consequently, vorticity. The first being accuracy of single point velocity measurements which is limited by hardware and design uncertainties as well as uncertainty in the calibration of the non-linear curves. Taking the difference of two velocities, which are very close in value, can possibly compound the error involved from that of a single realization by bringing into play the sampling resolution. If care has been taken to maintain a high signal-to-noise ratio and high-resolution analog to digital [A/D] conversion is utilized, errors like this can be minimized. By the same token, better accuracy can be attained if the separation distance, h, is accurately known or measured. The most serious problems concerning closely spaced intrusive probes are the aerodynamic and thermal interference these probes produce on one another and their spatial resolution. This is typical of hot-wire probes in which up to twelve individual hot-wire probes have been recently implemented for three-dimensional vorticity measurements (see e.g. Tsinober, Kit, and Dracos[30]).

7.2. The Vorticity Probe

A new multi hot-wire probe has been developed which is capable of measuring velocity-gradient related quantities in non-isothermal flows or in compressible flows. The present probe has been build upon the experience gained with vorticity measurements in incompressible flows (see Honkan and Andreopoulos[31]) by using a probe with nine wires and with velocity measurements in compressible flows by using single and cross-wire probes (see Briassulis et al.[32]). The present vorticity probe, which consists of 12 wires, is

a modification of the original design by Honkan and Andreopoulos[31]. The three additional wires were operated under the Constant Current Mode (CCA) and used to measure time dependent temperature. The probe essentially consists of a set of three modules [see Figure 7.1d for an individual module or array], each of them being mutually orthogonal to the flow. The rendered isometric view of the probe with the corresponding laboratory coordinate system is shown in Figure 7.1a, Figure 7.1b and 7.1d. It provides the front view of the probe whose overall size is determined by the cenroid to centoid distance between the triple wire sets of 1.73mm (center to center extreme wire position is 2.6mm and extreme prong distance is 3.5mm). Each triple wire set is labeled as A, B and C accordingly. The supporting stem holder is made of 316 SS stainless steel tubing with an outside diameter of 0.375 inches and .040-inch wall thickness machined bent at 90 degrees. This stem construction showed no sign of deformation after many experimental runs. The prongs are made from fine stainless steel rods which have been tapered towards the hot-wire contacts. 30-gauge lead wiring was soldered to the other end of the prongs. All the individual prongs are electrically isolated from each other through several ceramic holders and the whole assembly is glued onto the aluminum tubing. Figure 7.2 shows actual photographs taken by a stereo-microscope and a CCD Camera.

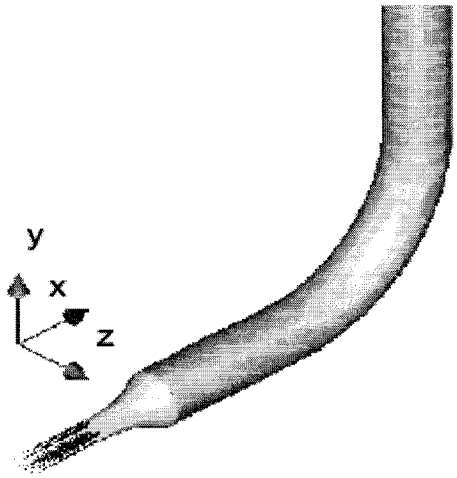

Figure 7.1a: Isometric rendered view of the vorticity probe.

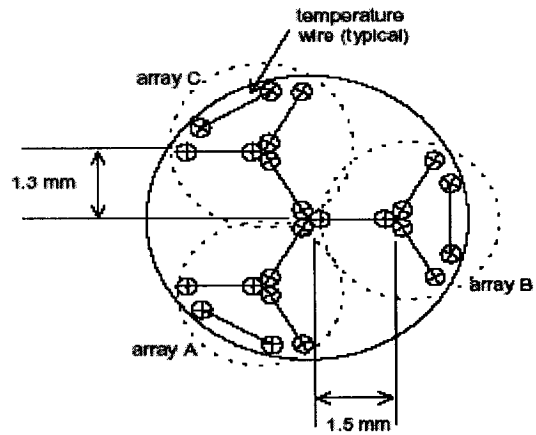

Figure 7.1b: Front view of the vorticity probe.

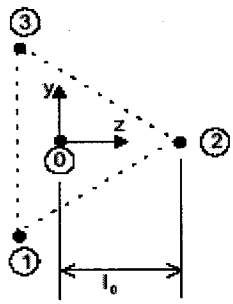

Figure 7.1c: Centroid Locations.

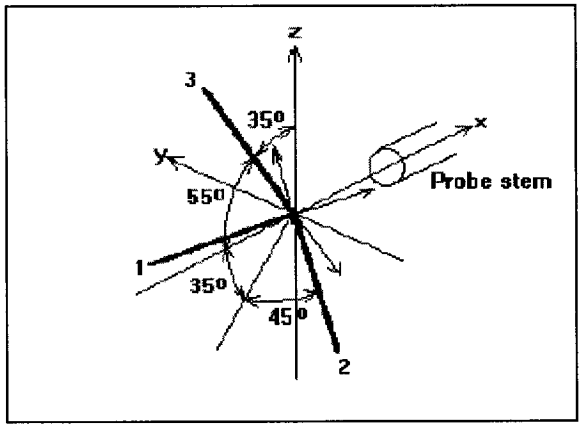

Figure 7.1d: Single module of the Vorticity Probe.

Figure 7.2a: Vorticity Probe Image.

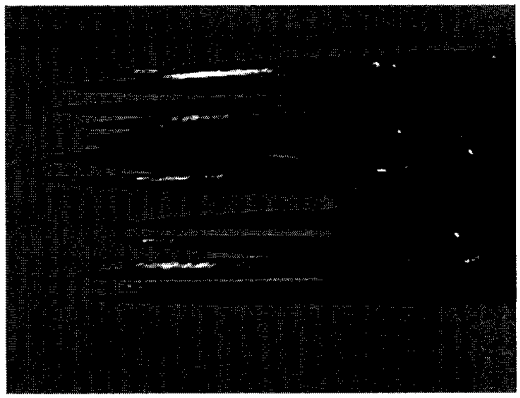

Figure 7.2b: Close up image of the probe.

Each module as seen in Figure 7.1d contains three hot-wires operated in the Constant Temperature Mode (CTM). Each wire of the triple wire sub-module is mutually orthogonal to each other, thus oriented at 54.7 degrees to the probe axis. Each of the 5 μm diameter tungsten sensors is welded on two individual prongs which have been tapered at the tips. Each sensor is operated independently since no common prongs are used. Each of the 2.5 μm diameter cold-wire was located on the outer part of the sub-module as seen in Figure 7.1b.

The hot-wire output voltage E_i of the ith sensor is related to the effective cooling velocity, $U_{i,eff}$ through the well known King's law:

$$E^2 = A + B(\rho U_{eff})^n \qquad (7.2.1)$$

Here the effective mass flux (ρU_{eff}) is the independent calibration variable, which in this form accounts for the effect of compressibility. The most general from of U_{eff} is given by:

$$U_{eff}^2 = U_N^2 + k^2 U_T^2 + h^2 U_B^2 \qquad (7.2.2)$$

where U_N , U_T and U_B are the normal, tangential and bi-normal components of the velocity vector with respect to the local individual wire coordinate system. The weighting

variables k and h are the yaw and pitch coefficients. Andreopoulos[33, 34] describes how the acceptance cone for this probe type is found by applying a condition which is dictated by evaluating the sign of the Jacobian of the raw voltage as a function of the velocity magnitude, and yaw and pitch angles, formed between the probe coordinate system and the lab coordinates system, over a range of these angles. The validity domain or acceptance cone is determined by the range over which the Jacobian does not change sign. It was found that the Jacobian criteria held for virtually the entire range was investigated. The reader is referred to Appendix A where more details on the calibration are inferred.

In selecting the dimensions of the vorticity probe, several conflicting considerations were taken into account. The individual wire length, the size of the individual sub-module and the size of the overall probe should be as a small as possible so that small scales can be resolved adequately since it is known that most of the contributions to vorticity come from small scales of turbulence. However, small wire spacing can lead to thermal interference and cross talk between the wires. This was of particular concern in the present case because of the high overheat ratio used in the experiments. Yaw and pitch tests of the probe were carried out in order to identify any thermal effects on wires located in the heated wake of a neighboring wire located upstream. These tests indicated no thermal interference among the wires. The reason for this behavior is that the spreading rate of the thermal wakes is reduced in high Reynolds number flows.

The requirement to reduce the probe size had to be counterbalanced with the requirement that the spacing between the sub-modules and the individual wires should be

finite so that the velocity gradients, which were used to compute vorticity and strain-rates, do not disappear.

The digitized signals were processed off-line. The cold-wire signals were first converted to total temperature that together with the hot wire signals were used to obtain instantaneous three-dimensional mass fluxes at three neighboring locations within the probe. Mass fluxes were further separated into density and velocity by using the method adopted by Briassulis et al.[23, 24] Decoupling density from mass fluxes assumes that static pressure fluctuations are small. This is the 'weak' version of the original 'strong Reynolds analogy' hypothesis of Morkovin[35]. The original hypothesis is based on the assumption that pressure and total temperature fluctuations are very small. In the present work, total temperature was measured directly and therefore no corresponding assumptions were needed. The pressure, however, was measured at the wall and not at the location of the hot wire measurement. The mean value of this pressure signal was used to separate the density and velocity signals since no mean pressure variation has been detected across a given section of the flow.

In summary, it should be emphasized that the major contribution of the present hot wire techniques is the addition of temperature wires to obtain instantaneous information on total temperature. This allowed decoupling of all partial sensitivities of the probe from each other.

7.3. Computation of Velocity Gradients

In flows where the compressibility effect plays a significant role, i.e. high-speed shock wave induced flows like in our case, the simpler relation between raw voltage and the

velocity vector in subsonic flows, in which density is considered constant, does not hold. The present probe output obtained by applying the calibration procedure of Appendix B yields the three components of mass flux and the total temperature at each of the triple wires. Still, these two flow variables are not sufficient to uniquely determine the velocity vector. Additional data or assumptions need to be made concerning one of the thermodynamic variables, i.e. density, pressure or temperature.

This is discussed in the following section. After properly extracting three velocity components from the data of each of the three sets of triple wires, the velocity data can be used to compute all three vorticity components and the six distinct rates of strain terms.

By following the one component gradient analysis initiated in Section 7.1 and applying a probe coordinate system shown in Figure 7.1c, a Taylor's expansion for each velocity component is obtained as follows:

$$u_{1_1} = u_{1_0} + \left(\frac{\partial u_{1_0}}{\partial x_2}\right)_{x_{1_0}, x_{2_0}, x_{3_0}} \Delta x_{2_1} + \left(\frac{\partial u_{1_0}}{\partial x_3}\right)_{x_{1_0}, x_{2_0}, x_{3_0}} \Delta x_{3_1} \tag{7.3.1}$$

$$u_{1_2} = u_{1_0} + \left(\frac{\partial u_{1_0}}{\partial x_2}\right)_{x_{1_0}, x_{2_0}, x_{3_0}} \Delta x_{2_2} + \left(\frac{\partial u_{1_0}}{\partial x_3}\right)_{x_{1_0}, x_{2_0}, x_{3_0}} \Delta x_{3_2} \tag{7.3.2}$$

$$u_{1_3} = u_{1_0} + \left(\frac{\partial u_{1_0}}{\partial x_2}\right)_{x_{1_0}, x_{2_0}, x_{3_0}} \Delta x_{2_3} + \left(\frac{\partial u_{1_0}}{\partial x_3}\right)_{x_{1_0}, x_{2_0}, x_{3_0}} \Delta x_{3_3} \tag{7.3.3}$$

Equations 7.3.1 – 7.3.3 form a system of equations that can be written in matrix form as:

$$\begin{bmatrix} u_{1_1} \\ u_{1_2} \\ u_{1_3} \end{bmatrix} = \begin{bmatrix} 1 & \Delta x_{2_1} & \Delta x_{3_1} \\ 1 & \Delta x_{2_2} & \Delta x_{3_2} \\ 1 & \Delta x_{2_3} & \Delta x_{3_3} \end{bmatrix} \begin{bmatrix} u_{1_0} \\ \dfrac{\partial u_{1_0}}{\partial x_2} \\ \dfrac{\partial u_{1_0}}{\partial x_3} \end{bmatrix} \tag{7.3.4}$$

The stream wise derivatives are obtained by applying the momentum equation in each component and neglecting pressure and viscous forces. The final expression yields:

$$\frac{\partial u_{1_0}}{\partial t} + u_{1_0}\frac{\partial u_{1_0}}{\partial x_1} + u_{2_0}\frac{\partial u_{1_0}}{\partial x_2} + u_{3_0}\frac{\partial u_{1_0}}{\partial x_3} = 0 \tag{7.3.5}$$

which can be solved for $\frac{\partial u_{1_0}}{\partial x_1}$, and thus yield:

$$\frac{\partial u_{1_0}}{\partial x_1} = -\frac{1}{u_{1_0}}\left[\frac{\partial u_{1_0}}{\partial t} + u_{2_0}\frac{\partial u_{1_0}}{\partial x_2} + u_{3_0}\frac{\partial u_{1_0}}{\partial x_3}\right] \tag{7.3.6}$$

In a similar fashion the other two stream wise derivatives can be obtained as:

$$\frac{\partial u_{1_0}}{\partial x_2} = -\frac{1}{u_{2_0}}\left[\frac{\partial u_{1_0}}{\partial t} + u_{1_0}\frac{\partial u_{1_0}}{\partial x_1} + u_{3_0}\frac{\partial u_{1_0}}{\partial x_3}\right] \tag{7.3.7}$$

$$\frac{\partial u_{1_0}}{\partial x_3} = -\frac{1}{u_{3_0}}\left[\frac{\partial u_{1_0}}{\partial t} + u_{1_0}\frac{\partial u_{1_0}}{\partial x_1} + u_{2_0}\frac{\partial u_{1_0}}{\partial x_2}\right] \tag{7.3.8}$$

The temporal derivatives, i.e. $\frac{\partial u_{1_0}}{\partial t}$, contained in Equations 7.3.6-8 can be easily computed from differencing two successive velocity values and diving by the sampling frequency interval, Δt.

7.4. Description of Vorticity Measurement Experiments

This chapter describes the experiments performed to investigate the interaction of the expansion waves with grid-generated turbulence. Chapter 8 will be dedicated for results and based on the statistics observed. The turbulent flow is created by a rigid wire mesh previously described, placed in front of the working section.

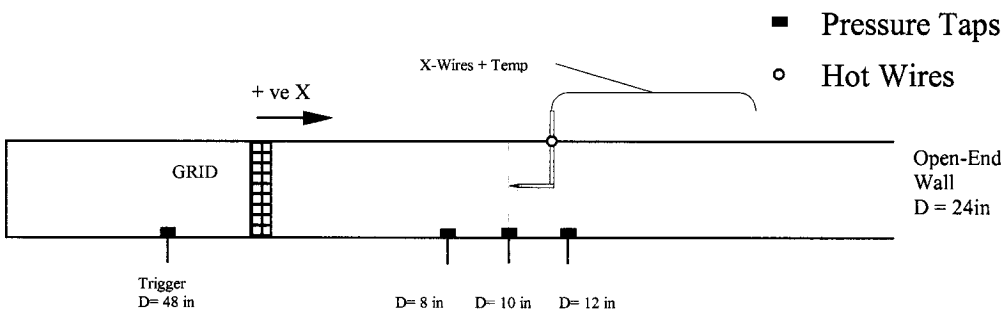

Figure 7.3: Two-dimensional schematic of the working section with pressure and vorticity probe locations along the 2 ft length.

Figure 7.3, describes again the 2 ft working section, since this is the only one used for vorticity measurements. The reader is referred to Chapter 4 for the flow conditions required for turbulence and expansion wave interaction based on the TVD scheme.

Table 7.4 provides all the pertinent experiments and operating conditions for each one.

#	Grid Size	Solidity	X/M	P_2 - psi	M_2	W_s - m/s
1	2x2a	0.39	20	6.35	0.2528	405.0
2	2x2b	0.28	20	6.70	0.2609	407.25
3	3x3	0.39	30	6.75	0.2629	407.75
4	4x4	0.44	40	5.95	0.2368	400

Table 7.4: Vorticity Measurement Experiments.

Turbulence in experiments is characterized by the fluctuating behavior of measured quantities. In grid generated turbulence the fluctuating levels and scales of eddies is dictated by the porosity (open area ratio) of the grid mesh as well as the mesh size. Three different grid sizes were used in the present work; 2x2, 3x3 and 4x4 meshes/inch. Two 2x2 grids with different solidities were utilized to see the effect variable solidity in the same grid size. Again the reader is referred to the CFD chapter where ample comments are presented of the behavior of these grids.

7.5. Decoupling of density and velocity

Mass fluxes were further separated into density and velocity by using the method previously described. In the present work, total temperature was measured directly and therefore no corresponding assumptions were needed. The pressure, however, was measured at the wall and not at the location of the hot wire measurement. The mean value of this pressure signal was used to separate the density and velocity signals since no mean pressure variation has been detected across a given section of the flow. The procedure involves an expression for mass flux, m_i, in terms of total temperature, T_0, and pressure, p, at the centroid of each array:

$$m_i = \rho U_i = \frac{pU_i}{RT} = \frac{pU_i}{R[T_0 - \frac{U_k U_k}{2C_p}]} \qquad (7.5.1)$$

where U_i is the instantaneous velocity component, i=1,2 or 3 and

$$U_k U_k = U_1^2 + U_2^3 + U_3^2$$

The velocity can be decomposed into $U_i = \overline{U}_i + u_i$.

An iterative scheme was used to decouple density and velocity. During the first iteration it was assumed that the quantity, $\frac{u_2^2+u_3^2}{2C_p}$ where u_2 and u_3 are the velocity components in the span wise and normal directions respectively, are substantially smaller that the quantity $T_0-\frac{U_1^2}{2C_p}$. Then Equation 7.5.1 can be rearranged to obtain a quadratic equation for U_i,

$$\frac{Rm_i}{2C_p}U_i^2+pU_i-m_iRT_0=0 \qquad (7.5.2)$$

For each digitized point, T_0 and m_i were available instantaneously at the centroid of each module while pressure was measured at the wall. If the thin shear layer approximation is invoked then the mean pressure at the wall can substitute the pressure at the centroid of the array, which appears in the last equation. This assumption is justified because pressure fluctuations are extremely small and therefore their impact on velocity fluctuations is minimal. The discriminant of the above equation $\Delta=p^2+\frac{2m_i^2R^2T_0}{C_p}$ is always positive, and therefore there are two real roots. The product of the two roots, as expressed by the ratio of the last term of the left hand side of the quadratic equation to the coefficient of the first term, is always negative. Therefore one root is positive and one negative. The negative root is unrealistic and only the positive root was accepted.

7.6. Typical Raw velocity signals from vorticity Probe

This section will provide some of the raw data obtained by the 16 channel, 16bit, 800khz per each channel data acquisition system. Figure 7.4 provides a typical signal

with just two channels out of the usual 16 that are obtained during the experiments. Figure 7.5 is an enlargement of the same signal at the region of interest. Three regions are visible here. The first jump in mass/flux is due to the arrival of the incident shock, followed by the turbulent flow that has passed through the grid. The signals visually seem to be relatively clean devoid of any electronic noise characteristics such as spikes. The second region is that of an accelerating region flow due to the arrival of the expansion wave; significant reduction in the fluctuating levels is visibly seen. After the interaction with the expansion wave, Mass/flux, tends to attain a mean value which is either constant or has a slight deceleration and then with the arrival of the expansion wave from the driver section the signal drops even more. It should be noted here that the hotwires are not able to distinguish the direction of the flow, being a cylinder in the flow, thus the arrival of the expansion waves and the contact surface is observed by the pressure transducer signals which are not plotted here.

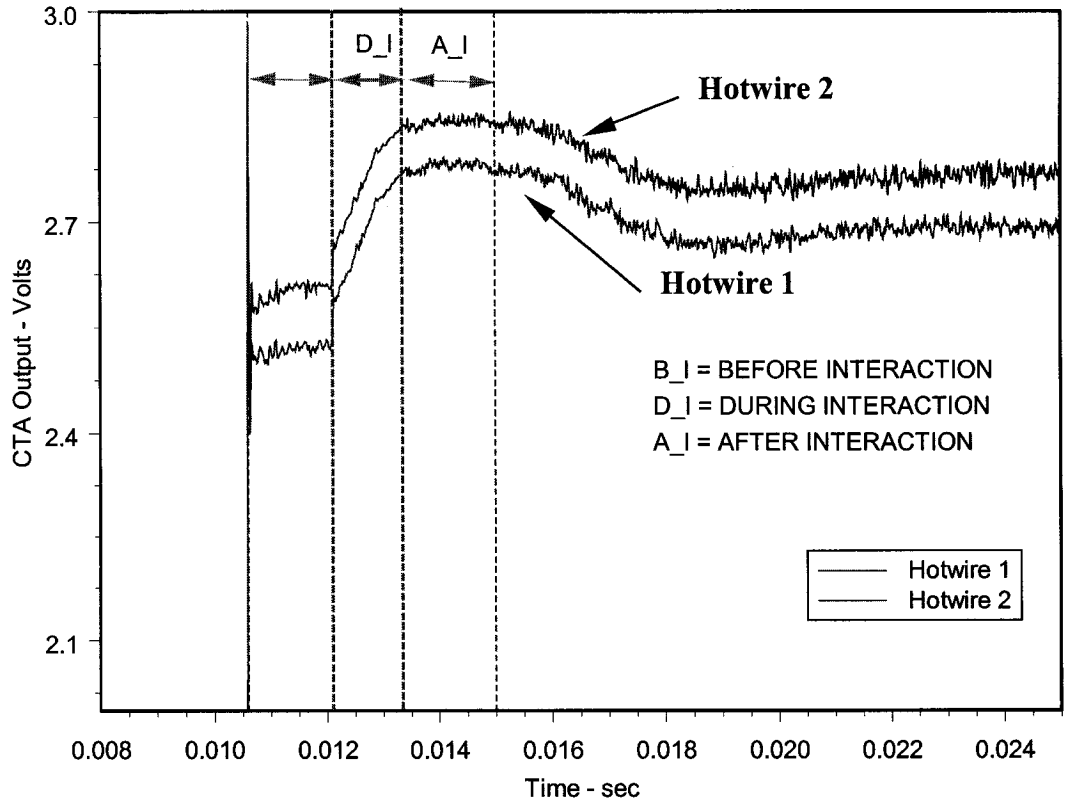

Figure 7.4: Typical hotwire signals during expansion wave interaction.

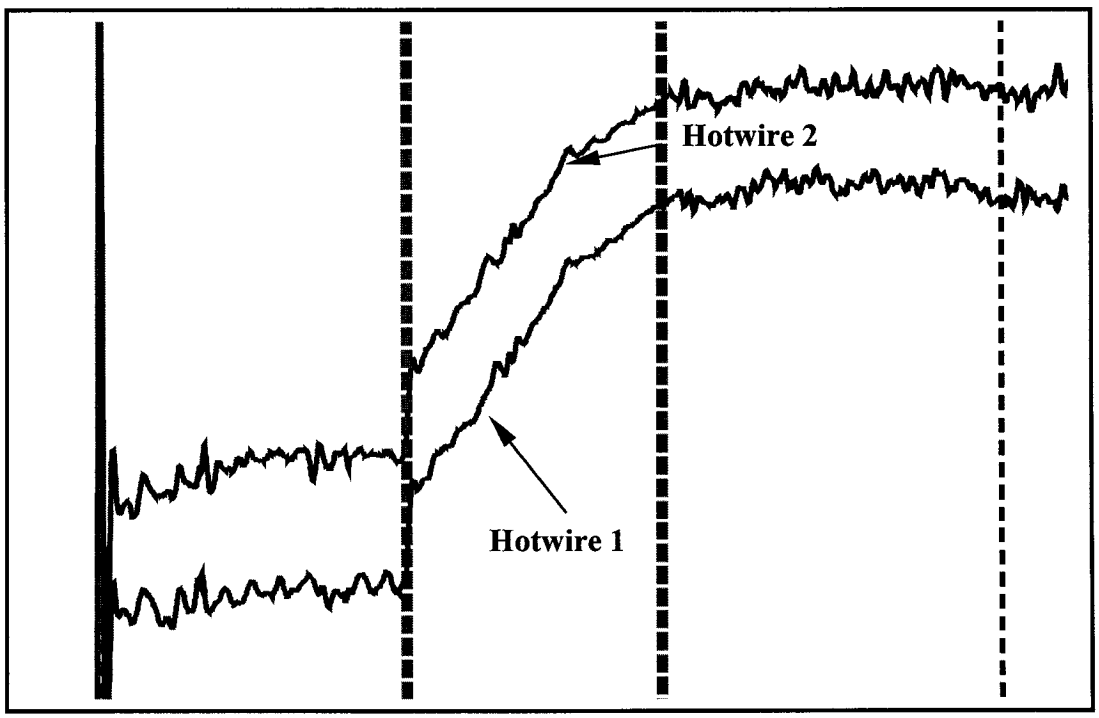

Figure 7.5: Region of interest enlarged.

Chapter 8: Vorticity Results

8.1. Vorticity and enstrophy in the flow field

A better understanding of the nature of the interaction of turbulent structures and vortex motions of turbulent flows with expansion waves requires information on important quantities like vorticity, rate-of-strain tensor and its matrix invariants, and dissipation of turbulent kinetic energy. These flow quantities, although computationally as well as experimentally demanding, when resolved to proper scales, are therefore well suited for describing physical phenomena in vortical flows.

In the present work, however, the transport equations of vorticity and enstrophy will be used to gain further insight of the processes involved in the interactions of shock waves with turbulence by looking at the instantaneous signals of the various quantities involved. The transport equation of vorticity

$$\frac{D\Omega_i}{Dt} = S_{ik}\Omega_k - \Omega_i S_{kk} + \varepsilon_{iq\eta}\frac{1}{\rho^2}\frac{\partial\rho}{\partial x_q}\frac{\partial p}{\partial x_\eta} + \varepsilon_{iq\eta}\frac{\partial}{\partial x_q}\left(\frac{1}{\rho}\frac{\partial \tau_{\eta j}}{\partial x_j}\right) \qquad (8.1.1)$$

describes four dynamically significant processes for the vorticity component Ω_i, namely that of stretching or compression and tilting by the strain S_{ik}, vorticity generation through dilatation, baroclinic generation through the interaction of pressure and density gradients and viscous effects expressed by the viscous stress term. The term $S_{ik}\Omega_k$ consists of one stretching or compression component and two tilting components. This term presumably plays an important role in the various processes involved which is not yet fully understood. The viscous term may also describe reconnection of vortex lines at very small scales due to viscosity. If the viscous term can be ignored since its magnitude, very

often is small, then the change of vorticity of a fluid element in a Lagrangian frame of reference can be entirely attributed to vortex stretching and/or tilting, to dilatational effects and to baroclinic torque.

If the above equation is multiplied by Ω_i, then the transport equation for the enstrophy equation $\frac{1}{2\Omega_i\Omega_i}$ can be obtained:

$$\frac{D(1/2\Omega_i\Omega_i)}{Dt} = S_{ik}\Omega_k\Omega_i - \Omega_i\Omega_i S_{kk} + \varepsilon_{iqn}\frac{1}{\rho^2}\Omega_i\frac{\partial\rho}{\partial x_q}\frac{\partial p}{\partial x_n} + \varepsilon_{iqn}\frac{\partial}{\partial x_q}\left(\Omega_i\frac{1}{\rho}\frac{\partial\tau_{nj}}{\partial x_j}\right) - \varepsilon_{iqn}\frac{1}{\rho}\frac{\partial\Omega_j}{\partial x_q}\frac{\partial\tau_{nj}}{\partial x_j}$$

(8.1.2)

The physical meaning of the terms associated with the time-dependant changes of enstrophy of a fluid element in a Lagrangian frame of reference are similar with those responsible for the generation or destruction of vorticity.

Figures 8.1-8.4 show signals of longitudinal velocity component U_1, lateral velocity component U_2, longitudinal, lateral and transverse vorticity components Ω_1, Ω_2 and Ω_3 respectively, the enstrophy $\Omega_i\Omega_i$, wall pressure and total temperature for each of the experiments with four different grids. Each signal has been normalized by its r.m.s. value upstream of the interaction. As a result, signals with relatively large fluctuations are reduced and signals with relatively small fluctuations are expanded. Thus, all signals have been brought to about the same amplitude level. This normalization also helps to observe whether the signal of the particular quantity is attenuated or not during or after the interaction. This is because the r.m.s. value of this portion of the signals is the attenuation/gain G which is defined in terms of a representative variable Q as the ratio

$G = \frac{Q_{rms,d}}{Q_{rms,u}} = \frac{\sigma_d}{\sigma_u}$ where the superscripts **u** and **d** denote regions upstream and downstream of the interaction respectively.

Each of the signals, with the exception of that of U_1, has been displaced by multiples of 100 r.m.s. units to provide better visual aid. Pressure signals have been simply displaced by 400 units and amplified by a factor of 10. The arrival of the expansion waves is evident by the slow increase in velocity, the slow decrease in pressure and T_0.

An inspection of the level of fluctuations during or after the passage of the expansion waves and actual computation of their r.m.s. values indicates that some signals are attenuated and some not. The longitudinal vorticity Ω_1 and lateral velocity components U_2 and U_3 signals are expected to be only slightly affected by the interaction.

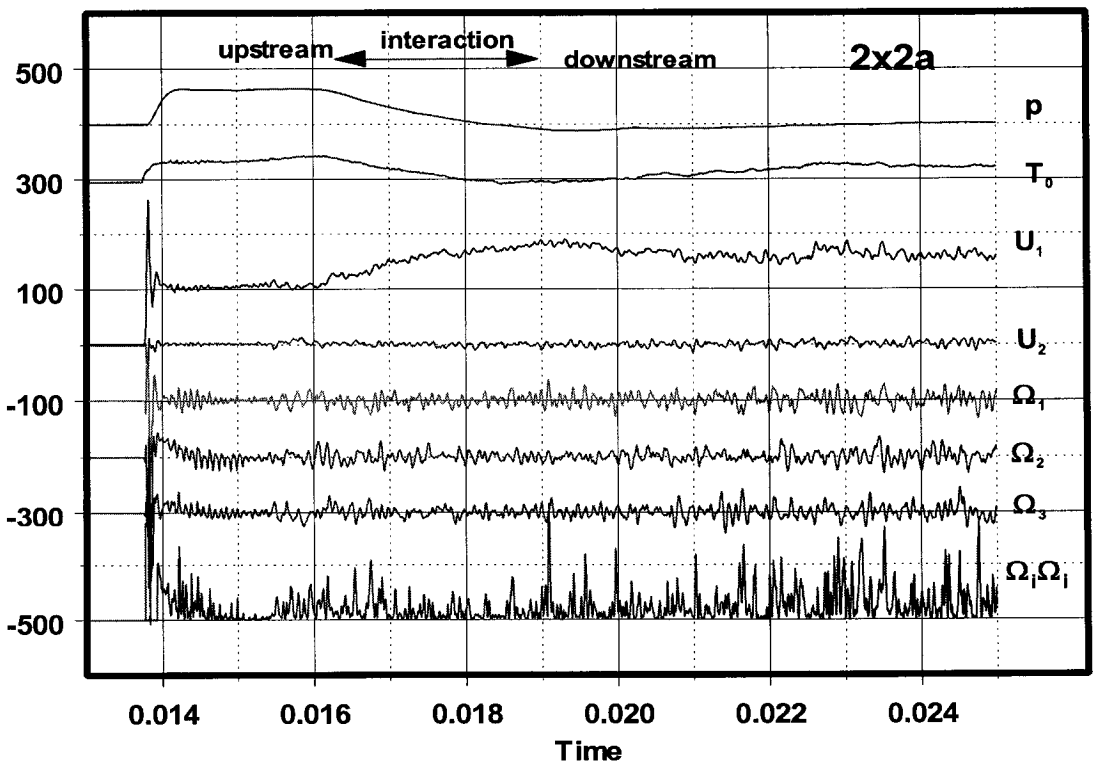

Figure 8.1: Typical signals in the experiment with the 2x2a grid.

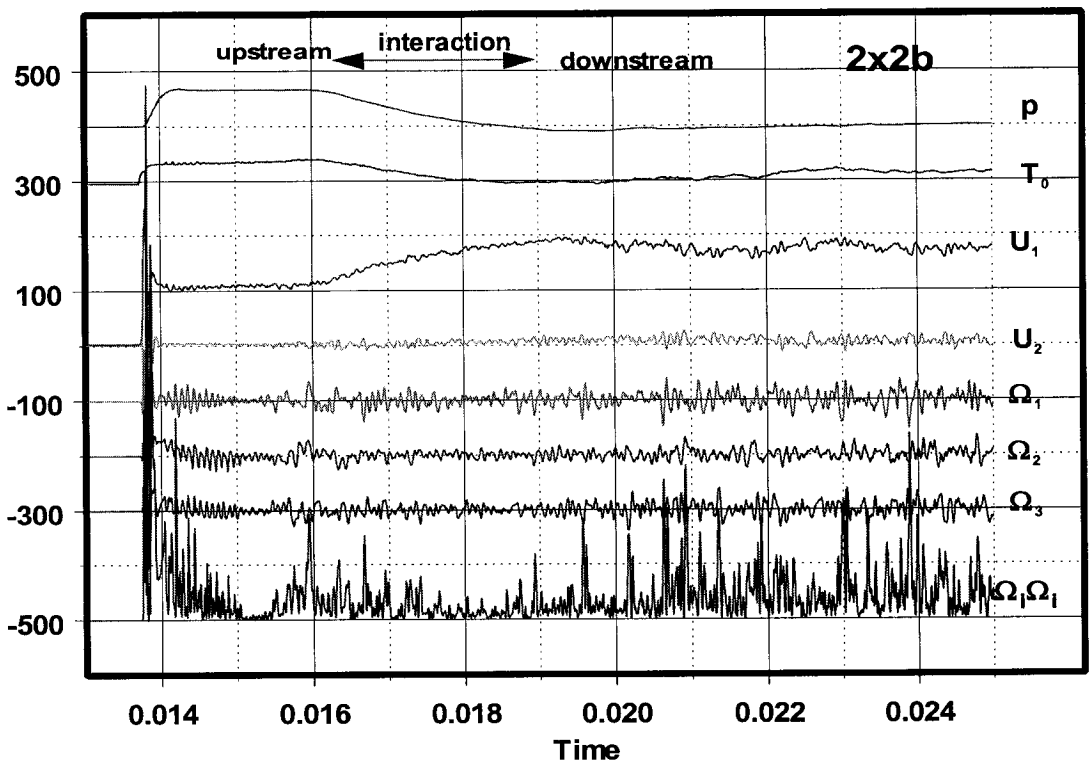

Figure 8.2: Typical signals in the experiment with the 2x2b grid.

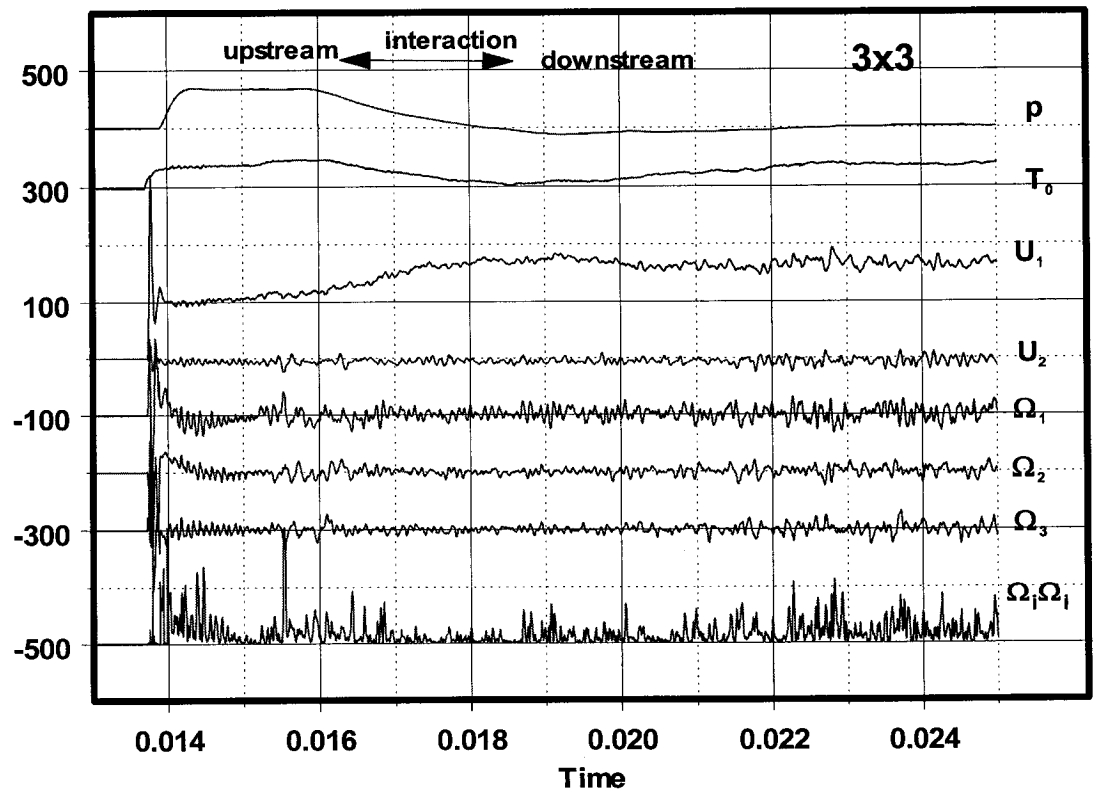

Figure 8.3: Typical signals in the experiment with the 3x3 grid.

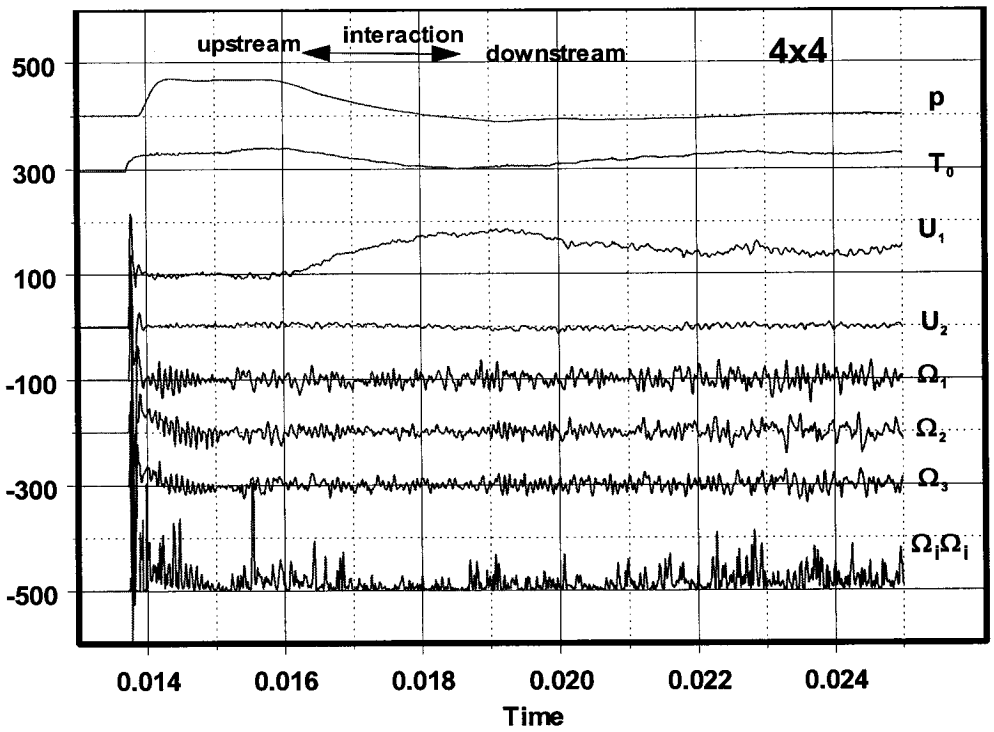

Figure 8.4: Typical signals in the experiment with the 4x4 grid.

Figures 8.5, 8.6 and 8.7 show some typical probability density function distributions of fluctuations of the three vorticity components before and after the interaction. Longitudinal fluctuations are very little affected by the interaction, while the two lateral components are reduced substantially. Similar attenuation can be observed in the fluctuations of enstrophy as shown in the p.d.f distribution of Figure 8.8.

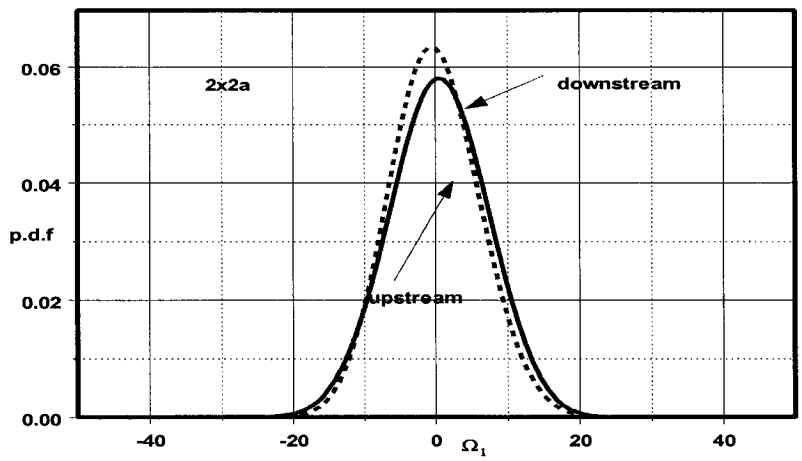

Figure 8.5: Typical probability density function of longitudinal fluctuations 2x2a.

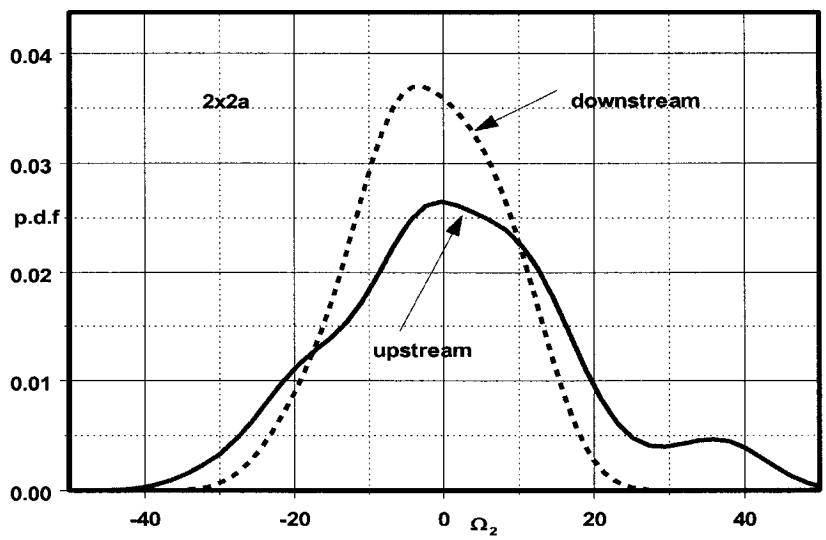

Figure 8.6: Typical probability density function of lateral vorticity fluctuations 2x2a.

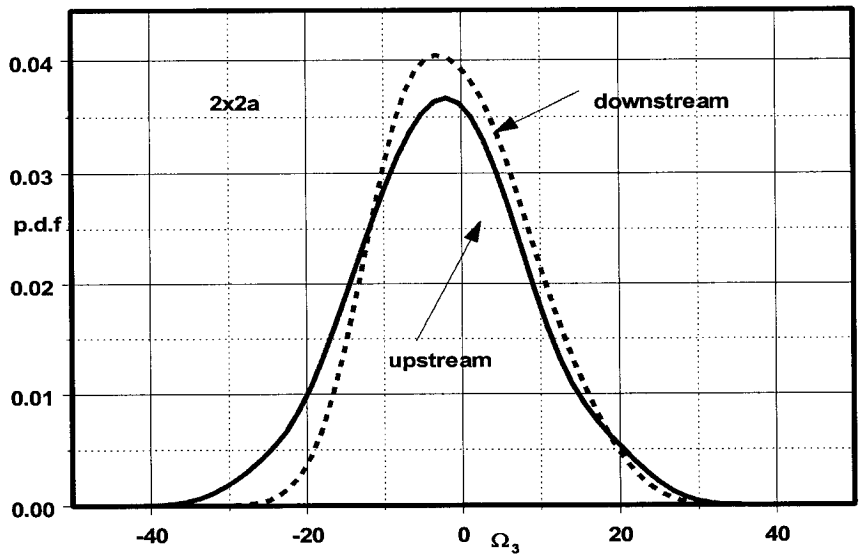

Figure 8.7: Typical probability density function of lateral vorticity fluctuations 2x2a.

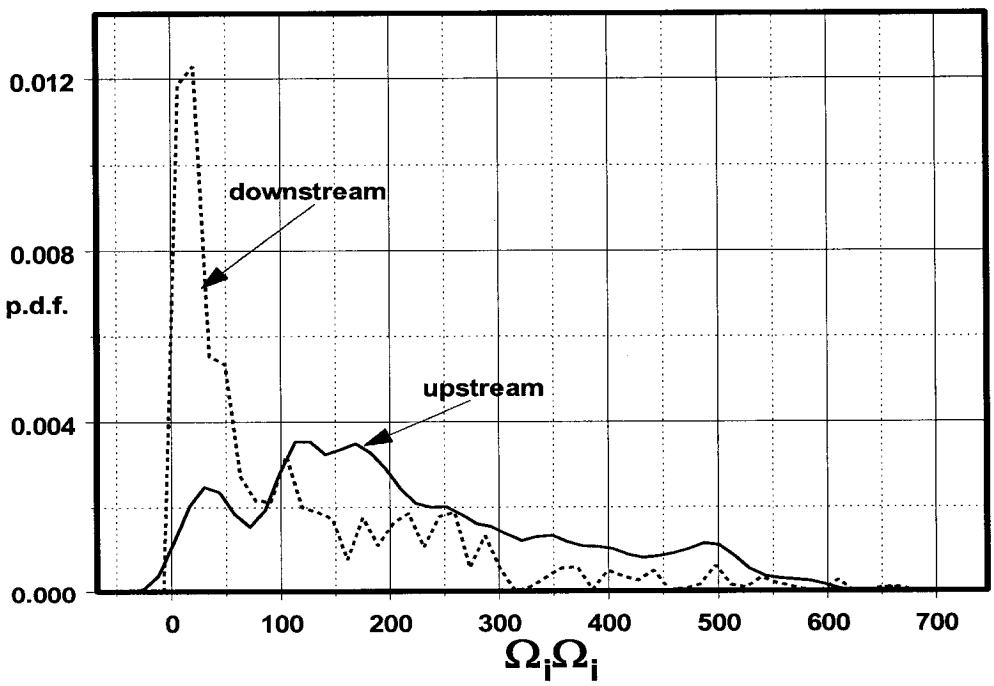

Figure 8.8: Typical p.d.f. of enstrophy fluctuations.

In flows where turbulence is distorted by a rapidly applied strain, like the strain $S_{11} = (\frac{\partial U_1}{\partial x_1})_{EW}$ in the present case across the shock wave, the dissipative time scale of turbulence or eddy turnover time $T_\varepsilon = \frac{L_\varepsilon}{q}$, where L_ε is the dissipation length scale and $q = (\frac{1}{2} U_i U_i)^{\frac{1}{2}}$ should be directly compared to the time scale of the applied strain $T_{EW} = \frac{1}{S_{11}}$. The dissipation length scale, L_ε, is defined as $L_\varepsilon = \frac{q^3}{\varepsilon}$, where ε is the dissipation rate of turbulent kinetic energy, q^2. The time T_t then appears to be $T_t = \frac{q^2}{\varepsilon}$. This time scale indicates how fast the kinetic energy of a typical turbulent eddy is dissipated into heat. The full dissipation rate has been evaluated in the present work. In this case $E = E_s + E_d$ with

$$E_S = \mu \Omega_k \Omega_k + 2\mu \left[\frac{\partial U_i}{\partial x_j} \frac{\partial U_j}{\partial x_i} - S_{kk} S_{kk} \right] \text{ and } E_d = 4/3 \mu S_{kk} S_{kk} \quad (8.1.3)$$

The strain rate S_{11} that is associated with the imposed disturbance of the incoming expansion wave can be approximated by $S_{11} = (\frac{\partial U_1}{\partial x_1})_{EW} \approx \frac{\Delta U_{EW}}{\Delta x_{EW}}$ where ΔU_{EW} is the velocity difference across the Expansion Wave and Δx_{EW} is its typical thickness. This can be approximated by $\Delta x_{EW} = \Delta t_{EW} U_c$, where is Δt_{EW} is the duration of the expansion zone and $(U_c - U_2)$ is its convective velocity, which is approximated to be the speed of sound in the upstream zone.

The ratio of two time scales $R_t = \frac{T_t}{T_{EW}} = S_{11}\frac{\varepsilon}{q^2}$ is plotted vs Re_λ in Figure 8.9. The data show that the time scale of turbulent eddy turn-over is about 1000 time greater than the time scale of the interaction. It also appears that R_t grows slightly with Re_λ. There is no strong dependence of R_t on Re_M as shown in Figure 8.10.

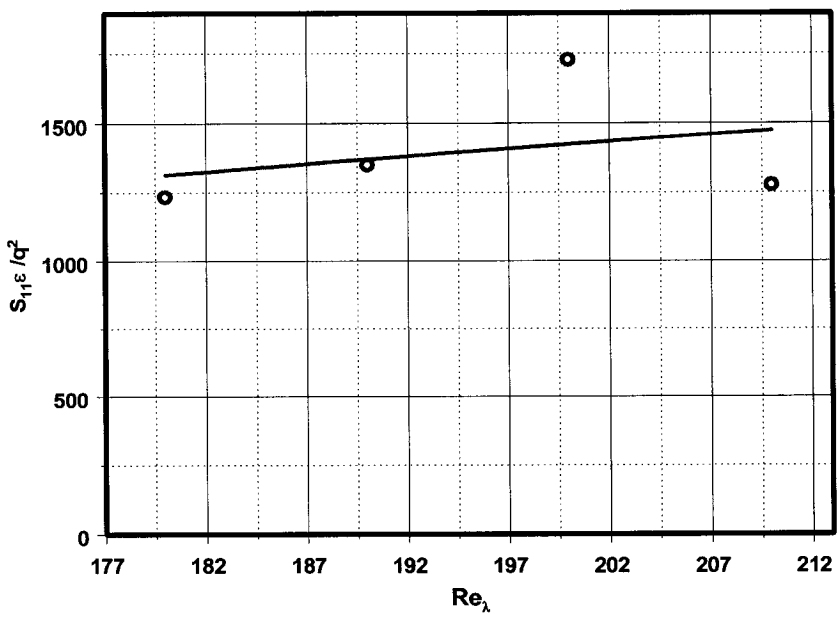

Figure 8.9: Ratio of time scales as a function of Re_λ

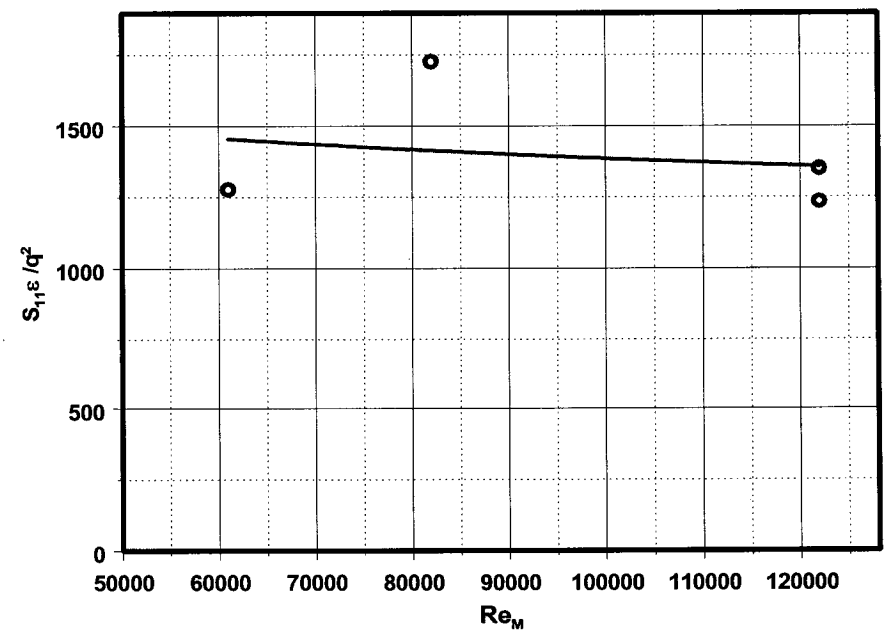

Figure 8.10: Ratio of time scales as a function of Re_M.

Table 8.1 shows a summary of the computed data obtained with the vorticity probe. Figure 8.11 shows the ratios of the standard deviations $G = \frac{\sigma_d}{\sigma_u}$ for the longitudinal and lateral velocity and vorticity fluctuations. It appears that lateral vorticity fluctuations attenuated the most with ratios between 0.74 and 0.42. The data also show that the attenuations increase with Re_λ. Clear evidence of some attenuation is shown in the data of longitudinal velocity fluctuations, although small amplification is measured in one experiment. Longitudinal vorticity fluctuations show a constant behavior throughout all Re_λ. Lateral velocity fluctuations show some rather weak dependence on Re_λ.

The attenuation of turbulent kinetic energy and turbulence intensity is shown in Figure 8.12. In both cases attenuation seems to increase with Re_λ.

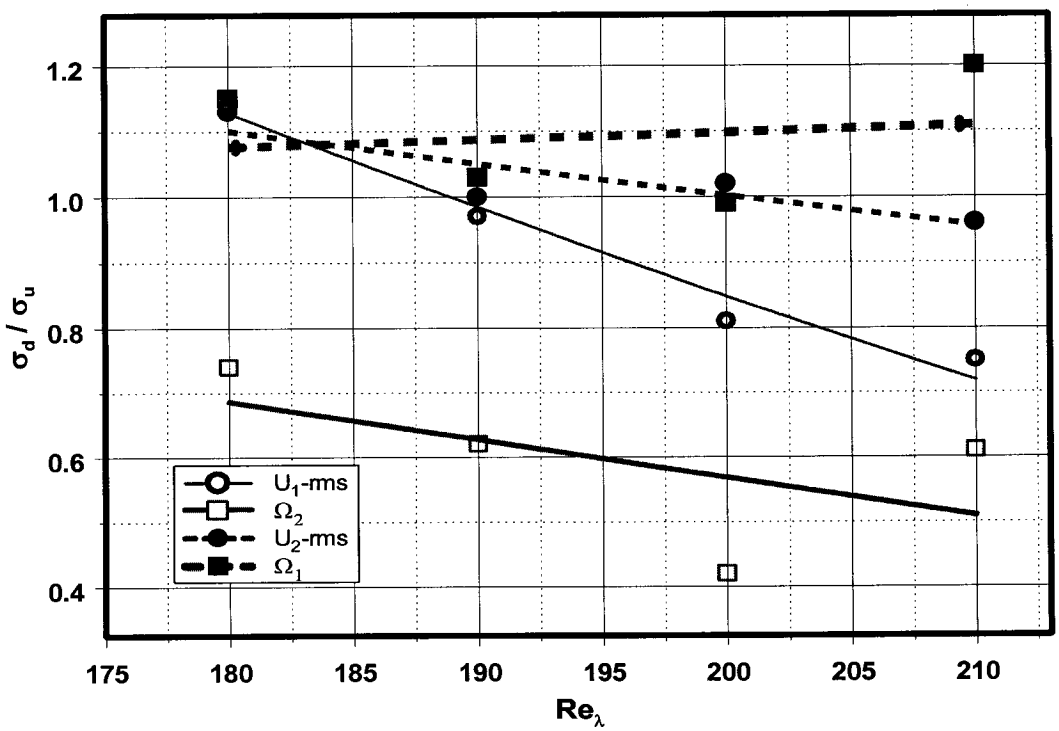

Figure 8.11: Attenuation of velocity and vorticity fluctuations.

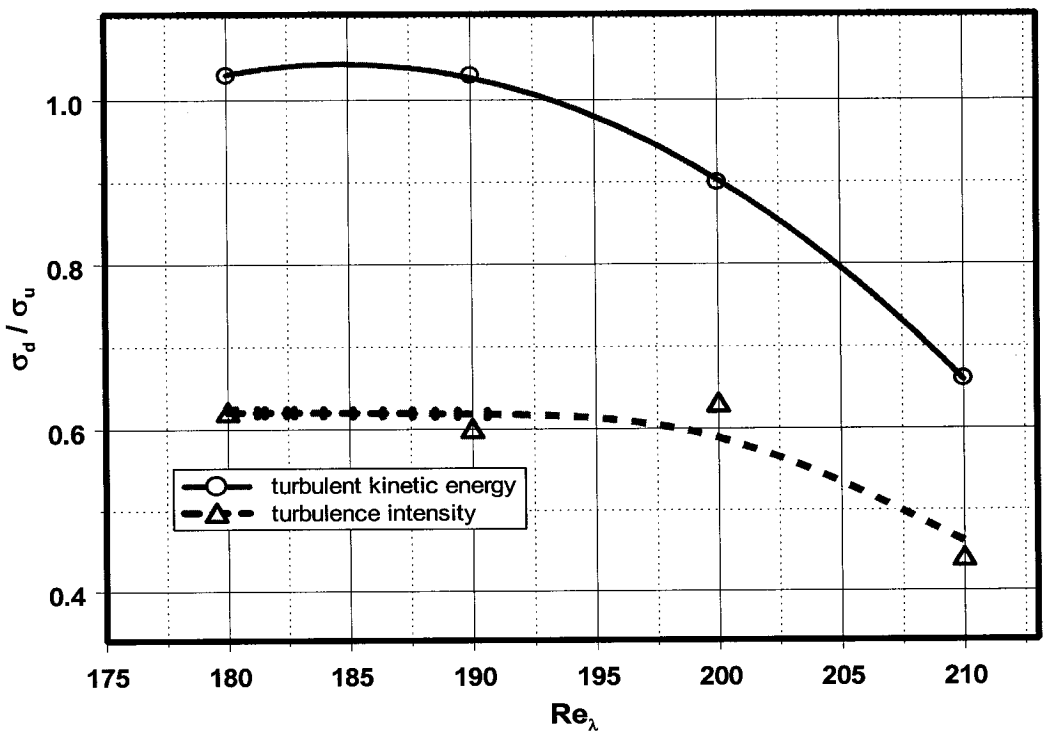

Figure 8.12: Attenuation of turbulence intensity and turbulent kinetic energy.

Grid	U_1	u_1'	u_2'	u_3'	$1/2u_iu_i$	q/U_1	Δt_{EW} ms	ΔU_{EW}	S_{11} Hz	E 10^3	Re_M 10^3	σ	Re_λ	$S_{11}\varepsilon/q^2$ 10^3	Ω_1'	Ω_2'	Ω_3'	$\Omega_i'\Omega_i'$ 10^6
2x2a																		
Upstream	107	3.53	3.93	5.4	28.5	0.0499	2.8	73	96	0.408	122	0.39	190	1.35	27.9	15.4	9.9	11.38
Downstream	180.0	3.44	4.29	5.03	29	0.0299									8.7	7.9	9.9	
Ratio σ_d/σ_u	1.68	0.97	1.09	0.93	1.03	0.599									1.03	0.56	0.79	
	1.68	**0.97**	**1.00**		**1.03**	**0.599**									**1.03**	**0.67**		
2x2b																		
Upstream	109	3.43	3.35	3.32	22.2	0.043	3	79.4	99	0.308	122	0.28	180	1.24	2.17	1.53	0.837	7.8
Downstream	188.4	4.07	3.81	4.01	25.63	0.026									2.51	1.01	0.708	
Ratio σ_d/σ_u	1.73	1.17	1.17	1.20	1.15	0.62									1.15	0.66	0.84	
	1.73	**1.17**	**1.13**		**1.03**	**0.62**									**1.15**	**0.74**		
3x3	116.5	5.58	4.63	5.33	40.5	0.054	3	57	70	1.00	82	0.39	200	1.73	3.13	2.23	2.02	27.8
Upstream	173.2	4.53	4.78	5.46	36.59	0.034									3.16	0.89	0.93	
Downstream	1.485	0.81	1.03	1.02	0.9	0.629									0.99	0.39	0.44	
Ratio σ_d/σ_u	**1.485**	**0.81**	**1.02**		**0.9**	**0.629**									**0.99**	**0.42**		
4x4																		
Upstream	95.4	3.43	2.75	4.43	19.47	0.046	2.5	77.8	116	.215	61	0.44	210	1.28	2	1.06	0.86	5.8
Downstream	173.23	2.58	2.31	3.68	12.76	0.02									2.4	0.54	0.62	
Ratio σ_d/σ_u	1.81	0.75	0.93	0.93	0.656	0.44									1.2	0.51	0.72	
	1.81	**0.75**	**0.93**		**0.656**	**0.44**									**1.2**	**0.61**		

Table 8.1: Summary of vorticity probe measurements.

8.2. Spectral Densities

Some further insight into the evolution of turbulence through the expansion wave can be obtained by looking into the one-dimensional wave number spectra (power spectral densities) of turbulent kinetic energy and of enstrophy, which describe the translational kinetic energy relatively to the mean and the rotational kinetic energy respectively. Figure 8.13 shows spectra of $\frac{1}{2}U_iU_i$ and $\frac{1}{2}\Omega_i\Omega_i$ upstream and downstream of the interaction obtained in the flow with the 4x4 grid. These spectra have been computed from frequency spectra after invoking Taylor's hypothesis with convection velocities those of the mean velocities U_u and U_d for the upstream and downstream of the expansion wave regions. This is based on the assumption that the frequency of the waves, ω, remains unchanged by the interaction and that the associated wave number, K_1, changes to satisfy the dispersion relation $\omega - k_1U_c = 0$ where U_c is the convection velocity. Because of the difference in U_c the upstream and downstream wave number range will be different. The present choice of convection velocities refers to the laboratory system of reference as opposed to the alternative one moving with the wave, which requires different convection velocities. Values of the streamwise wave number K_1 have been non-dimensionalized by the mesh size M.

The upper limit in the wave number scales is defined by the resolution of the instrumentation and the lower limit, i.e. the larger eddies are defined by the shock tube diameter D. Thus the ratio of the largest to smallest resolvable scales is about 300:1.

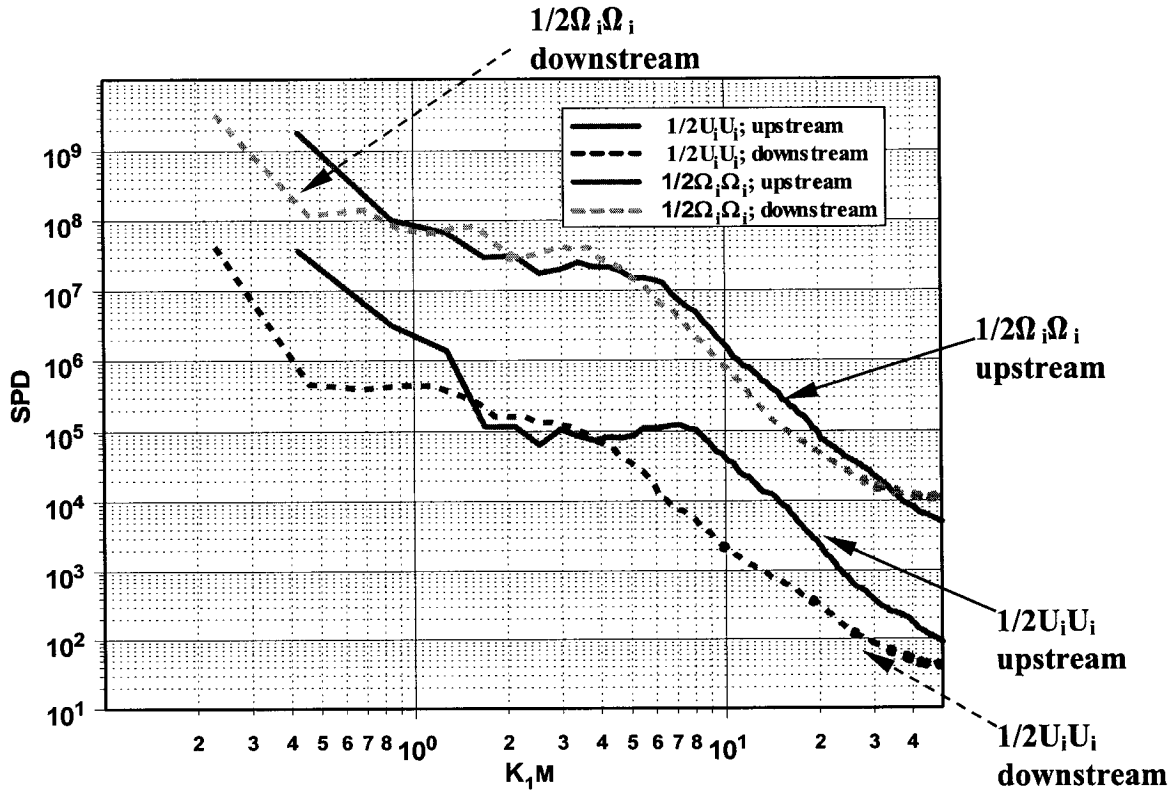

Figure 8.13: Spectral Density - 4x4 Grid.

Through the interaction the spectral content of both turbulent kinetic energy and enstrophy changes significantly. The most revealing pattern is that after the interaction the spectrum shifts to lower wave numbers. This clearly indicates that the length scales of the flow changed substantially. It appears that they increase through the interaction. There is also attenuation of turbulent kinetic energy almost across the whole wave number spectrum. The spectra of enstrophy also show a similar shift of energy towards lower wave numbers but a lesser shift in turbulent kinetic energy.

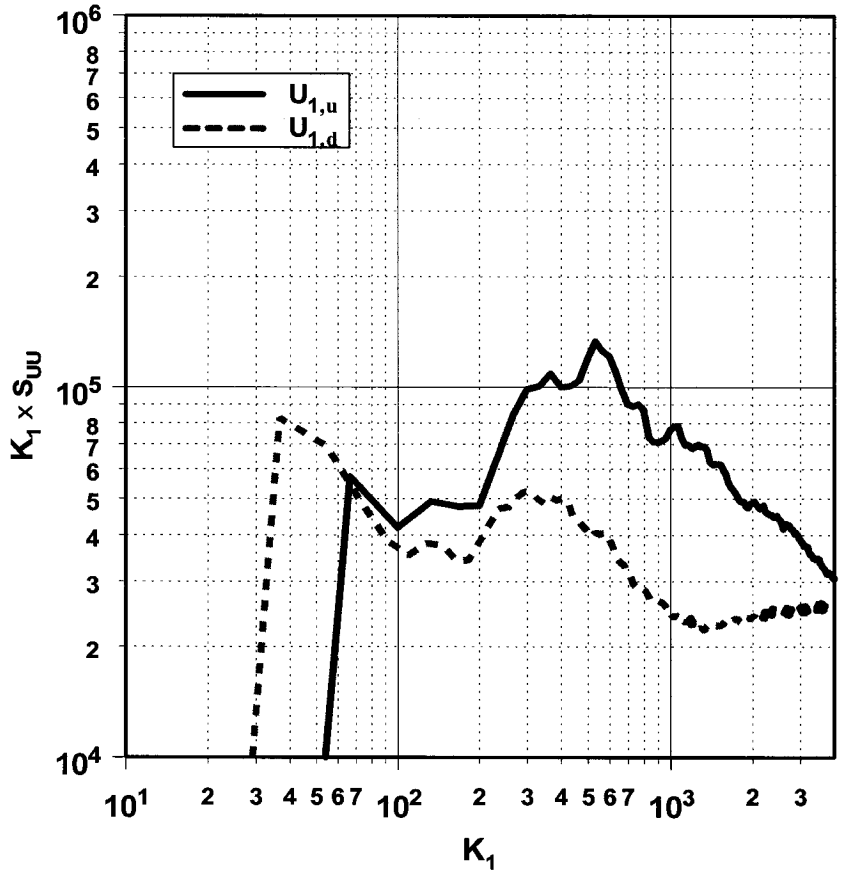

Figure 8.14: Spectral Density of longitudinal velocity fluctuations - 4x4 Grid.

Spectral densities weighted by the wave number K_1 of the longitudinal velocity fluctuations are shown in Figure 8.14. The data show that there is a shift towards lower wave numbers. It is also interesting to observe that the K_1 location where the maximum density occurs also shifts towards lower wave numbers.

The spectral densities of the longitudinal vorticity fluctuations, which are shown in Figure 8.15, indicate a different behavior. The small scales are attenuated while the large scales are amplified. There is a wave number region, 90 m^{-1} $<K_1<$300 m^{-1} which corresponds to wave lengths $3.3<\lambda/M<11$, which shows no amplification or attenuation through the interaction.

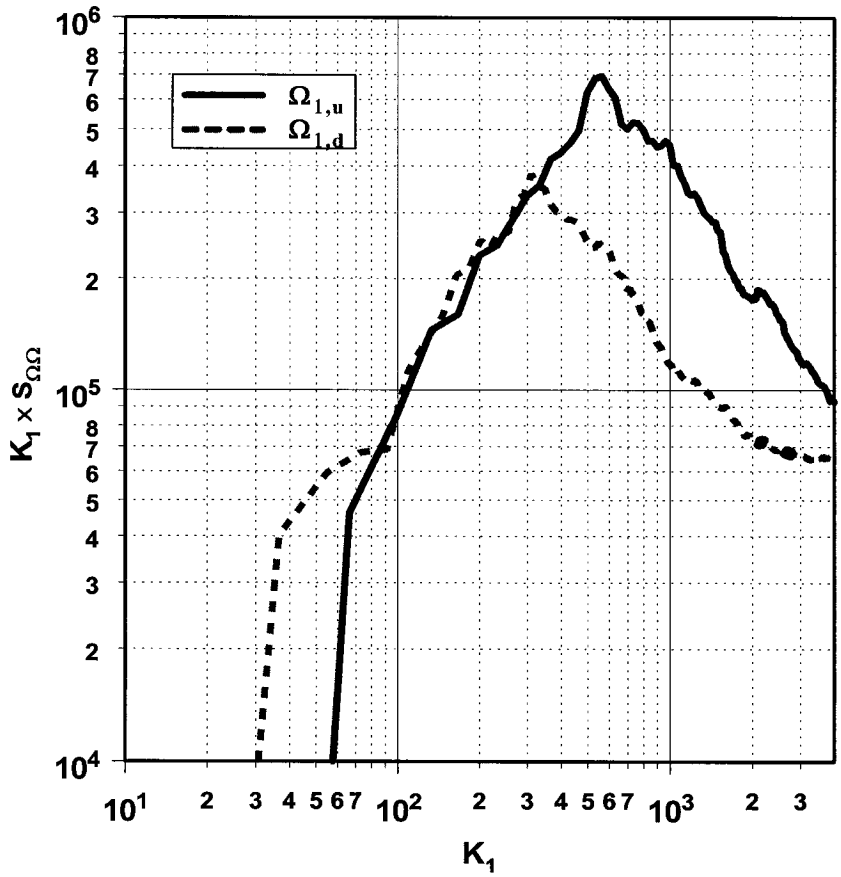

Figure 8.15: Spectral Density of longitudinal vorticity fluctuations - 4x4 Grid.

Figure 8.16 shows the spectral densities of the lateral vorticity fluctuations before and after the interaction. The peak appears to be shifted towards lower wave numbers and also the amplitude of the fluctuations is suppressed significantly.

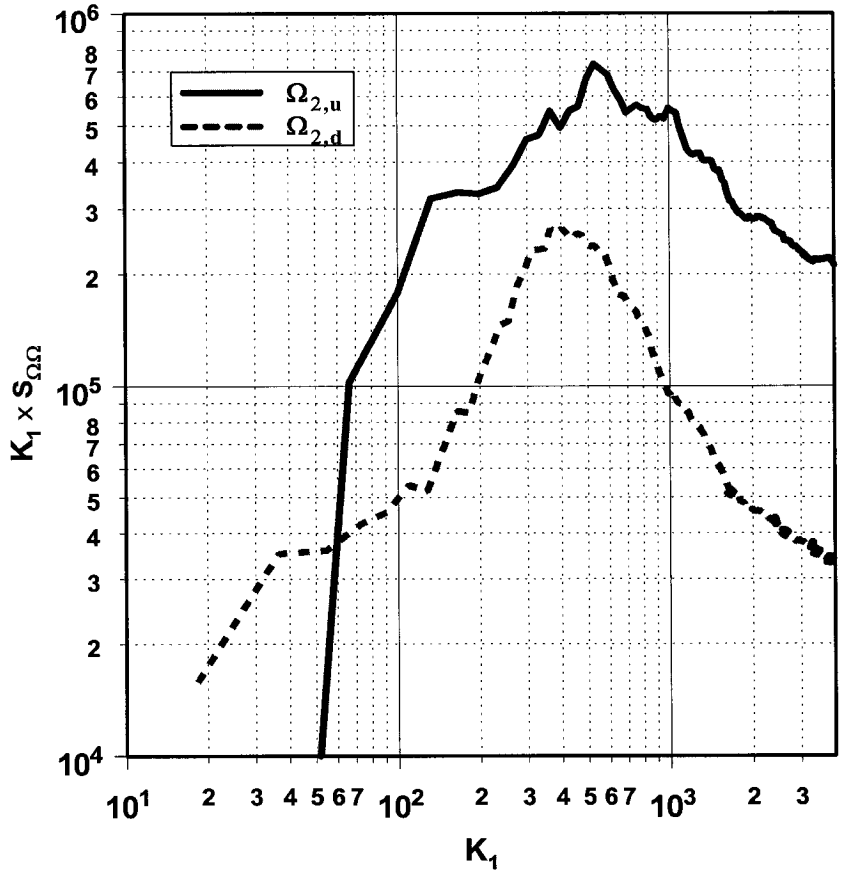

Figure 8.16: Spectral Density of lateral vorticity fluctuations - 4x4 Grid.

Chapter 9: Conclusions

An attempt has been made to investigate experimentally the effects of flow expansions caused by moving expansion waves on isotropic turbulence in a large scale shock tube facility by employing multiple hot-wire probes of various types and related instrumentation with high spatial and temporal resolution.

The incident shock and the induced flow behind it passed through a rectangular grid, which generated a nearly homogeneous and nearly isotropic turbulence. As the shock wave exited the open end of the shock tube a system of expansion waves was generated which traveled upstream and interacted with the grid-generated turbulence. This type of interaction is free from streamline curvature effects, which cause additional effects on turbulence.

CFD was used systematically to design the experiment, identify useful time windows and understand the bulk behavior of the incoming flow.

The flow field was generated by using a variety of grids of rectangular pattern of different mesh size. The Reynolds number of the flow based on the mesh size, Re_M, ranged from 50,000 to 200,000 while the turbulent Reynolds number Re_λ based on Taylor's micro scale was between 150 and 250 which is reasonably high a laboratory flow. The Mach number of the incoming flows investigated was about 0.3. In that respect these interactions are considered as interactions with an almost incompressible flow. Mild interactions with expansion waves which generated expansion ratios of the order of 1.8 were achieved in the present investigations. In that respect the compressibility effects

started to become important during the interaction. The ratio of the eddy turnover time to that of the strain rate of the interaction reached values of the order of 10^3.

A custom designed vorticity probe was used to measure for the first time the rate-of-strain, the rate-of-rotation and the velocity-gradient tensors in several of the present flows. Testing and validation of the probe and its eventual use in the shock tube flow field were a formidable task. Issues related to calibration, data analysis and spatial and temporal resolutions appeared to be the most significant among all that were considered.

Custom made x-hot-wire probes were also used to measure the flow quantities simultaneously at different locations inside the flow field.

Although the strength of the generated expansion waves was mild, $S = \left[\frac{\partial U}{\partial x}\right]_{EW} = 50$ to100 s^{-1}, the effect on damping fluctuations of turbulence was clear. In this experiment, time- and space-resolved three-dimensional vorticity was measured for the first time. Vorticity fluctuations were reduced dramatically more than velocity or pressure fluctuations.

Attenuation of longitudinal velocity fluctuations has been observed in all experiments. It appears that the attenuation increases in interactions with higher Reynolds number. The data of velocity fluctuations in the lateral directions show no consistent behavior change or some minor attenuation through the interaction. These results indicate that the outcome of the interaction depends strongly on the upstream turbulence of the flow.

The present results clearly show that in most of the cases, attenuation occurs at large $\frac{x}{M}$ distances where length scales of the incoming flow are high and turbulence

intensities are low. Thus large in size eddies with low velocity fluctuations are affected the most by the interaction with the expansion waves. Spectral analysis indicated that spectral energy is shifted after the interaction to lower wave numbers suggesting that the typical length scales of turbulence are increased after the interaction.

Appendix A: Formation of Compression and Expansion Waves

A.1. Formation of Compression and Expansion Waves

Prior to describing the formation of compression and expansion waves and the principle of operation of a shock tube, the definition and physical meaning of the speed of sound is required.

A.1.1. The Speed of Sound

The physiological effects of speech and hearing are related to the transmission and detection of tiny pressure disturbances because of the elastic nature of the fluid. The speed at which these disturbances travel is commonly known as the speed of sound, denoted by V_s here and it depends on the compressibility of the medium in which it propagates into. The aim here is to demonstrate how infinitesimal pressure, density and enthalpy disturbances propagate through a compressible fluid. One might speculate that the speed of sound would depend on the specific properties of the transmitting fluid and perhaps on the magnitude of the pressure or sound disturbances themselves.

In order to relate the above-mentioned effects in a qualitative way, a homogenous compressible fluid of pressure p, density ρ, and enthalpy h at rest in a piston tube with a uniform cross-section is considered as shown in Figure A.1 Assume that that tube is thermally insulated and the piston contained is close-fitted yet frictionless. This assumption and under the restriction of small pressure disturbances, the process can be considered reversible and isentropic. If the piston is given a steady velocity ΔV to the right, an infinitesimal pressure pulse will be generated at the face of the piston, which will propagate to the right at a velocity V_s. The fluid is compressed in front of the piston

and the pressure, density and enthalpy increase slightly to p+Δp, ρ+Δp and h+Δh respectively. Behind this advancing front, the properties remain constant at their increased value as long as the piston continuous to move steadily. The fluid behind the front moves at the same speed as the piston (ΔV) while the fluid in front of the advancing pulse remains stationary. Considering the advancing front as stationary by choosing a reference frame moving steadily at the speed V_s and by applying the equations governing conversation of mass and momentum, the speed of sound V_s is given by:

$$V_s^2 = \frac{\Delta p}{\Delta \rho}(1+\frac{\Delta \rho}{\rho}) \quad \text{.....(A.1.1)}$$

given that $\frac{\Delta \rho}{\rho} << 1$, for infinitesimal disturbances and under adiabatic and reversible conditions, $\frac{\Delta p}{\Delta \rho}$ can be interpreted as the partial derivative of p with respect to ρ at constant entropy, $(\frac{\partial p}{\partial \rho})_s$. Thus the expression for the speed of sound A.1 becomes:

$$V_s^2 = \alpha^2 = (\frac{\partial p}{\partial \rho})_s \quad \text{.....(A.1.2a)}$$

$$V_s = \sqrt{(\frac{\partial p}{\partial \rho})_s} \quad \text{.....(A.1.2b)}$$

and for a perfect gas, since $(\frac{\partial p}{\partial \rho})_s = \gamma(\frac{\partial p}{\partial \rho})_T$ equation A.2a becomes:

$$V_s^2 = \alpha^2 = \gamma RT \quad \text{.....(A.1.3)}$$

The relative magnitude of fluid speed and the speed of sound is of great importance and is usually measured by the Mach number, $M = \frac{V}{a}$. This number has a physical importance much like the Reynolds, Nusselt and other dimensionless groups and

is proportional to the square root of the ratio of the inertial to elastic or compressive forces. Another interpretation for the Mach number is given as the ratio of the time necessary for a pressure signal to travel a fixed distance to the time necessary for a fluid particle to cover the same distance.

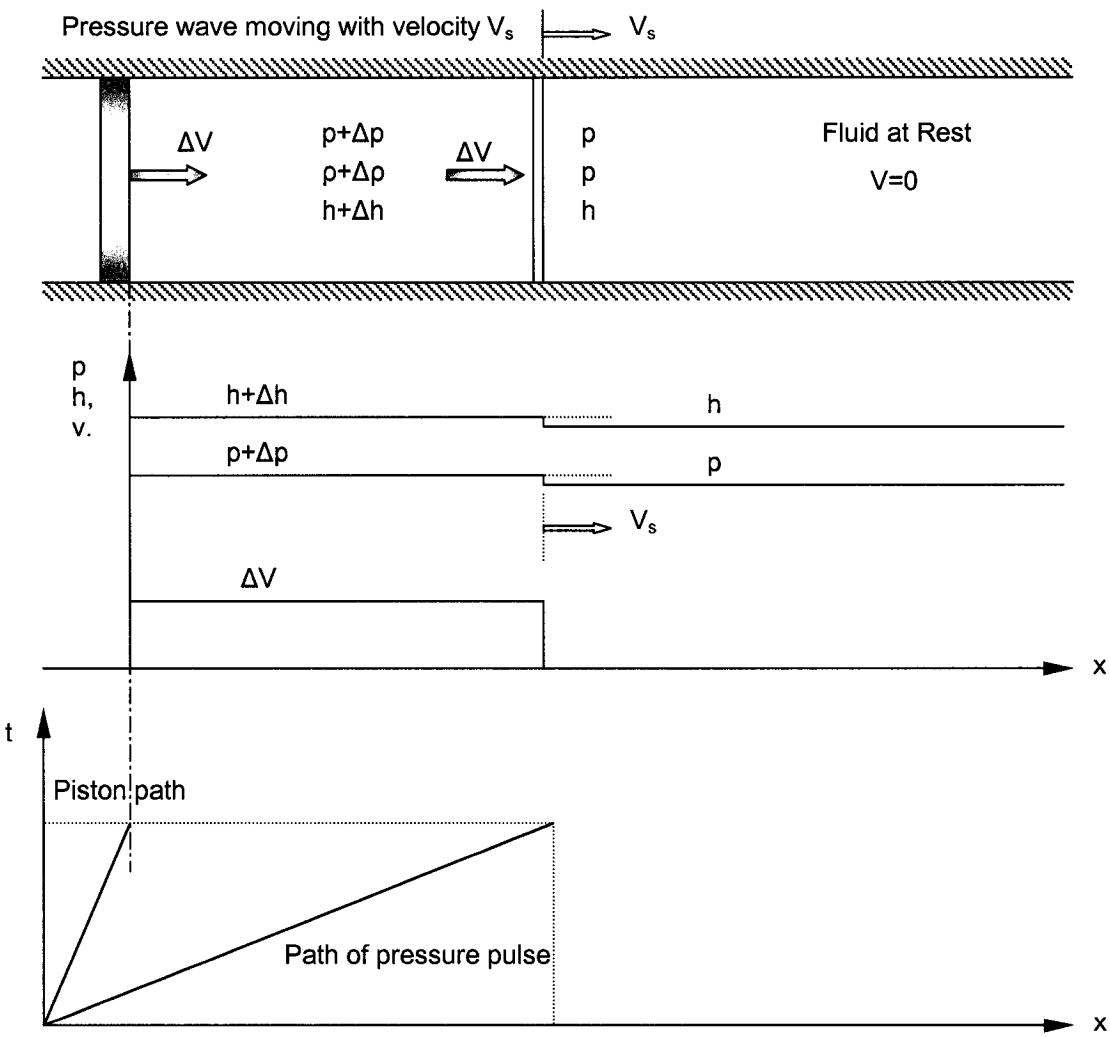

Figure A.1: Propagation of a weak pressure wave along a tube with a compressible fluid based on a stationary observer.

A.2. Shock Waves

Now that the speed of sound and the propagation of small pressure disturbances have been elaborated on, the development of a compression shock wave as well as an expansion wave is considered. To observe in a qualitative manner how a finite discontinuity can be formed reexamining the piston-tube arrangement described before and with the aid of Figure A.2, the formation of a compression wave is illustrated. A slight steady movement of the piston produces a weak compression wave (a sound wave) that propagates through the gas at rest. If the piston velocity is now increased a second time, a second compression wave forms and also moves along the tube. This wave travels at a higher sonic speed than the first because the gas into which it travels is at a higher temperature as a result of the compression produced by the first wave. The second wave thus has a higher absolute velocity than the first wave. For a third increment in speed, the process is repeated and the generated sonic wave is inclined to overtake the first two. The successive compression waves generated by the successive accelerations, see Figure A.2a, of the piston tend to reinforce each other, causing an abrupt contour of the wave. The pressure and temperature gradients tend to

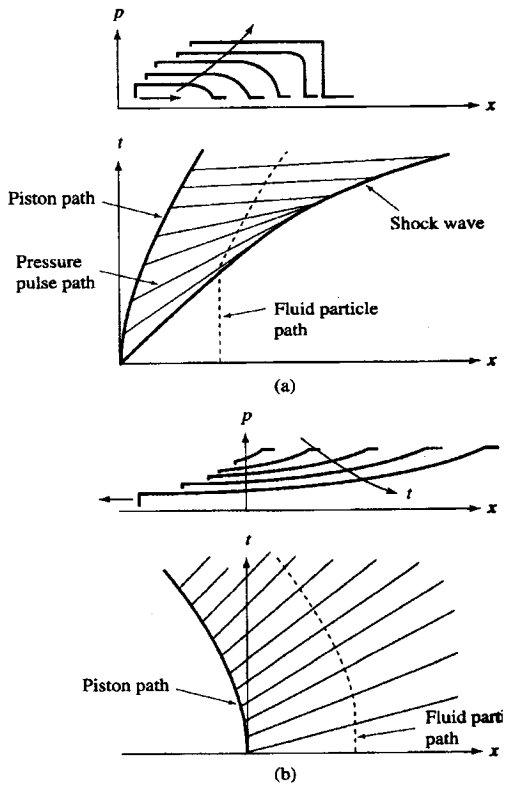

Figure A.2: Time-Distance Plot
a. Development of a shock wave by a piston accelerating into a gas-filled tube;
b. Development of a rarefaction wave by a piston accelerating out of a gas-filled tube.

become very large, but internal viscous stresses and heat transfer rates limit this effect resulting in a compression front termed as a *normal shock wave* that remains as a thin (finite thickness) moving region.

A.3. Expansion Waves

By way of comparison, the formation of expansion waves can be explained in a similar way. If the piston is drawn away from rather than into the fluid, a reverse process to that just illustrated occurs. When the piston moves to the left at some velocity, a weak expansion wave travels through the gas moving to the **right** at sonic speed. The gas behind the wave is set in motion to the left at the speed of the piston. Due to the expansion, the gas behind the wave is at a temperature and pressure slightly lower than the gas upstream of the wave. A second increment in velocity of the piston generates a second weak expansion wave, which travels to the right at a slower speed than the first wave. The reduction is speed is because of the expansion and cooling experienced by the gas as a result of the passage of the first wave. Note that the gas and the waves move in the opposite directions. The second wave travels slower than the first wave and lags behind the first wave. Each expansion wave is less steep than its predecessor and unlike compression waves; successive expansion waves do not form a finite expansion wave. The resulting pressure profile, termed a *rarefaction wave*, continuous to broaden along the tube, see Figure A.2b.

A.4. Shock Tube

A shock tube is a device suitable for producing high velocities and temperatures. It is used extensively in the study of unsteady short duration phenomena in varied fields ranging from aerodynamics, physics etc. Wave structures and wave interactions can be studied when the shock wave propagates at a high speed yet these high speeds necessitate that experimental measurements be accomplished in a very short time, usually in the range of milliseconds or less. The shock tube consists of a long tube divided into two sections by a diaphragm (membrane) as shown in Figure A.3a.

Chamber 4, called the driver section, contains gas ("driver" gas) at a high pressure whereas chamber 1, called expansion section, contains gas ("test" gas) at a low pressure. At time t = 0, the diaphragm (membrane) is ruptured, the driver gas compresses a slug of the test gas, much as the moving piston described earlier, and generates a series of compression waves that rapidly coalesce into a normal shock wave which propagates at supersonic speed in the expansion section and sets up the gas behind it in motion in the direction of the shock at velocity V_2. The laws of normal shock dictate that $p_2 > p_1$, $T_2 > T_1$ and $\rho_2 > \rho_1$. At the same time a rarefaction wave emanates at the diaphragm section and propagates in the opposite direction into the driver section 4. The leading rarefaction wave (head wave) propagates into the gas of the driver section at a local speed of sound c_4. In a similar manner the tail wave propagates at a local speed of sound of c_3. The gas in the driver section is at rest until affected by the rarefaction waves and the gas behind the tail wave is set in motion to the right at a velocity V_3 equal to V_2. The interaction of the shock wave and the rarefaction waves establishes a common pressure $p_2(= p_3)$ and a common velocity $V_2(= V_3)$ for the gas downstream of these waves. The gases in region 2

and 3 though differ in temperature and entropy, thus a surface of discontinuity is created which moves to the right at the same velocity of the gases and these two regions. This is called contact surface. Figures A.4a, A.4b A.4c show the distributions of different properties at some later time t_1 based on the shock tube configuration described in Figures A.3a, A.3b.

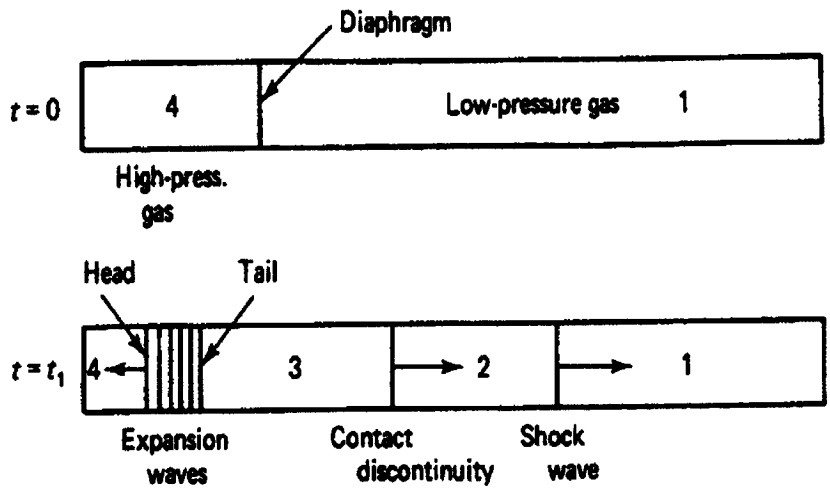

Figures A.3a, A.3b: Shock tube

In addition the Figure A.5 indicates the location at which the test object must be placed in order to subject it to a maximum testing time. This time depends on the length of tube and the velocities of the shock and expansion waves.

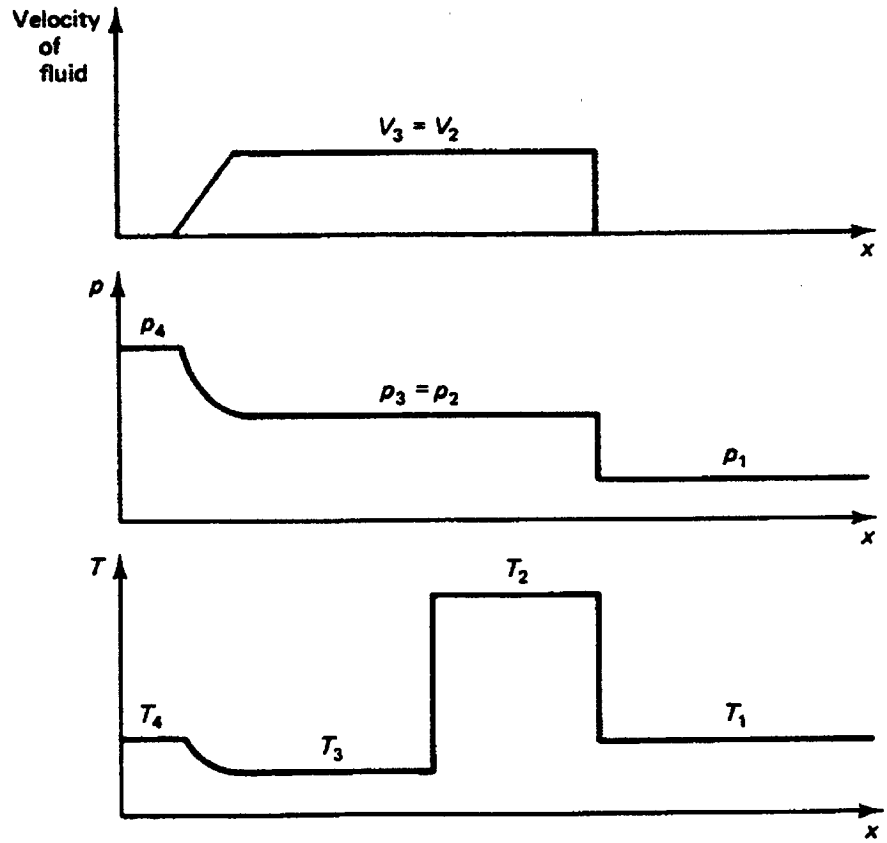

Figures A.4a, A.4b, A.4c: Property Distributions at time = t_1

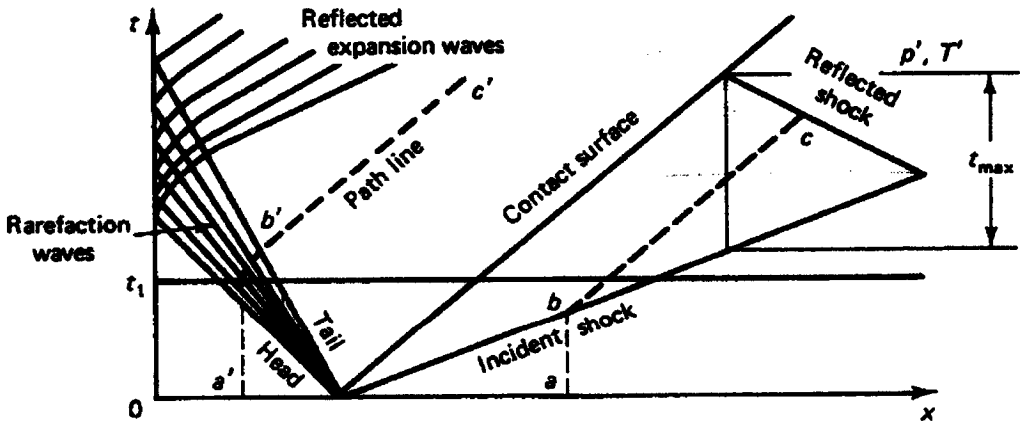

Figure A.5: Time-Position diagram

A.5 Moving Shock and Expansion Waves

When a normal shock or expansion wave propagates at a constant speed in a gas, its apparent motion depends on the coordinate system that is selected. If coordinate system is fixed, the motion is viewed as unsteady, yet if the coordinate system itself is moving with the wave, the flow across the shock or expansion appears steady. With this transformation in mind consider a normal shock wave propagating at an absolute velocity V'_s into a gas that it is itself, moving at a velocity V'_x as shown in Figure A.6a and A.6b. The shock propagation sets the gas behind it in motion at velocity V'_y. Figure A.6a indicates the properties of the gas across the shock wave relative to a fixed coordinate system and are identified by primes. In Figure A.6b the coordinate system is moving with the wave. The velocities of the gas on both sides of the shock are therefore related as follows:

$$\left.\begin{aligned} V_y &= V'_s - V'_y \\ \text{and} \quad V_x &= V'_s - V'_x \end{aligned}\right\} \qquad \text{(A.5.1)}$$

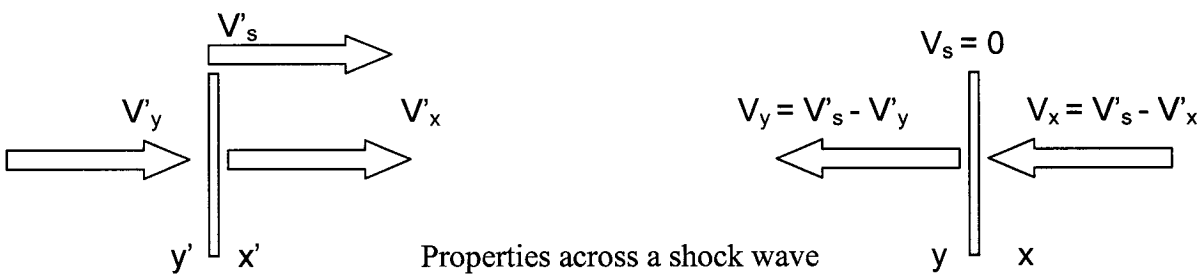

Figure A.6a. Moving Wave

Figure A.6b. Stationary Wave

When a normal shock wave travels in a closed-end tube, the gas between the shock wave and the closed end remains at rest. The gas behind the shock wave however moves at a velocity V'_y. Figure A.7a shows the incident shock reflected at the closed end of a shock

tube and how it propagates back through the incoming gas. Again based on the coordinate system two configurations of motion are observed, as it can be seen in Figure A.7b.

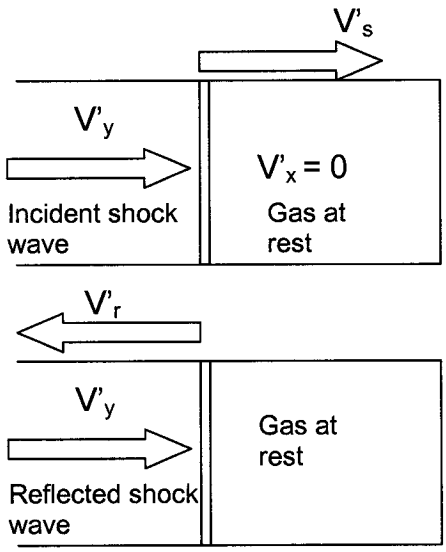

Figure A.7a. Velocities relative to a fixed coordinate system

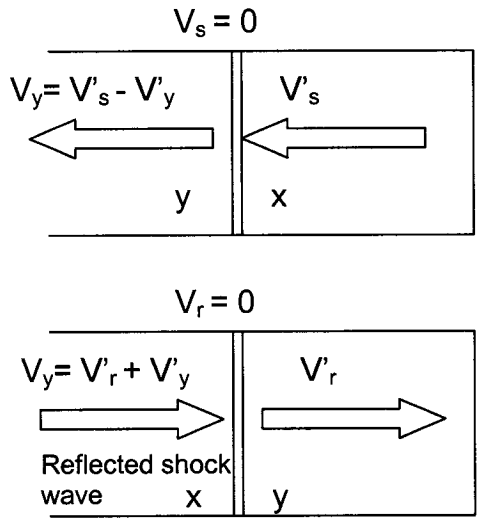

Figure A.7b. Velocities relative to a System moving with the wave.

In the event that an incident shock wave is propagating into an open-ended tube as shown in Figure A.8a and A.8b, due to the decrease in pressure that will take place across the reflected wave and the incident shock wave at the open ended side of the tube, the incident shock wave is reflected at the open end as an expansion wave. This is how expansion waves are created in the working section of the shock tube in the Aerodynamics laboratory of CCNY. The aforementioned waves then interact with the grid generated isotropic and homogeneous turbulent field as described in Chapters 1 and 2 previously.

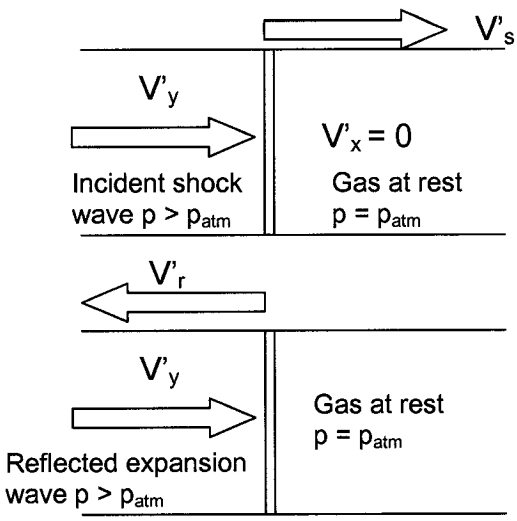

Figure A.8a. Velocities relative to a fixed coordinate system

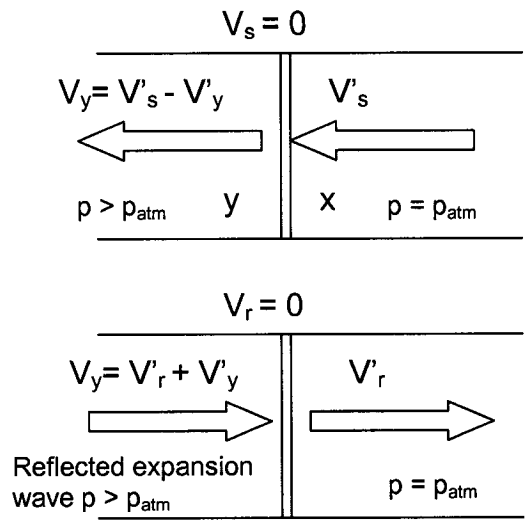

Figure A.8b. Velocities relative to a system moving with the wave.

A.6 Governing Equations

Some of the governing equation will be presented here considering normal shock waves propagating adiabatically through a gas in a shock tube of constant cross sectional area A as shown in Figure A.9. The properties of the gas downstream of the shock will be expressed here rather than derived. The derivations along with all the assumptions involved can be found in many compressible Fluid Flow books.

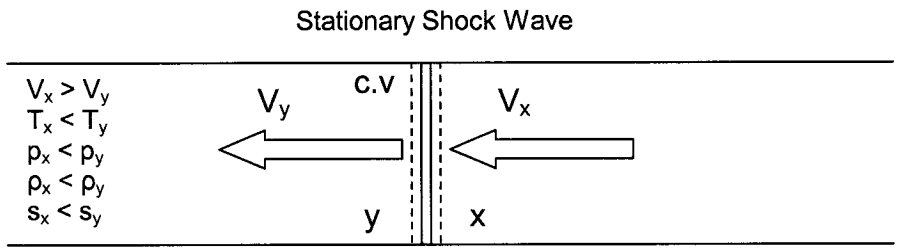

Figure A.9b. Changes of properties across a normal shock, stationary wave

First properties will be expressed in terms of both the Mach numbers and ratio of specific heats γ ($= \frac{C_p}{C_v}$), and then they will be presented as functions of only the upstream Mach number and γ.

Ratio of static temperature:
$$\frac{T_y}{T_x} = \frac{1+\frac{\gamma-1}{2}M_x^2}{1+\frac{\gamma-1}{2}M_y^2} \quad \text{.....(A.6.1)}$$

Using continuity and perfect gas law:
$$\frac{T_y}{T_x} = \frac{\rho_x p_y}{\rho_y p_x} = \frac{V_y}{V_x}\frac{p_y}{p_x} \quad \text{.....(A.6.2)}$$

since
$$\frac{V_y}{V_x} = \frac{M_y}{M_x}\sqrt{\frac{T_y}{T_x}} \quad \text{.....(A.6.3)}$$

and by using the above equations the temperature ratio can be eliminated and the pressure ratio across the shock is given by:

$$\frac{p_y}{p_x} = \frac{M_x}{M_y}\sqrt{\frac{1+\frac{\gamma-1}{2}M_x^2}{1+\frac{\gamma-1}{2}M_y^2}} \quad \text{.....(A.6.4)}$$

the density ratio across the shock is:
$$\frac{\rho_y}{\rho_x} = \frac{T_x}{T_y}\frac{p_y}{p_x} \quad \text{.....(A.6.5)}$$

combining Eq. (A.6.1) and Eq. (A.6.4) the density ratio becomes:

$$\frac{\rho_y}{\rho_x} = \frac{M_x}{M_y}\sqrt{\frac{1+\frac{\gamma-1}{2}M_y^2}{1+\frac{\gamma-1}{2}M_x^2}} \quad \text{.....(A.6.6)}$$

the ratio of stagnation pressures is given by:

$$\frac{p_{0y}}{p_{0x}} = \frac{\left(\frac{p_{0y}}{p_y}\right)}{\left(\frac{p_{0x}}{p_x}\right)}\left(\frac{p_y}{p_x}\right) \quad \text{.....(A.6.7)}$$

which can be expressed in terms of M_x and M_y as:

$$\frac{p_{0y}}{p_{0x}} = \frac{M_x}{M_y}\frac{(1+\frac{\gamma-1}{2}M_y^2)^{\frac{(\gamma+1)}{[2(\gamma-1)]}}}{(1+\frac{\gamma-1}{2}M_x^2)^{\frac{(\gamma+1)}{[2(\gamma-1)]}}} \quad \text{.....(A.6.8)}$$

The entropy change across the shock is:

$$s_y - s_x = C_p \ln\frac{T_y}{T_x} - R\ln\frac{p_y}{p_x} = C_p \ln\frac{\frac{T_y}{T_x}}{\left(\frac{p_y}{p_x}\right)^{\frac{\gamma-1}{\gamma}}} \quad \text{.....(A.6.9)}$$

where temperature ratio is given by Eq. (A.6.1) and the pressure ratio by Eq. (A.6.4).

The temperature, pressure and density ratios can be expressed as functions of only a single Mach number as follows:

$$\frac{T_y}{T_x} = \frac{[2\gamma M_x^2 - (\gamma-1)][2+(\gamma-1)M_x^2]}{(\gamma+1)^2 M_x^2} \quad \text{.....(A.6.10)}$$

$$\frac{p_y}{p_x} = \frac{2\gamma M_x^2 - (\gamma-1)}{\gamma+1} \quad \text{.....(A.6.11)}$$

$$\frac{\rho_y}{\rho_x} = \frac{V_x}{V_y} = \frac{(\gamma+1)M_x^2}{2+(\gamma-1)M_x^2} \quad \text{.....(A.6.12)}$$

$$\frac{p_{0y}}{p_{0x}} = [\frac{2\gamma M_x^2 - (\gamma-1)}{\gamma+1}]^{\frac{-1}{(\gamma-1)}}[\frac{(\gamma+1)M_x^2}{2+(\gamma-1)M_x^2}]^{\frac{\gamma}{\gamma-1}} \quad \text{.....(A.6.13)}$$

The pressure rise across the shock, $\frac{p_y}{p_x} = \frac{p_2}{p_1}$, is called the ***strength of the shock***.

A.6.1. Rankine-Hugoniot Relations

The Rankine-Hugoniot relations relate the densities and the static pressures across a normal shock. The derivation again is not in the scope of this appendix thus the expressions will be expressed for reference.

The pressure ratio across the shock can be expressed in terms of the density ratio as follows:

$$\frac{p_y}{p_x} = \frac{\frac{\gamma+1}{\gamma-1}\frac{\rho_y}{\rho_x} - 1}{\frac{\gamma+1}{\gamma-1} - \frac{\rho_y}{\rho_x}} \quad \text{.....(A.6.1.1)}$$

or conversely the density ratio can be expressed in terms of the pressure ratio:

$$\frac{\rho_y}{\rho_x} = \frac{\frac{\gamma+1}{\gamma-1}\frac{p_y}{p_x} + 1}{\frac{\gamma+1}{\gamma-1} + \frac{p_y}{p_x}} \quad \text{.....(A.6.1.2)}$$

Equations (A.6.1.1) and (A.6.1.2) relate the static pressure ratio and the density ratio across an irreversible adiabatic compression shock wave. For an isentropic process the relationship of pressure and density is: $\frac{\rho_2}{\rho_1} = \left(\frac{p_2}{p_1}\right)^{\frac{1}{\gamma}}$ .....(A.6.1.3)

If values of pressure ratio are calculated for various density ratios and compared with Eq. (A.6.1.3), some interesting observations can be made. At low-pressure ratios (~ 4.0), the Hugoniot curve and the isentropic curve differ only slightly from each other, so that a weak shock appears like an isentropic process. To achieve such a pressure ratio across the

shock the driver section of a shock tube needs to be pressurized to approximately 25 times that of the ambient (~ 375psig) which is much more than what this set of experiments will deal with. At the large pressure ratios, which characterize strong shocks, the density ratio reaches some limiting value (~ 6.0 for $\gamma = 1.4$) whereas in the isentropic process the density ratio increases constantly.

Appendix B: Vorticity Calibration and Decomposition

B.1. Vorticity Probe Calibration For Velocity/Mass Flux Measurements

The vorticity probe consisted of three triple wire modules each coupled with an independent temperature wire sensor. The hot-wires for velocity/mass flux measurement were driven under a constant temperature mode using Dantec 56C01CTA/56C17 Bridge modules, while temperature wires were driven under a constant current mode using a simple electronic circuit shown in Figure B.2. The triple hot-wire module required a very elaborate calibration procedure including velocity and yaw and pitch response tests. On the other hand, the temperature wire calibration was simple due to the nature of the temperature sensitivity of the wire, which yields a linear response to a sensed total temperature.

B.1. Temperature (Cold Wire Calibration)

The cold wire, when placed in a flow, it measures both velocity and temperature fluctuations. In order to use the cold wire as a temperature measurement device, the sensitivity of the wire to velocity fluctuations must therefore be minimal, i.e. $\frac{\partial E}{\partial U} = 0$.

A length to diameter ratio of ≈700 [length of ≈1.5mm, diameter of 2.5 μm] was used for these wires to minimize the end conduction effects as proposed by (Bradshaw[36]). To calculate the corresponding sensitivities due to temperature and velocity fluctuations the following expressions are used. The temperature sensitivity on the flow velocity of the 2μm platinum/Tungsten temperature wire can be found by using the suggestion of Wyngaard[37] as:

$$\frac{\partial T}{\partial U} = \frac{I^2 R_w (\frac{1}{4} \mathrm{Re}_d^n)}{\pi k_f l U_i (0.24 + 0.56 \mathrm{Re}_d^n)^2} \qquad \text{(B.1.1)}$$

where $n = 0.45$ and

I = supplied current [0.5mA]

R_w = the resistance of the wire [10 Ω]

Re_d = the Reynolds number based on the diameter of the wire

k_f = the thermal conductivity of air [0.025 (A^2 Ω)/(m °C)]

l = the length of the wire [1.5mm]

U_i = the mean flow velocity [200 $\frac{m}{\text{sec}}$]

The range of the temperature wire sensitivity to velocity fluctuation will now be calculated in order to show its minimal value and thus minimal effect to the temperature measurements. From Equation B.1.1 and assuming that a 2.5 μm Platinum/Tungsten wire is used in a 200 $\frac{m}{\text{sec}}$ flow to measure temperature, then $\frac{\partial T}{\partial U} = 1.574 \times 10^{-5} \frac{^oC}{m/\text{sec}}$.

Typical values that were used in the previous calculation are given in the brackets above where the properties of air were evaluated at 50 °C. The temperature sensitivity $\frac{\partial E}{\partial T}$ is now required in order to calculate the fluctuation due to the velocity $\frac{\partial E}{\partial U}$ since the later is given by $\frac{\partial E}{\partial U} = \frac{\partial E}{\partial T}\frac{\partial T}{\partial U}$. (B.1.2)

Using $\frac{\partial E}{\partial T} = \alpha I R_w$ where $\alpha = 0.004 \frac{1}{^oC}$ is the temperature resistivity of the Platinum/Tungsten wire, having a typical value of $\frac{\partial E}{\partial T} = 0.024 \frac{mV}{^oC}$ the velocity sensitivity from Equation B.1.2 becomes $\frac{\partial E}{\partial U} = \frac{\partial E}{\partial T}\frac{\partial T}{\partial U} = 3.778 \times 10^{-7} \frac{mV}{m/\sec}$.

Taking now into account the case of a very low speed [$20 \frac{m}{\sec}$], temperature sensitivity of the wire to mean velocity is: $\frac{\partial T}{\partial U} = 3.303 \times 10^{-4} \frac{^oC}{m/\sec}$, resulting in a maximum velocity sensitivity of the wire of $\frac{\partial E}{\partial U} = 7.928 \times 10^{-6} \frac{mV}{m/\sec}$.

In view of the above calculations, $3.778 \times 10^{-7} < \frac{\partial E}{\partial U} < 7.928 \times 10^{-6} \frac{mV}{m/\sec}$, it can be accurately assumed that the 2.5 μm temperature wire is insensitive to velocity fluctuations in the above range of flow conditions.

The output voltage can be converted easily using a conversion factor similar to the above $\frac{\partial E}{\partial T}$ with the corresponding operating conditions of each cold wire (i.e. constant current, R_w, I_w). The above value for the temperature sensitivity can be used without the introduction of a significant error. A typical temperature calibration can be seen in Figure B1. The 1-D inviscid total temperature of the flow is plotted against the calculated mean total temperature using the above calibration value. The recorded shock strength of each experiment was used to identify the 1-D total temperature. The data collapsing on a straight line supports the insensitivity claim of the temperature wire to velocity as well as the validity of the calculations.

The calibration of the cold wires for the X wire probes, and the vorticity probe were performed using the above procedure. Figure B.2 shows the circuit used for the temperature wires.

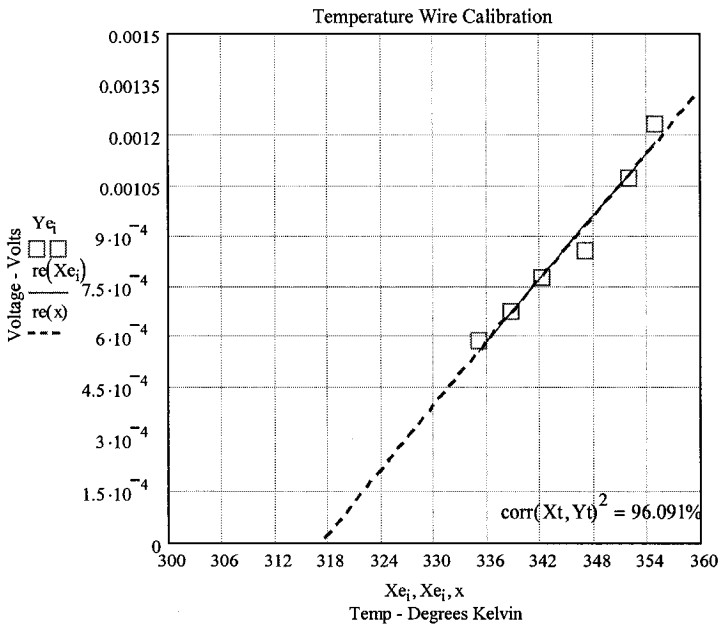

Figure B.1: Calibration Curve for a Typical Temperature Wire.

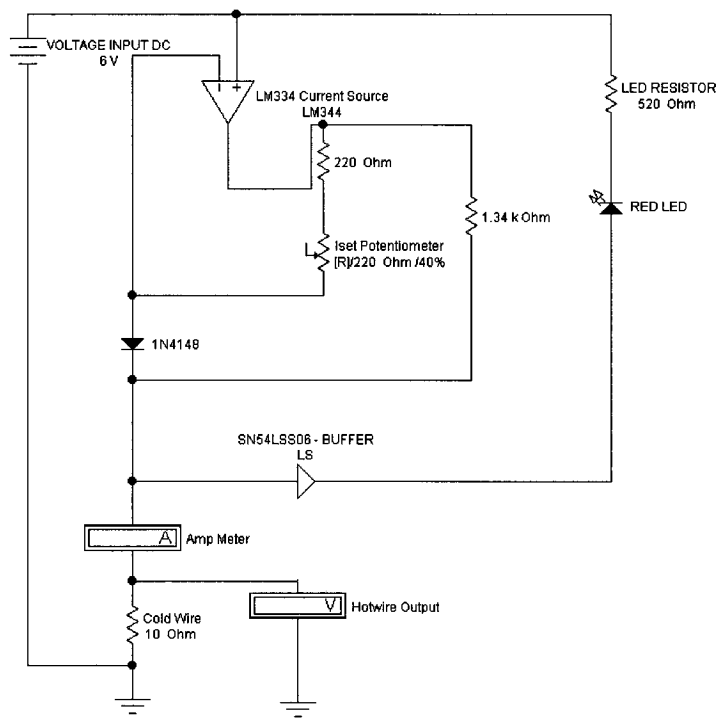

Figure B.2: Electronic Circuit for Wires operated under CCA Mode.

B.2. Triple wire calibration:

The triple wire required an extensive analysis owing to the governing King's law relation. King's Law applied to non-isothermal flows is given by:

$$\frac{E^2}{T_w - T_0} = A\left[\frac{T_0}{T_r}\right]^a + B\left[\frac{T_0}{T_r}\right]^b (\rho U_{eff})^n \qquad \text{(B.2.1)}$$

where T_w is the wire temperature and T_r is a reference temperature usually taken to be the ambient temperature. The wire temperature is set by setting the overheat ratio on the Wheatstone bridge; in all the experiments here the overheat ratio was 100% which rendered a hotwire temperature T_w = *550K*. Physically, this is done by adjusting the decade resistance in the bridge, which causes an increase in current to the hot-wire, which is on one branch of the bridge, thereby increasing the wire temperature due to increased heat transfer at the wire surface. The values suggested by Kovasznay[38] for a and b are 0.768, and the exponent n may range from 0.42 to 0.45.

If 3-D response of the wire is considered, the relation for U_{eff} given by Jorgenson[39] applies

$$U_{eff}^2 = U_N^2 + k^2 U_T^2 + h^2 U_B^2 \qquad \text{(B.2.2)}$$

The subscripts refer to the normal, tangential and bi-normal components respectively. The coefficients k and h are the pitch and yaw coefficients, respectively. They are generally a function of the inclination of the impinging velocity vector, and normally described in terms of the yaw and pitch angles of the vector. Combining Equation B.2.1 and Equation B.2.2 for three individual wires with some manipulation gives, (B.2.3

$$(\rho U_{eff_1})^2 = \left[\frac{\rho E_1^2[\frac{T_r}{T_0}]}{T_w - T_0}\right]^{\frac{1}{n}}, (\rho U_{eff_2})^2 = \left[\frac{\rho E_2^2[\frac{T_r}{T_0}]}{T_w - T_0}\right]^{\frac{1}{n}}, (\rho U_{eff_3})^2 = \left[\frac{\rho E_3^2[\frac{T_r}{T_0}]}{T_w - T_0}\right]^{\frac{1}{n}}$$

Due to the orthogonality of the triple wire set, Equation B.2.2 is conveniently employed by noting that the tangential velocity components of one wire lies normal to one of the other two and in the binormal direction of the third. This can be used derive the component relations for each wire.

$$U_{eff_1}^2 = Y^2 + k_1^2 X^2 + h_1^2 Z^2 \tag{B.2.4}$$

$$U_{eff_2}^2 = Z^2 + k_2^2 Y^2 + h_2^2 X^2 \tag{B.2.5}$$

$$U_{eff_3}^2 = X^2 + k_3^2 Z^2 + h_3^2 Y^2 \tag{B.2.6}$$

Where X, Y and Z have arbitrarily been chosen to be the normal, bi-normal and tangential velocity components of each wire, respectively. For a calibration test, the velocity vector is known in terms of the laboratory coordinate system. The velocity components in lab coordinates are related to the wire coordinate velocity components through the use of the respective direction cosines (the cosine of the angle between the primed and unprimed coordinate axii), i.e.

$$\begin{bmatrix} u \\ v \\ w \end{bmatrix} = \begin{bmatrix} X' \\ Y' \\ Z' \end{bmatrix} = \begin{bmatrix} \cos(X',X) & \cos(X',Y) & \cos(X',Z) \\ \cos(Y',X) & \cos(Y',Y) & \cos(Y',Z) \\ \cos(Z',X) & \cos(Z',Y) & \cos(Z',Z) \end{bmatrix} \begin{bmatrix} X \\ Y \\ Z \end{bmatrix} \tag{B.2.7}$$

Therefore, the normal, bi-normal, and tangential velocity components for each wire are found from values of X, Y, and Z as derived above.

Or,

$$\begin{bmatrix} X \\ Y \\ Z \end{bmatrix} = N^{-1} \begin{bmatrix} u \\ v \\ w \end{bmatrix} \tag{B.2.8}$$

The velocity magnitude, which is the same in both coordinate systems, can be used with to reformulate the B coefficient of Equation B.2.1 with the help of Equation B.2.2. This is seen in the following equation,

$$\frac{E^2\left[\frac{T_r}{T_0}\right]}{T_w - T_0} = A + \left[B\left(\frac{U_N^2}{Q^2} + k^2\frac{U_T^2}{Q^2} + h^2\frac{U_B^2}{Q^2}\right)\right](\rho Q)^n \tag{B.2.9}$$

The complex term in front of $(\rho Q)^n$ can be represented by a another coefficient B', then

$$\frac{E^2\left[\frac{T_r}{T_0}\right]}{T_w - T_0} = A + B'(\rho Q)^n \tag{B.2.10}$$

This is a valid alternate form of King's law since the coefficient B' has absorbed the dependence of the three wire components and the yaw and pitch coefficients. Notice this expression implies that mass flux calibration can be performed independent of probe orientation. The calibration procedure begins with this last expression. During a calibration either in the wind tunnel or the shock tube, the probe is subjected to different, but known or controlled, incoming flow conditions, i.e. increasing normal mean velocity or mass flux respectively. The measured raw voltages and known flow conditions are plotted to obtain a calibration curve. Therefore, the constants A and B' are obtained from this calibration.

From,

$$B' = B\left(\frac{U_N^2}{Q^2} + k^2\frac{U_T^2}{Q^2} + h^2\frac{U_B^2}{Q^2}\right) \qquad \text{(B.2.11)}$$

the coefficient B' is shown to be a function of B, k, and h. A simple method to obtain the unknown coefficients above (recall B' is found from the mass flux calibration) was developed. This method starts with an assumed value of k and arbitrarily chosen value of h with some justification. In the present case a value of $k^2 = 0.02$ has been chosen and was kept constant. The value of h, on the other hand, is significantly larger with average values being reported as 1.2 for h^2, with moderate variation. Once these two values are chosen the coefficient B is determined, and its value, as that of the k coefficient, is kept fixed. This leaves h to account for the variation in yaw and pitch of the sensed velocity vector.

Yaw and pitch response experiments were previously performed on the probe to determine the value of h as a function of these two angles. Each wire gives h as a smooth function of yaw and pitch. These surface maps were used to obtain discrete interpolated values of h, which were then applied to the processing of the mass flux data. A two-dimensional array was created from yaw coefficient values obtained from experiment, whose function was to find an interpolated value of the yaw coefficient based on input values of yaw angle and pitch angle. Figures B.3 – B.5 provide the calibration lines for each of the wires for each of the individual array. The X – axis denotes the $(\rho U_i)^n$ where $n = 0.45$ for the case of the hotwires in the vorticity probe. For the X wire probes the power value of n was not assumed as the typical value of 0.45 but rather fitted the calibration data that gave the minimum value of the error. The Y – axis denotes the

voltage output of the Constant Temperature Anemometer normalized with respect to the local flow temperature during calibration i.e.

$$Y_i = \frac{(E_i)^2}{T_w - T_{0_i}} \left(\frac{T_r}{T_{0_i}}\right)^a$$

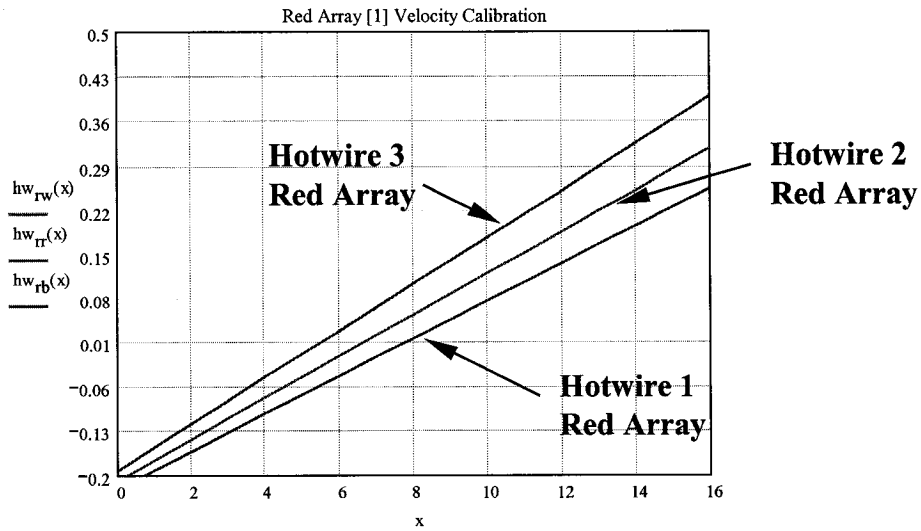

Figure B.3: Calibration Curve for Array # 1 [Red].

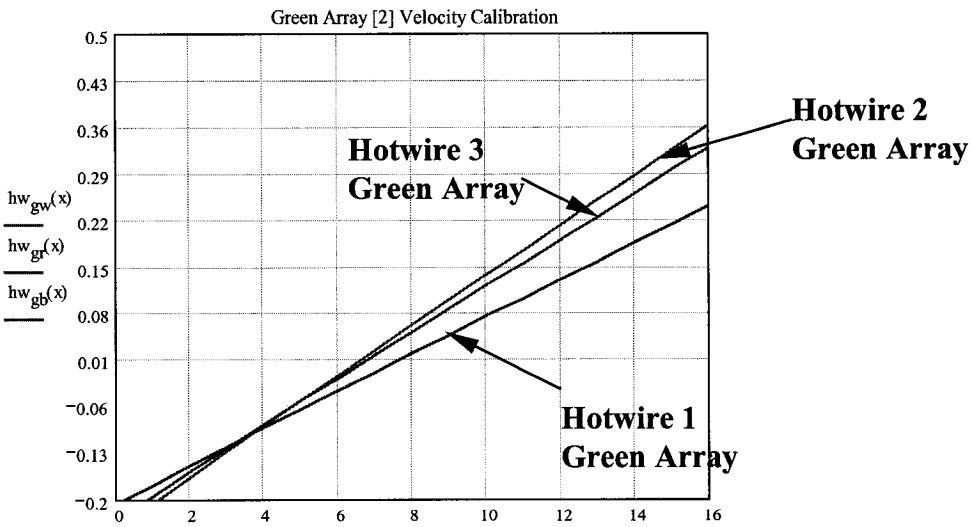

Figure B.4: Calibration Curve for Array # 2 [Green].

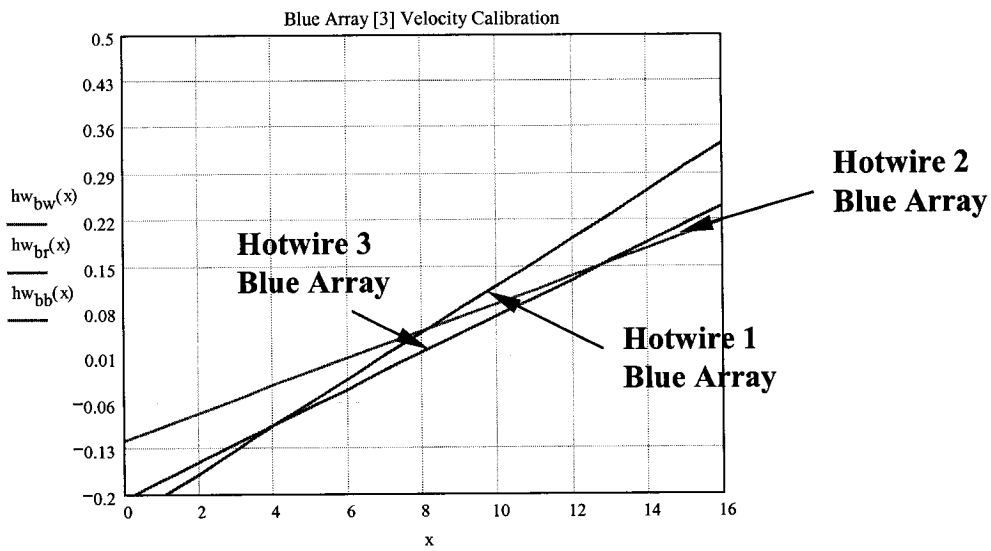

Figure B.5: Calibration Curve for Array # 3 [Blue].

B.3. Transformation into Laboratory Coordinate System for a single array.

Each individual array for the vorticity probe has to have its individual velocity components transformed into the probe and consequently into the laboratory coordinate system. The transformation presents an inclination of the XY plane (rotated around the Y-axis as shown in Figure B.6) by a pitch angle β, followed by a rotation around the X – axis, roll angle ω.

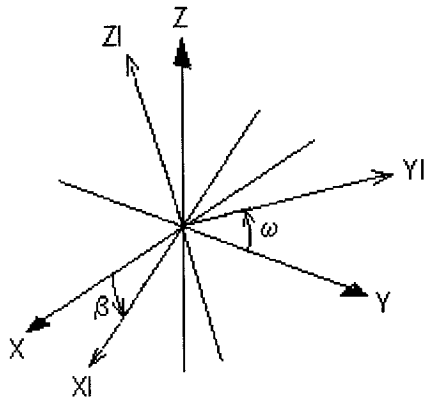

Figure B.6: Transformation of Coordinates.

The transformation matrix for pitch is given by **P**:

$$\mathbf{P} = \begin{bmatrix} \cos\beta & 0 & -\sin\beta \\ 0 & 1 & 0 \\ \sin\beta & 0 & \cos\beta \end{bmatrix} \tag{B.3.1}$$

where the roll matrix is given by **R**:

$$\mathbf{R} = \begin{bmatrix} 1 & 0 & 0 \\ 0 & \cos\omega & \sin\omega \\ 0 & -\sin\omega & \cos\omega \end{bmatrix} \tag{B.3.2}$$

BIBLIOGRAPHY

[1] Andreopoulos, Y., Agui, J. H. and Briassulis, G., "Shock Wave-Turbulence Interactions," *Annual Review of Fluid Mechanics*, Vol. 32, 2000, pp. 309-345.

[2] Briassulis, G. K., and Andreopoulos, J., "High Resolution Measurements of Isotropic Turbulence Interacting with Shock Waves," AIAA Paper 96-0042, Jan. 1996.

[3] Briassulis, G. K., Agui, J., and Andreopoulos, Y., "The structure of weakly compressible grid turbulence," *Journal of Fluid Mechanics*, Vol. 432, 2001, pp. 219-283.

[4] Agui J., "Shock Wave Interactions with Turbulence and Vortices," Ph.D. Thesis. The City University of New York, 1998.

[5] Sternberg, J., "The Transition from a Turbulent to a Laminar Boundary Layer," Rept. 906, May 1954, Ballistic Research Labs., Aberdeen, Md.

[6] Vivekanandan, R., " A Study of Boundary Layer Expansion Fan Interactions near a Sharp Corner in Supersonic Flow," 1963, M.Sc. thesis, Dept. of Aeronautical Engineering, Indian Institute of Science, Bangalore, India.

[7] Viswanath, P.R. and Narashima, R., " Base Pressure on Sharply Boat-Tailed Aft Bodies," Rept. 72 FMI, July, Dept. of Aeronautical Engineering, Indian Institute of Science, Bangalore, India.

[8] Ananda Murthy, K.R. and Hammitt, A. G., "Investigation of the Interaction of a Turbulent Boundary Layer with Prandtl-Meyer Expansion Fan at M=1.88," Report 434, 1958, Dept. of Aeronautical Engineering, Princeton University, Princeton, NJ.

[9] Morkovin, M. V., "Effects of High Acceleration on a turbulent Supersonic Shear Layer," Proceedings, Heat Transfer and Fluid Mechanics Institute, Los Angeles, California, June 1955.

[10] Narashima, R. and Viswanath, P.R., "Reverse Transition at an Expansion Corner in Supersonic Flow," AIAA Journal, Technical Notes, May. 1975, pp.693-695.

[11] Narashima, R. and Sreenivasan, K.R., "Relaminarization in Highly Accelerated

Turbulent Boundary Layers." Journal of Fluid Mechanics, Vol. 61, Nov. 1973, pp. 417-447.

[12] Dussauge, J.P. and Gaviglio, J. "The rapid expansion of a supersonic turbulent flow: role of bulk dilatation," Journal of Fluid Mechanics, Vol. 174, 1987, pp. 81-112.

[13] Smith, D.R. and Smits, A. J., " The Rapid Expansion of a Turbulent Boundary Layer in a Supersonic Flow," Theoretical and Computational Fluid Dynamics, 1991 2: 319-328.

[14] Dawson, J.D., Samimy, M., & Amette, S.A., 1994, "The Effects of Expansion on a Supersonic Boundary Layer: Surface Pressure Measurements," AIAA J., 32, No.11, pp. 2169-2177.

[15] Johnson, A. W., 1993, "Laminarization and Retransition of Turbulent Boundary Layers in Supersonic Flow," Ph.D. Dissertation, Yale University, New Haven, CT.

[16] Bloy, A.W., Georgeer, M.P., 1974, "The hypersonic Laminar Boundary Layer near Sharp Compression and Expansion Corners," J. Fluid Mech., 63(3), 431-447.

[17] Hill, F.K, "Turbulent Boundary Layer measurements at Mach number s from 8 to10, Physics of Fluids, 1959, 2:668-680.

[18] Lewis, J.E., Gran, R.L., and Kubota, T., 1972, "An Experiment on the Adiabatic Compressible Turbulent Boundary in Adverse and Favorable Pressure Gradients," J. Fluid Mech., 41(4), 657-672.

[19] Arnette, S.A., Samimy, M., & Elliott, G.S., 1995, "Structure of Supersonic Turbulent Boundary Layer After Expansion Regions," AIAA Journal, 33, 430-438.

[20] Dawson, J.D., Samimy, M., & Amette, S.A., 1994, "The Effects of Expansion on a Supersonic Boundary Layer: Surface Pressure Measurements," AIAA J., 32, No.11, pp. 2169-2177.

[21] Xanthos, S. and Andreopoulos, Y., 2003, "Experiments of Compressible and Homogeneous and Isotropic Turbulence interacting with Expansion Waves", ASME Paper FEDSM2003-45075.

[22] Briassulis, G., Honkan, A., Andreopoulos, J., and Watkins, B. C. "Applications of Hot-Wire Anemometry in Shock Tube Flows," *Exp. in Fluids,* Vol. 19, 1995, pp. 29-37.

[23] Briassulis, G. K., "Unsteady Nonlinear Interactions of Turbulence with Shock Waves," Ph.D. Thesis. City College of CUNY, 1996.

[24] Briassulis, G., Agui, J., Andreopoulos, J., and Watkins, B. C., "A Shock Tube Research Facility for High-Resolution Measurements of Compressible Turbulence," *Experimental Thermal and Fluid Science*, 1996, pp. 430-446.

[25] Xanthos, S.S, Briassulis, and Andreopoulos, Y., "Interaction of Decaying Freestream Turbulence with a Moving Shock Wave: Pressure Field", *Journal of Propulsion and Power*, Volume 18, Number 6, 2002, pp. 1289-1297.

[26]Laws, E. M., and Livesey, J. L., "A Flow through screens," *Annual Review of Fluid Mechanics*, Vol. 10, 1978, pp 247-266.

[27] Groth, J., and Johansson, A. V., "A Turbulence reduction in screen," *Journal of Fluid Mechanics*, Vol. 197, 1988, pp 139-155.

[28] Taylor, G. I, and Davies, R. M., "The aerodynamics of porous sheets," A.R.C. R&M 2237, 1944.

[29] Pinker, R. A., and Herbert, M. V., "Pressure loss associated with compressible flow thorough square-mesh wire gauzes," *J. Mech. Eng. Science*, Vol. 9 (1), 1967, p11-23.

[30] Tsinober, A., Kit, E., and Dracos, T. 1992 Experimental Investigation of the Field of Velocity Gradients in Turbulent Flows. J. Fluid Mech., vol. 242, 169.

[31] Honkan A, Andreopoulos J. 1997 Vorticity strain-rate and dissipation characteristics in the near wall region of turbulent boundary layers. *J. Fluid Mech.* 350:29-96.

[32] Briassulis G., Honkan A., Andreopoulos J., Watkins, B. C. 1995 *Applications of Hot-Wire Anemometry in Shock Tube Flows.* Exp. in Fluids. 19: 29-37.

[33] Andreopoulos, J. 1983a Improvements of the Performance of Triple Hot Wire Probes. Rev. Sc. Instrum., vol. 54, 733-740.

[34] Andreopoulos, J. 1983b Statistical Errors Associated with Turbulence Intensity and Probe Geometry in Hot-Wire Anemometry. Physics E. Sci. Instr., Vol. 16, 1264-1271.

[35] Morkovin M.V. 1960 Note on Assessment of Flow Disturbances at a Blunt Body Traveling at Supersonic Speeds Owing to Flow Disturbances in Free Stream. *J. Applied Mechanics* 27: 223-229.